LA--13315-T

LA-13315-T
Thesis

Neutron Detection and Multiplicity Counting Using a Boron-Loaded Plastic Scintillator/Bismuth Germanate Phoswich Detector Array

Los Alamos
NATIONAL LABORATORY

Los Alamos National Laboratory is operated by the University of California for the United States Department of Energy under contract W-7405-ENG-36.

This thesis was accepted by the Nuclear Engineering Department, University of New Mexico, Albuquerque, New Mexico, in partial fulfillment of the requirements for the degree of Doctor of Philosophy. The text and illustrations are the independent work of the author and only the front matter has been edited by the CIC-1 Writing and Editing Staff to conform with Department of Energy and Los Alamos National Laboratory publication policies.

This work was supported by the US Department of Energy, Office of Nonproliferation and National Security, Office of Research and Development.

An Affirmative Action/Equal Opportunity Employer

DISCLAIMER

Portions of this document may be illegible electronic image products. Images are produced from the best available original document.

LA-13315-T
Thesis

UC-700
Issued: March 1998

Neutron Detection and Multiplicity Counting Using a Boron-Loaded Plastic Scintillator/Bismuth Germanate Phoswich Detector Array

Michael Conrad Miller

Los Alamos
NATIONAL LABORATORY
Los Alamos, New Mexico 87545

ACKNOWLEDGMENTS

Any endeavor of this magnitude requires the help and encouragement of many people. This is particularly true for an experimental thesis undertaken while working full time. I must thank first and foremost Jack Parker, Phyllis Russo and Howard Menlove, colleagues with whom I worked when I first came to the Los Alamos National Laboratory and have continued to interact with over the years. It was their initial encouragement that led me to conclude that I could and should pursue a doctoral degree and their support has been an inspiration to me. Additionally, I would like to thank Phyllis for carefully proofreading the manuscript in its draft form. I owe a debt of gratitude to Roger Byrd and Merlyn Krick for serving on my committee, engaging in the many enlightening conversations and consultations, and proofreading, all of which encroached on their already overloaded schedules This work could not have been performed without the help of Bill Feldman, who graciously gave his detectors up for this study. Bill also provided many insightful conversations, especially in the conceptual design of the pulse-separation electronics. Norbert Ensslin provided support as my supervisor during his tenure as Deputy Group Leader of the Safeguards Science and Technology group and also provided the figure-of-merit code used for the

assay variance estimates. A special note of thanks goes out to the current Safeguards Science and Technology group management, Avigdor Gavron (Group Leader) and Mark Pickrell (Deputy Group Leader). Their encouragement and support during the final phases of this project was critical to its completion.

A number of individuals participated in various aspects of this project and their help was essential to its success. The constant fraction discriminator/gated integrator circuitry shares a common heritage with a series of instruments designed for space applications, including the original development of the BC454 detector material. Ken Fuller and Jerry Longmire are the principals in the design of these circuits and Jerry led the latest effort, incorporating the relevant changes needed for this investigation. The time-tag module was conceived and specified with the help of Steve Bourret, Rod Biddle, and Martin Sweet. Steve did the design work and aided in the post-fabrication diagnostics. The data-acquisition software was specified with the help of Rod Biddle and Martin Sweet. Martin wrote the software for the Time-Tag Module interface, while Rod wrote the software for the Analog-to-Digital Converter interface and performed system integration. Greg Walton did the mechanical design for the sample chamber and auxiliary laboratory items, while Ted Dye and Dave Garcia fabricated them. Electronics support was provided by Steve Salazar, Becky Cordova, Danny Roybal, and the Space Engineering fabrication shop. Finally, I would like to thank Bill Harker for his C-programming consultations.

Genara Jaramillo and Celina Ortiz helped with word-processing consultation and final figure production. Illustration support was provided by Florence Fujita and

Amos Romero. Thanks goes out to you all for helping to create a professional-looking manuscript.

Financial support was provided by the Los Alamos National Laboratory's Nonproliferation and International Security division and the Department of Energy's Nonproliferation and National Security division, Office of Research and Development.

TABLE OF CONTENTS

PAGE

LIST OF FIGURES

PAGE

LIST OF TABLES

PAGE

NEUTRON DETECTION AND MULTIPLICITY COUNTING USING A BORON-LOADED PLASTIC SCINTILLATOR/BISMUTH GERMANATE PHOSWICH DETECTOR ARRAY

Michael Conrad Miller

ABSTRACT

Neutron detection and multiplicity counting has been investigated using a boron-loaded plastic scintillator/bismuth germanate phoswich detector array. Boron-loaded plastic combines neutron moderation (H) and detection (^{10}B) at the molecular level, thereby physically coupling increasing detection efficiency and decreasing die-away time with detector volume. Both of these characteristics address a fundamental limitation of thermal-neutron multiplicity counters, where ^{3}He proportional counters are embedded in a polyethylene matrix.

Separation of the phoswich response into its plastic scintillator and bismuth germanate components was accomplished on a pulse-by-pulse basis using custom integrator and timing circuits. In addition, a custom time-tag module was used to provide a time for each detector event. Analysis of the combined energy and time event stream was performed by calibrating each detector's response and filtering based

on the presence of a simultaneous energy deposition corresponding to the ^{10}B(n,alpha) reaction products in the plastic scintillator (93 keV_{ee}) and the accompanying neutron-capture gamma ray in the bismuth germanate (478 keV). Time-correlation analysis was subsequently performed on the filtered event stream to obtain shift-register-type singles and doubles count rates.

Proof-of-principle measurements were conducted with a variety of gamma-ray and neutron sources including ^{137}Cs, ^{54}Mn, AmLi, and ^{252}Cf. Results of this study indicate that a neutron-capture probability of ~10% and a die-away time of ~10 μs are possible with a 4-detector array with a detector volume of 1600 cm^3. Simulations were performed that indicate neutron-capture probabilities on the order of 50% and die-away times of less than 4 μs are realistically achievable. While further study will be required for practical application of such a detection system, the results obtained in this investigation are encouraging and may lead to a new class of high-efficiency, short die-away time neutron multiplicity counters capable of extending current non-destructive assay methods for special nuclear materials.

1. INTRODUCTION

1.1. OVERVIEW

Neutron detection and multiplicity counting has been investigated using a boron-loaded plastic scintillator/bismuth germanate phoswich detector array. Boron-loaded plastic combines neutron moderation (H) and detection (^{10}B) at the molecular level, thereby physically coupling increasing detection efficiency and decreasing die-away time with detector volume. Both of these characteristics address a fundamental limitation of thermal-neutron multiplicity counters, where ^{3}He proportional counters are embedded in a polyethylene matrix. This study used detectors that were previously conceived of and fabricated, but never tested or calibrated prior to this work. The goal of this research was to demonstrate basic neutron detection and multiplicity counting using these detectors by 1) decomposing the phoswich response into its component parts, 2) using spectral discrimination techniques to identify neutron events, and 3) applying time-correlation analysis to the filtered data.

Separation of the phoswich response into its plastic scintillator and bismuth germanate components was accomplished on a pulse-by-pulse basis using custom integrator and timing circuits. In addition, a custom time-tag module was used to provide a time for each detector event. Analysis of the combined energy and time event stream was performed by calibrating each detector's response and filtering based on the presence

of a simultaneous energy deposition corresponding to the $^{10}B(n,alpha)$ reaction products in the plastic scintillator (93 keV_{ee}) and the accompanying neutron-capture gamma ray in the bismuth germanate (478 keV). Time-correlation analysis was subsequently performed on the filtered event stream to obtain shift-register-type singles and doubles count rates.

Proof-of-principle measurements were conducted with a variety of gamma-ray and neutron sources including ^{137}Cs, ^{54}Mn, AmLi, and ^{252}Cf. Results of this study indicate that a neutron-capture probability of ~10% and a die-away time of ~10 μs are possible with a 4-detector array with a detector volume of 1600 cm^3. Simulations were performed that indicate neutron-capture probabilities on the order of 50% and die-away times of less than 4 μs are realistically achievable. While further study will be required for practical application of such a detection system, the results obtained in this investigation are encouraging and may lead to a new class of high-efficiency, short die-away time neutron multiplicity counters capable of extending current non-destructive assay methods for special nuclear materials.

1.2. MOTIVATION

The need to assure the proper use of special nuclear materials (SNM) is motivated by the fact that uranium and/or plutonium are necessary ingredients of all nuclear weapons. Domestic materials control and accountancy (MC&A) programs rely on access control, surveillance, and seals, as well as on quantitative measurements in the implementation of nuclear materials safeguards. These programs are carried out by the

Department of Energy (DOE) and the Nuclear Regulatory Commission (NRC). Civilian nuclear fuel cycle facilities are overseen by the NRC, while the DOE has primary responsibility for the nuclear weapons complex. The DOE also has the lead role in research and development activities for domestic and international safeguards programs.

As part of the Nonproliferation Treaty (NPT), signatory states agree to allow inspection activities to be conducted in their countries. The International Atomic Energy Agency (IAEA), a part of the United Nations, is tasked with the verification activities required by this treaty. Traditional IAEA safeguards have focused on the verification of declared nuclear programs within NPT countries as well as within countries that have bilateral safeguards agreements. Recent experiences with Iraq's clandestine nuclear weapons program, as well as with other states such as South Africa, have motivated expansion of the role of the IAEA to include the detection, and therefore hopefully the prevention, of undeclared nuclear programs. Techniques employed by the IAEA are similar to those for domestic MC&A programs and include surveillance, seals, and measurements of nuclear materials.

Of particular importance in domestic and international safeguards are quantitative measurements by nondestructive means because of the much less intrusive nature of such methods compared to destructive (i.e., chemical) techniques. Materials such as uranium and plutonium lend themselves to this type of assay because of the penetrating radiations, neutron and gamma rays in particular, that arise from their decay. As a result, nondestructive assay (NDA) methods based on neutron and gamma-ray signatures have been developed and applied to a wide variety of uranium- and plutonium-bearing materials, such as bulk powders and pellets, fuel pins, and finished fuel assemblies.

The boron-loaded plastic scintillator/bismuth germanate detector system offers the potential to benefit traditional assay requirements in nuclear materials safeguards through its intrinsically high neutron detection efficiency and short average neutron lifetime (die-away time).

1.3. MULTIPLICITY COUNTING

One of the primary techniques employed in nuclear materials safeguards measurements is thermal-neutron coincidence counting.[1] This technique is based on time-correlation counting using shift-register electronics to distinguish sources of fission neutrons from sources of non-correlated neutrons. Counting efficiency is enhanced by moderation of the neutrons prior to detection in ^{3}He proportional counters. The moderator also serves as a neutron reservoir, which is critical in the timing characteristics of the system. Because the ^{3}He detectors are discretely placed in the moderator, the average neutron lifetime (die-away time) in these types of counters is ~50 μs. The thermal-neutron coincidence counter in its most common form measures singles and doubles events, representing the zeroth and first reduced factorial moments of the fission multiplicity distribution, and it either incorporates an empirical, non-linear calibration function or assumes some knowledge of sample characteristics to relate the measured count rates to sample mass. In principle, extension of the technique to higher moments allows for analytical determination of sample mass without requiring *a priori* knowledge of the sample.[2,3,4] The practical limitation of this method using conventional thermal-neutron counters is that the statistical precision degrades rapidly for higher moments

because of accidental counts caused by non-correlated neutrons, primarily from (alpha,n) reactions. This situation restricts the applicability of thermal-neutron multiplicity counters to relatively pure materials and low (alpha,n) rates.

1.3.a. RADIATION SIGNATURES

The property of radioactivity provides the physical basis by which radionuclides may be identified and quantitatively assayed. Radioactive decay can result in the emission of energetic charged particles, photons, and neutrons, often in combination. Decay products and their energy distributions are characteristic of the parent nuclide. Because of their low penetrability, charged products such as alpha and beta particles are of limited use in NDA techniques, where the goal is to perform a measurement in situ, without containment breach. On the other hand, neutrons and gamma rays are quite penetrating and make suitable radiation signatures for NDA, especially in the case of actinides such as uranium and plutonium.

Gamma rays are electromagnetic radiation of nuclear origin and result from energy transitions within excited nuclei, most often following alpha or beta decay. Gamma rays are also emitted in the fission process and as the result of nuclear reactions such as (n,n'γ), (p,nγ), etc. X rays are also electromagnetic radiation, but they originate from atomic, rather than nuclear, transitions. As such, x rays are characteristic of the element of their origin, whereas gamma rays are isotope-specific. Gamma rays and x rays arising from radioactive decay are the most useful sources for the assay of uranium and plutonium, and they form the basis of techniques for isotopic and mass analyses.[5]

Gamma-ray methods are generally attenuation-limited and are therefore best suited for small samples when a quantitative determination of mass is desired.

Neutrons are primarily produced as a result of nuclear reactions such as (p,n), (γ,n), (alpha,n), and induced fission. Spontaneous fission is a special, although relatively rare, decay event that results in neutron emission. Neutrons are also produced by spallation from cosmic-ray induced interactions. Fission (spontaneous and induced) and (alpha,n) reactions are the primary neutron sources of interest in the case of SNM measurements. During the fission process of uranium and plutonium, 2–3 neutrons are emitted on average. In contrast, (alpha,n) reactions produce neutrons one at a time. Neutron energies are not discrete, as is the case for gamma rays, because their emission involves a binding energy threshold rather than a transition between two states. This fact and their electrically neutral character make neutron spectroscopy difficult compared to gamma-ray spectroscopy.

Table 1-1 presents the spontaneous fission neutron yields for several isotopes relevant to nuclear safeguards. As can be seen from Table 1-1, the spontaneous fission yield is much greater for plutonium than uranium and is quite large in the case of ^{252}Cf. Spontaneous fission yields for plutonium suggest the definition of a quantity called the "^{240}Pu-effective mass". This quantity is the mass of ^{240}Pu that would have the same neutron output as the masses of all of the even isotopes combined, and it is given by

$$^{240}\mathrm{Pu}_{\mathrm{eff}} = 2.54\,^{238}\mathrm{Pu} + {}^{240}\mathrm{Pu} + 1.69\,^{242}\mathrm{Pu}, \qquad (1\text{-}1)$$

where the coefficients are the ratios of the yields in Table 1-1. Normalization to the ^{240}Pu isotope is based on ^{240}Pu being the major component of the even isotopes in most cases

(^{238}Pu heat sources are an exception). Neutron yields from spontaneous fission in plutonium are sufficient to provide a basis of measurement in the passive mode for even sub-gram samples. Uranium must be present in kilogram quantities for the practical application of neutron counting techniques based on spontaneous fission. The high yield of ^{252}Cf makes it a good source of fission neutrons in very small (nanogram or microgram) quantities. As such, it is a good reference source (nanogram) and a compact interrogation source (microgram and above).

Table 1-1. Spontaneous Fission Neutron Yields

Isotope	Total half-life (yr.)	Spontaneous fission half-life (yr.)	Spontaneous fission yield (n/s-g)	Spontaneous fission multiplicity ($\bar{\nu}$)
^{234}U	2.45×10^{5}	2.1×10^{16}	0.005	1.81
^{235}U	7.04×10^{8}	3.5×10^{17}	0.0003	1.86
^{236}U	2.34×10^{7}	2.0×10^{16}	0.0055	1.91
^{238}U	4.47×10^{9}	8.2×10^{15}	0.0136	2.01
^{238}Pu	87.74	4.8×10^{10}	2590.	2.21
^{239}Pu	2.41×10^{4}	5.5×10^{15}	0.0218	2.16
^{240}Pu	6.56×10^{3}	1.2×10^{11}	1020.	2.16
^{241}Pu	14.35	2.5×10^{15}	0.05	2.25
^{242}Pu	3.79×10^{5}	6.8×10^{10}	1720.	2.15
^{241}Am	433.6	1.1×10^{14}	1.18	3.22
^{252}Cf	2.646	85.5	2.34×10^{12}	3.76

(Adapted from Ref. 1, pg. 339)

Materials containing uranium and plutonium found in the nuclear fuel cycle, and therefore important to safeguards, are in the form of oxides, fluorides, carbides, and metals. The combination of alpha decay and reactions in low-Z matrices gives rise to a source of neutrons via the reaction:

$$ {}^{A}_{Z}\mathrm{X}(\mathrm{alpha},\mathrm{n})^{A+3}_{Z+2}\mathrm{Y}, $$

where X is a low-Z element. These (alpha,n) neutrons are important to measurements of uranium and plutonium because they are usually an unwanted background source that must be subtracted. This correction is needed because their rate is dependent on chemical form and therefore not directly proportional to the mass of uranium or plutonium. Yields for PuO_2 are significantly larger than for UO_2, and they are of sufficient magnitude to constitute a non-negligible component of the total neutron output.

Neutrons from (alpha,n) reactions are not always an unwanted artifact that must be corrected for; they are often used as an interrogation source to induce fission in uranium (active methods). Figure 1-1 shows the fission cross section as a function of incident neutron energy for U and Pu isotopes. AmLi is well suited as an interrogation source because the energy of most emitted neutrons is sub-threshold for fission in ^{238}U. This feature allows for selective interrogation of ^{235}U in the sample. For very large quantities of material, an enrichment measurement could be carried out by combining passive counting (^{238}U) and active interrogation (^{235}U). Uranium hexafluoride can provide its own source of interrogation neutrons through (alpha,n) reactions on fluoride. These neutrons cause subsequent fission in the uranium, which can then be counted.

Neutron assay techniques that do not employ energy discrimination directly must rely on other means to separate out fission (spontaneous or induced) from (alpha,n) contributions. Fission neutrons are emitted in bursts of 0–8, with the average being 2–3. The probability of ν neutrons being emitted is given by the density function, $P(\nu)$. Neutrons are produced singly in (alpha,n) reactions. The multiplicity of fission and

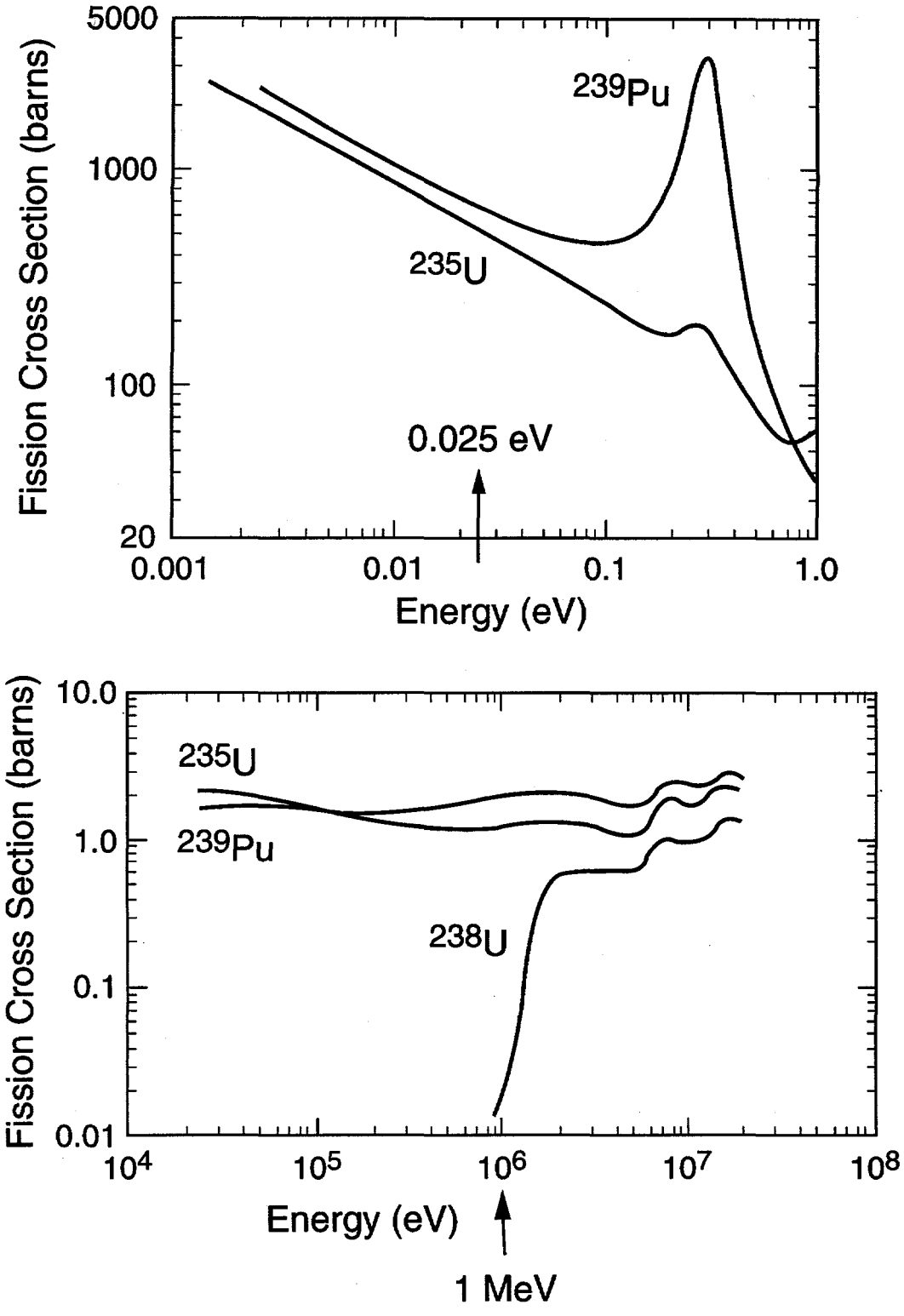

Figure 1-1. Fission Cross Sections for ^{235}U, ^{238}U, and ^{239}Pu

(alpha,n) reactions provides a basis for discrimination between them. Neutrons emitted during a $\nu > 1$ event, e.g., fission, will be related to one another in time. Neutrons arising from separate $\nu = 1$ events, e.g., (alpha,n) reactions, will not be time-related. This realization led to the investigation of time-correlation, or coincidence, counting methods for assay of spontaneous-fission and fissionable materials (e.g., plutonium and uranium).

Table 1-2 contains the prompt-fission neutron multiplicities for ^{235}U (induced), ^{240}Pu, and ^{252}Cf (spontaneous).[6] If an (alpha,n) reaction were to be included in the table, it would have only 2 entries, $P(0) = 0$ and $P(1) = 1$, because the (alpha,n) reaction produces exactly one neutron. The average values of ν, $\nu(\nu\text{-}1)$, and $\nu(\nu\text{-}1)(\nu\text{-}2)$ in Table 1-2 represent the first, second, and third factorial moments of the neutron multiplicity distribution. These quantities are important in coincidence counting techniques.

Table 1-2. Prompt Fission Multiplicity Distributions

ν	^{235}U $P(\nu)$	^{240}Pu $P(\nu)$	^{252}Cf $P(\nu)$
0	0.033	0.066	0.002
1	0.174	0.232	0.026
2	0.335	0.329	0.127
3	0.303	0.251	0.273
4	0.123	0.102	0.304
5	0.028	0.018	0.185
6	0.003	0.002	0.066
7			0.015
8			0.002
$\bar{\nu}$	2.406	2.156	3.757
$\overline{\nu(\nu-1)}$	4.626	3.825	11.962
$\overline{\nu(\nu-1)(\nu-2)}$	6.862	5.336	31.812

1.3.b. SHIFT-REGISTER ELECTRONICS

The shift-register circuit is the most widely used time-correlation technique in nuclear safeguards measurements. This circuit is sensitive to pulses that occur close in time relative to a coincidence-gate length. The outputs of each of the ^{3}He detectors in a thermal-neutron coincidence counter pass through a discriminator and logic-pulse generation circuit and are subsequently combined to form a single digital pulse train. Each pulse corresponds to a detected neutron. This pulse train is then processed by the shift-register electronics unit, where counts arising from fission are separated from the random background. By incorporating early and late coincidence gates, the shift register effectively samples the pulse train in pulse-triggered mode and in random mode. The contents of the pulse-triggered count distribution are a combination of true (real) and chance (accidental) coincidences, while the randomly triggered count distribution contains only chance coincidences. Single, double, and triple correlations are obtained by taking the zeroth, first, and second reduced factorial moments of these two distributions.

Originally proposed by Böhnel,[7] designed by Stevens et al.,[8] and later improved by Swansen et al.,[9] this circuit shifts the incoming pulses through a storage register at a rate determined by a clock. When a pulse has gone through all stages of the register, it has been in the circuit for the gate length. For example, a 256-stage shift register operating at 4 MHz (250 ns/stage) will define a gate of 64 μs. A 32-μs gate would use a 128-stage register operated at 4 MHz. One great advantage of the shift-register method is that it is free of deadtime. All losses occur prior to entering the circuit, and the only count-rate limitation is the clock rate compared to the incoming pulse rate. The number

of doubles counts resulting from shift-register counting of N events spaced closely in time (compared to the gate length) is the total number of pair-wise combinations,

$$\binom{N}{2} = \frac{N(N-1)}{2}. \tag{1-2}$$

This result is demonstrated in Fig. 1-2. Pulses #1, #2, #3, and #4 are closely spaced and result in a total of 6 doubles counts. Pulse #1 yields 3 counts, pulse #2 yields 2 counts, pulse #3 yields 1 count, and pulse #4 yields no counts, for a total of 6 counts. In this case N is equal to 4. A single, isolated pulse will not produce a correlated count. Note that it is possible to obtain more counts than pulses (i.e., detected neutrons) with this approach. The total neutron count in Fig. 1-2 is 4, while the doubles count is 6. This effect is simply an artifact of the shift register and does not have physical significance.

Analogously, the number of triple counts observed from shift-register counting closely-spaced events is given by

$$\binom{N}{3} = \frac{N(N-1)(N-2)}{3!}, \tag{1-3}$$

which represents the number of three-way combinations of N counts. Applying Eq. 1-3 to the 4-pulse example given above results in 4 triples counts. Illustration of Eq. 1-3 using the pulse train in Fig. 1-2 requires taking the second reduced factorial moment of the count distribution, which is discussed in detail in Sec. 1.3.c below. The process of summing the number of counts in the gate after triggering by each count, as was done in the doubles example above, is equivalent to taking the first reduced factorial moment of the count distribution.

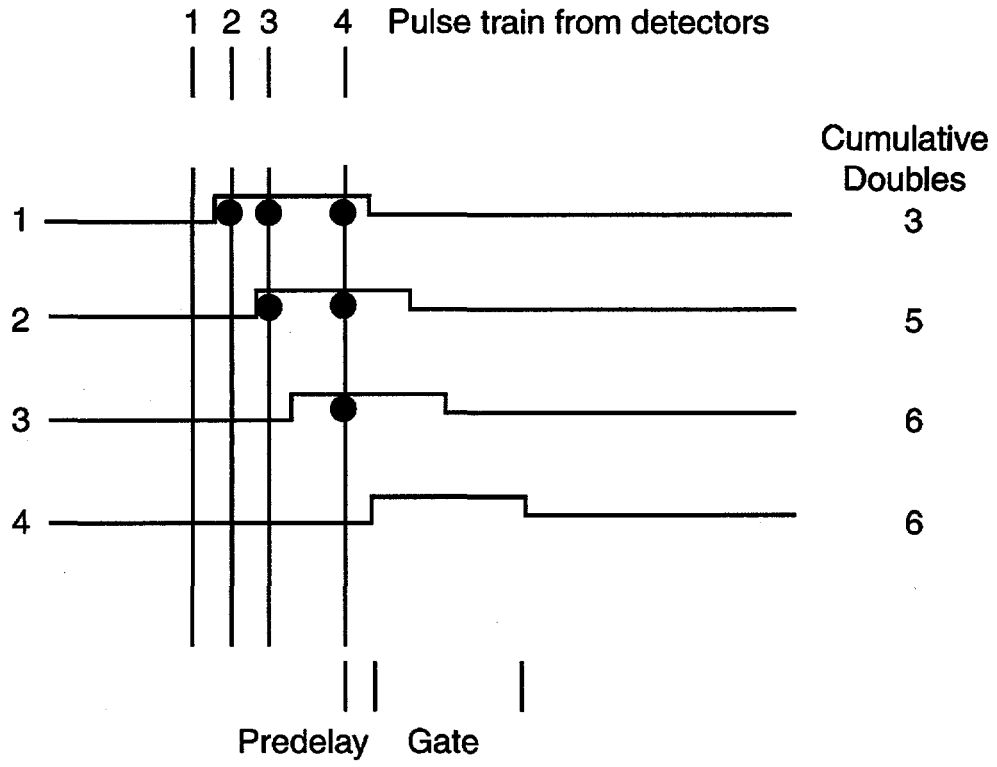

Figure 1-2. Example Pulse Train and Resulting Correlated Counts

Not all closely spaced pulses are from the same fission. Chance, or accidental, coincidences will occur as a function of the total counting rate and gate length and must be subtracted. This correction is accomplished by analyzing the pulse train using early and late coincidence gates. Figure 1-3 is a conceptual diagram of neutron detection probability versus time with gate information superimposed (Rossi-Alpha distribution)[10]. The top curve represents the exponential neutron lifetime in a thermal-neutron coincidence counter. Single-exponential decay is a reasonable model for these counters when they have an inner cadmium liner (the typical case) and optimal placement of the ^{3}He detectors in the moderator. Pulses being processed by the shift register will go through two gates, one early and the other late. During the early gate, both true (real) and accidental coincidences may register. This gate is known as the R+A (Reals + Accidentals) gate. If the late gate is delayed sufficiently long relative to the die-away time, then only accidental coincidences will be counted. This gate is called the A (Accidentals) gate. For thermal-neutron coincidence counters, where the average die-away time is 50 μs, a delay of, for example, 1 ms is used. This delay corresponds to an extremely low probability (on the order of e^{-20}) of counting a real coincidence in the accidental gate because of the exponential nature of the neutron die-away time.

Figure 1-4 shows a block diagram of a shift-register circuit. Pulses enter the circuit and proceed through a derandomizing buffer, the coincidence gate, the predelay (~4 μs), and finally the long delay. The derandomizing buffer stores pulses when they arrive at the circuit closer in time than the shift register can handle (e.g., 250 ns for a 4 MHz clock). The buffer is actually a fast counter that counts up (15 maximum)

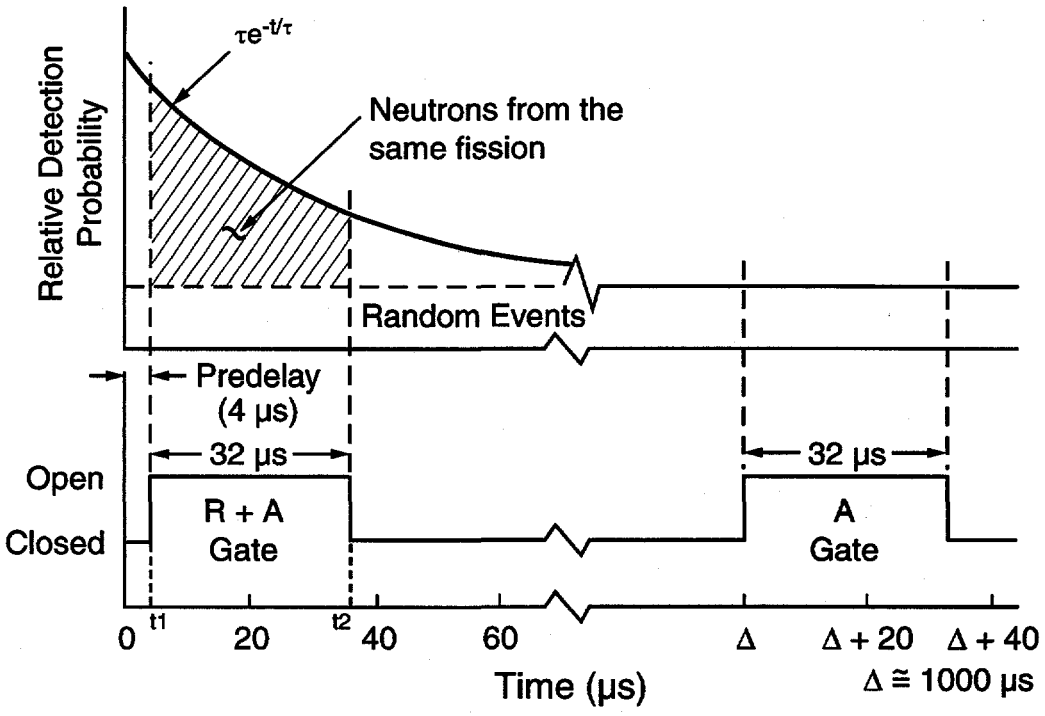

Figure 1-3. Rossi-Alpha Event Distribution

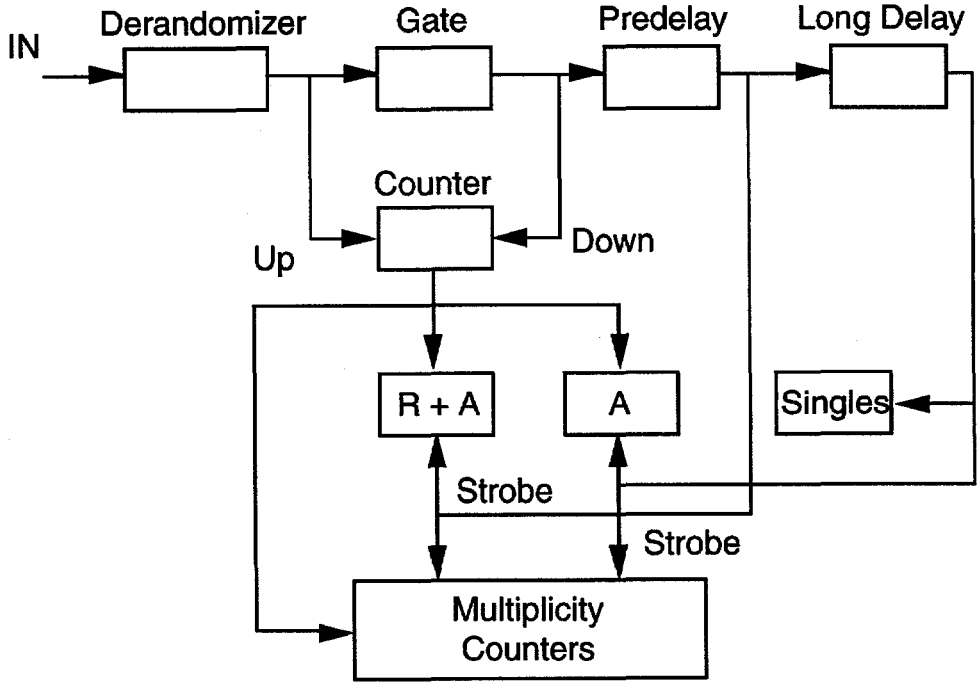

Figure 1-4. Block Diagram of Shift Register Circuit with Multiplicity

when pulses enter and then counts down (at the clock rate) to send pulses into the shift register. This approach is required because the pulse-pair resolution is ~20 ns and the pulse width is 50 ns, making it possible for more than one event to arrive at the shift register within 250 ns. The predelay is employed so that the deadtime characteristics of the early (R+A) and late (A) gates are the same. If a predelay is not used, a negative bias will result because there will be more loss in the R+A gate than the A gate. As pulses enter the coincidence gate, the up/down counter is incremented. When pulses leave, the up/down counter is decremented. Each time a pulse passes through the predelay, the R+A scaler is strobed to obtain the contents of the up/down counter (pulse trigger). This accumulator contains real and accidental coincidences. The A scaler is strobed after the delay and therefore contains only accidental coincidences (random trigger). Singles counts are also accumulated after the long delay. Net doubles counts are obtained by subtraction of the R+A and A scalers. In addition to the R+A and A scalers, multiplicity scalers record the number of times n counts (n ranging from 0 to 255 for current hardware) were observed in the R+A and A gates. Recording the multiplicity distribution allows the calculation of higher moments (e.g., triples), required for a more robust analysis.

1.3.c. MULTIPLICITY ANALYSIS

A theoretical framework that allows a general, analytic expression of the results of counting neutrons (correlated and noncorrelated) using the shift-register was developed

by Hage and Cifarelli.[11] The resulting equations using the moments derived by Böhnel[12] are referred to as the point equations of neutron coincidence counting and are given by

$$S = mF\varepsilon M\nu_{s1}(1+\alpha), \tag{1-4}$$

$$D = \frac{mF\varepsilon^2 f_d M^2}{2}\left[\nu_{s2} + \left(\frac{M-1}{\nu_{i1}-1}\right)\nu_{s1}(1+\alpha)\nu_{i2}\right], \text{ and} \tag{1-5}$$

$$T = \frac{mF\varepsilon^3 f_t M^3}{3!}\left\{\begin{array}{l}\nu_{s3} + \left(\frac{M-1}{\nu_{i1}-1}\right)\left[3\nu_{s2}\nu_{i2} + \nu_{s1}(1+\alpha)\nu_{i3}\right] \\ +3\left(\frac{M-1}{\nu_{i1}-1}\right)^2 \nu_{s1}(1+\alpha)\nu_{i2}^2\end{array}\right\}, \tag{1-6}$$

where

S = singles rate,

D = doubles rate,

T = triples rate,

m = plutonium-240 effective mass ($m = 2.52^{238}\text{Pu} + ^{240}\text{Pu} + 1.68^{242}\text{Pu}$),

F = spontaneous fission rate per unit mass m,

ε = detection efficiency,

M = neutron net leakage multiplication,

α = (alpha,n)-to-spontaneous-fission neutron ratio,

f_d = fraction of doubles events in the gate,

f_t = fraction of triples events in the gate,

ν_{s1}, ν_{s2}, ν_{s3} = first, second, and third factorial moments of the spontaneous fission neutron multiplicity distribution, and

ν_{i1}, ν_{i2}, ν_{i3} = first, second, and third factorial moments of the induced fission neutron multiplicity distribution.

The definition of the plutonium-240 effective mass differs slightly from that given earlier because the effects of multiplicity are included, whereas Eq. 1-1 is based on total neutron output. The parameters ε, f_d, and f_t are detector constants and can be measured with a known ^{252}Cf source (a small adjustment is made for the energy-spectrum difference for plutonium), whereas F, ν_{s1}, ν_{s2}, ν_{s3} ν_{i1}, ν_{i2}, and ν_{i3} are nuclear data (the energy dependence on induced fission multiplicity is ignored for this application). Thus the problem is reduced to a solvable level: three unknowns (m, M, and α) and three equations (S, D, and T). Appendix A shows an example of the solution to the point equations for neutron coincidence counting.

Assumptions made in the point equations include: 1) the neutron detection efficiency is a constant, 2) fission chains can be considered simultaneous (superfission concept) because of the long die-away time of the counter, and 3) fission probability is constant within the sample and independent of incident neutron energy.

Under certain circumstances, the required number of measurements can be reduced to two (singles and doubles) by the elimination of one of the neutron-production variables. The most common situation is the elimination of α, a situation that is possible if the chemical composition of the sample is known. This "known Alpha" approach has been particularly successful when applied to the measurement of bulk PuO_2.[13] In contrast, samples such as fuel pins and fuel assemblies, where the physical parameters such as

geometry and density are known and constant, lend themselves to elimination of the variable M, hence the "known M" method.[14]

An example multiplicity distribution is shown in Table 1-3. The count rates in Table 1-3 are obtained by taking the zeroth, first, and second reduced factorial moments of the reals plus accidentals and the accidentals multiplicity distributions as follows (neglecting deadtime and background effects):

$$S = \sum_{i=0}^{\max} A_i \ , \tag{1-7}$$

$$D = S\left[\sum_{i=1}^{\max} i(p_i - q_i)\right], \text{ and} \tag{1-8}$$

$$T = S\left[\sum_{i=2}^{\max} \frac{i(i-1)}{2}(p_i - q_i) - \sum_{i=1}^{\max} i(p_i - q_i)\sum_{i=1}^{\max} iq_i\right], \tag{1-9}$$

where

$$p_i = \frac{(R+A)_i}{\sum_{0}^{\max}(R+A)_i} \text{ and} \tag{1-10}$$

$$q_i = \frac{A_i}{\sum_{0}^{\max} A_i} \tag{1-11}$$

are the probabilities for multiplicity i in the R+A and A scalers respectively. Derivation of these equations can be found in Appendix B.

The multiplicity distribution for the pulse train given in Fig. 1-2 is shown below.

Multiplicity	R
0	1
1	1
2	1
3	1

There are no accidentals in this case because all four neutrons are from the same fission event. The equations for singles, doubles, and triples given above simplify to just taking the zeroth, first, and second reduced factorial moments of the multiplicity distribution and reduce to

$$S = \sum_{i=0}^{3} R_i \ , \tag{1-12}$$

$$D = S \sum_{i=1}^{3} i r_i \ , \tag{1-13}$$

$$T = S \sum_{i=2}^{3} \frac{i(i-1) r_i}{2} \ , \tag{1-14}$$

where

$$r_i = \frac{R_i}{\sum_{i=0}^{3} R_i} \ . \tag{1-15}$$

Substituting gives $S = 4$, $D = 6$, and $T = 4$, the same values obtained earlier in Sec. 1.3.b.

Instrumentation has been developed for passive and active multiplicity counting of plutonium and uranium.[15,16] For active multiplicity, the theory is somewhat different than that given above because the coupling of the interrogation source (e.g., AmLi) to the sample must be accounted for (i.e., probability of inducing fission in ^{235}U by the

interrogation source). Also, the term α is negligible and the resulting equations are simpler. Appendix C contains the point equations for active multiplicity counting.

Table 1-3. Example Multiplicity Distribution

Multiplicity	$R+A$	A
0	329308	344585
1	272831	271135
2	119237	111695
3	36359	32227
4	8899	7542
5	1899	1495
6	354	230
7	64	36
8	15	18
9	2	2
10	0	0
Singles (S)	Doubles (D)	Triples (T)
25634	1251	123

The primary limitation of thermal-neutron multiplicity counters is that the precision of the triples degrades rapidly with high accidentals rates (high α), restricting the application of the method to relatively pure materials and $\alpha \leq 5$. A detection system capable of high efficiency while maintaining a low die-away time would allow this limitation to be addressed. High efficiency is required because of the ε^3 dependence of the triples rate. A shorter die-away time will allow shorter coincidence gates to be used and will result in fewer accidental counts. A detector that promises to fit these criteria is the boron-loaded plastic scintillator.

1.4. BORON-LOADED PLASTIC SCINTILLATORS

The boron-loaded plastic scintillator (BC454*) was developed for the purpose of measuring neutron energy spectra.[17] Fast neutrons interact with the plastic, scatter and lose energy, and then terminate by capture with an (n,alpha) reaction on ^{10}B. Scattering interactions result in proton recoils on a time scale of <30 ns, while the capture reaction occurs with a die-away time of ~2 μs. The much shorter die-away time (compared to the thermal-neutron counters discussed above) occurs because the boron is intimately mixed with the plastic; therefore regardless of where a neutron is in the detector when it slows down, a ^{10}B nucleus is nearby. Identification of a neutron event is accomplished by coincidence counting of the proton recoils and captures within a few-microsecond gate. Because the probability of capture is very high for slow neutrons (and very low for fast neutrons), the proton recoil pulse height represents the neutron's energy and may therefore be used for neutron spectrometry. This detector material is naturally suited to the requirement to address the limitations of thermal-neutron multiplicity counting because of its intrinsically short die-away time and capability for high detection efficiency (capture by ^{10}B dominates).

1.4.a. DETECTION PHYSICS

First introduced by Drake et al.[18] and subsequently reported in more detail by Feldman et al.[19] and Byrd et al.,[20] BC454 was originally designed for purposes of neutron

---

* Bicron Corp., 12345 Kinsman Rd., Newbury, OH 44065.

spectroscopy in space environments. Because plastic scintillators respond with very similar pulse shapes to protons, gamma rays, and neutrons, boron was added to the plastic to act as a neutron event identifier. Neutrons enter the plastic and elastically scatter (primarily on hydrogen), thereby creating proton recoils. These proton recoils result in the production of scintillation light ($\lambda \approx 425$ nm). Gamma rays also cause scintillation, primarily by Compton scattering. Light produced by either neutrons or gamma rays is collected with a photomultiplier tube (PMT). With boron added to the plastic, neutron capture can occur by the ^{10}B(n,alpha)^{7}Li reaction, where Q = 2.791 MeV. The first excited state of ^{7}Li is produced 94% of the time and decays by emission of a 478-keV gamma ray. For plastic containing 5% by weight boron (~1% ^{10}B), capture by ^{10}B will dominate the neutron absorption (>98%). The proton recoils occur faster than the response time of the PMT (~30 ns) and are collected as a single pulse. Neutrons that have been moderated diffuse in the plastic and are captured by the ^{10}B with a time constant given approximately by

$$\tau = \frac{1}{n_{10}\sigma\upsilon}, \tag{1-16}$$

where n_{10}, σ, and υ are the ^{10}B atom density, (n,alpha) cross section, and neutron speed, respectively. For plastic containing 5% by weight boron, $\tau \approx 2\ \mu s$. The time constant is essentially constant because of the $1/\upsilon$ behavior of σ for ^{10}B at the energies of interest. The reaction products (α and ^{7}Li) deposit their energy locally in the plastic, producing a light output of approximately 93 keV electron equivalent (keV_{ee}). The unit keV_{ee} represents the pulse height (light output) that an electron of 1 keV would produce. As such, it forms a basis of comparison for pulse heights arising from different particles (n,

γ, alpha, etc.) detected by the scintillator (light production efficiency varies with particle type). The gamma ray emitted by the excited ^{7}Li may or may not deposit energy in the plastic. Because the capture reaction occurs most probably for slow neutrons, the proton recoil pulse is a record of the neutron's total energy (discussed below). Figure 1-5 is an example of the spectrum for the ^{10}B capture reaction (second-pulse spectrum).[21] Note the large capture peak at 93 keV_{ee} (alpha and ^{7}Li absorption), the broad continuum extending from about 150–400 keV_{ee} (alpha, ^{7}Li absorption, and Compton scatter of the 478-keV gamma ray), and finally a "Compton edge" at 404 keV_{ee} (alpha, ^{7}Li absorption, and 478-keV Compton scatter with $\theta = 180°$).

1.4.b. NEUTRON SPECTROSCOPY

By counting the first pulse (recoil) and second pulse (capture) in coincidence, one can isolate only those events that 1) were of neutron origin and 2) deposited all of their energy. Figure 1-6 is a time-difference spectrum of first- and second-pulse events (proton recoils and captures respectively).[22] Note the exponential decay with a time constant of 2.3 μs. To subtract out accidental coincidences, early and late windows are used (similar in concept to the early and late gates in the shift register). The early window is shown from 0.5–3.5 μs, while the late window extends from roughly 18–25 μs. As can be seen from Fig. 1-6, there are essentially no true coincidences in the late window.

In addition to being used in space applications, the BC454 detector has been applied as a spectrometer for fission sources and as a search tool for neutron sources.[23,24,25]

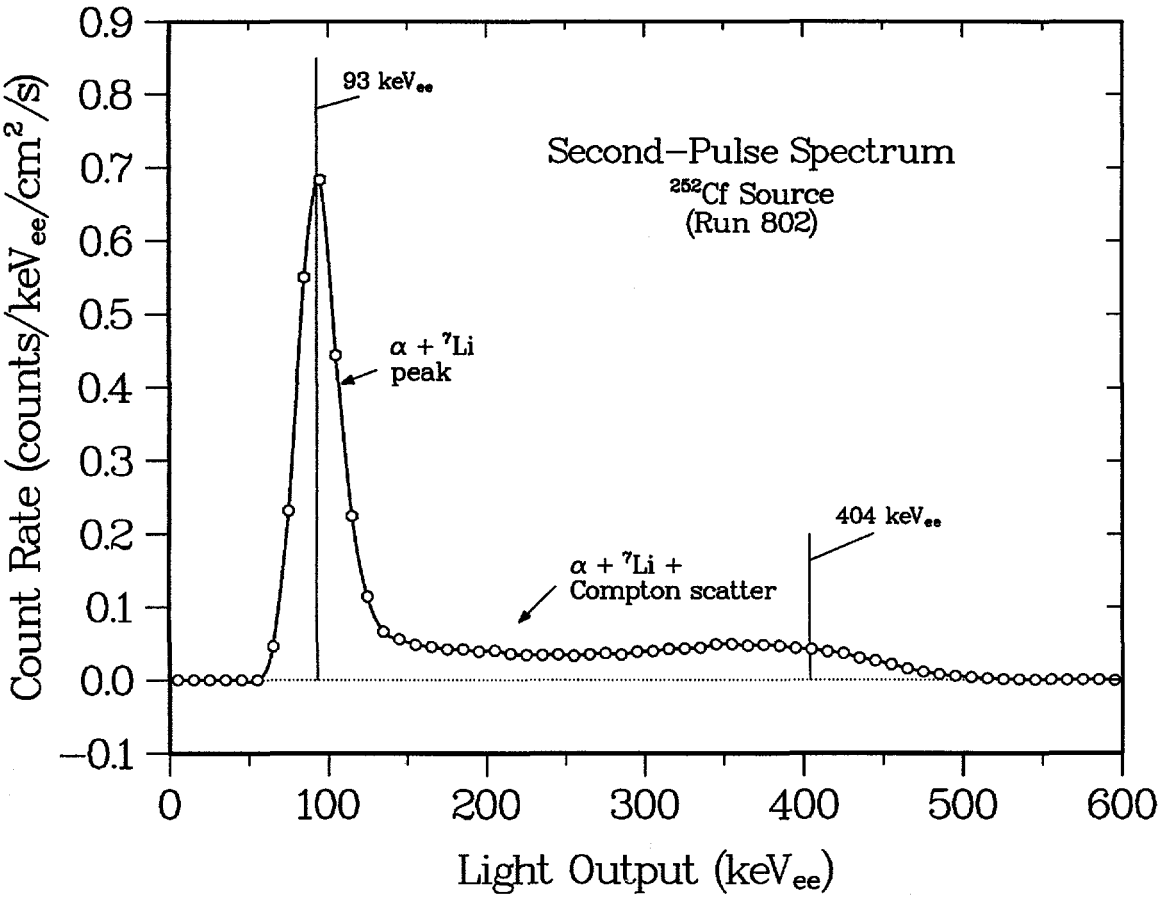

Figure 1-5. Neutron Capture Spectrum of BC454

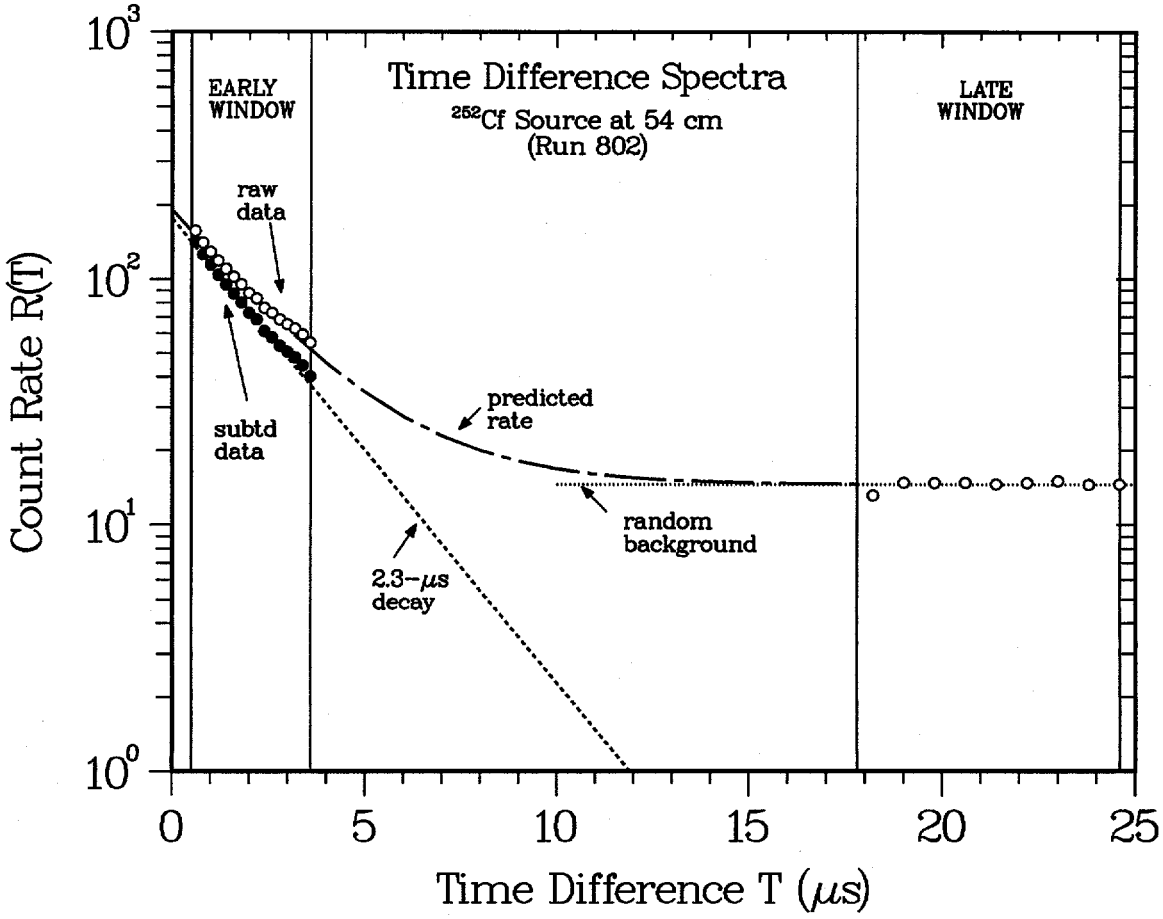

Figure 1-6. Time-Difference Spectrum of BC454

Figure 1-7 shows a ^{252}Cf spectrum with a Maxwellian fit ($T = 1.42$ MeV).[26] The differences between the fitted curve and experimental data are largely because of the fact that there is a neutron-energy threshold of ~0.5 MeV for light production in the scintillator [27] Advantages of the BC454 detector over other scintillators include 1) the ability to uniquely identify neutrons, 2) better stability and ruggedness (compared to liquid systems), and 3) high detection efficiency per unit weight.

1.5. INITIAL CALCULATIONS

Preliminary calculations were done using the Los Alamos transport code MCNP[28] to verify the potentially high neutron-capture efficiency and short die-away time properties of BC454. A figure-of-merit (FOM) algorithm was then used, and assay variance estimates were made for a current state-of-the-art thermal-neutron coincidence counter (TNCC).[29] These estimates were compared to those for an equivalent-efficiency fast-neutron coincidence counter (FNCC), composed of BC454, for plutonium samples with variable (alpha,n) and mass values.

1.5.a. MONTE CARLO SIMULATION

The computer simulation consisted of a right-circular cylinder of BC454 containing 5% boron by weight. The cylinder radius equaled one half its height and varied from 5 to 500 cm. A small sample cavity having a radius of 2 cm and a height of 4 cm was located at the center of the detector. A ^{252}Cf point source, isotropic in angular distribution, was located at the center of the sample cavity. This arrangement simulates

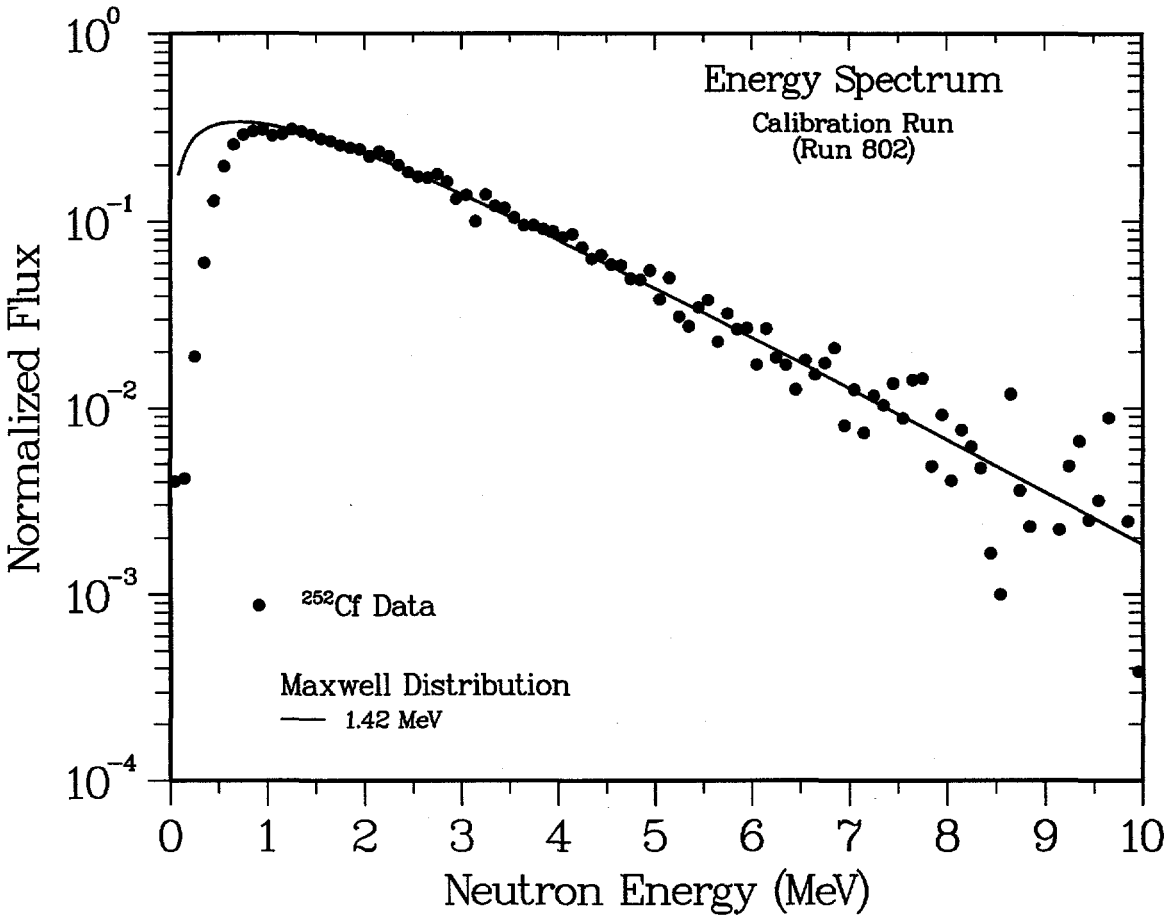

Figure 1-7. Energy Spectrum of ^{252}Cf Measured with BC454

the nearly 4π geometry of most thermal-neutron multiplicity counting systems. Results of these calculations are presented in Table 1-4.

Table 1-4. Calculational Results for Cylindrical Large-Volume BC454 Detector

Cylinder dimensions (cm)	Capture probability (ε)	Die-away time (μs)
r = 5 , h = 10	0.055	1.79
r = 10 , h = 20	0.413	2.02
r = 50 , h = 100	0.989	2.13
r = 500 , h = 1000	0.992	2.13

Die-away times given in Table 1-4 differ somewhat from those reported by Feldman et al. (2.2 μs calculated with Eq. 1-16, 2.4 μs measured),[30] by Kamykowski (1.65 μs calculated with MCNP, 1.69 μs measured),[31] and by Byrd and Urban (1.68 μs calculated with MCNP).[32] The differences arise from the actual geometries used for the various measurements and calculations. Byrd and Urban and Kamykowski worked with single detector elements (7.6-cm diameter and 20-cm length), whereas the data reported by Feldman et al. involved a 4-element array of similar detectors (lower average density compared to single element). It is probable that the longer times reported by Feldman et al. include neutron diffusion time between elements. In all cases, the source is external to the detectors. Fast neutrons are not completely thermalized for these small-volume detector geometries, therefore the die-away times (measured or calculated) do not include the full contribution from lower-energy captures (where the cross section is largest). The trend of times given in Table 1-4 is consistent with this model, starting out at less than 2 μs for the smaller detector and increasing to the theoretical value (large-detector limit)

given by substitution of the following values into Eq. 1-16: $n_{10} = 5.59X10^{20}$ atom/cm^3, $\sigma =$ 3838 b, and $\upsilon = 0.22$ cm/μs, ($\tau = 2.12$ μs).

Efficiency values listed in Table 1-4 increase rapidly and support the possibility of producing a detection system using BC454 that has a neutron capture efficiency equal to or greater than existing TNCCs with a die-away time more than an order of magnitude shorter.

1.5.b. ESTIMATION OF ASSAY VARIANCE

Interpretation of the MCNP results and comparison with a TNCC is facilitated by calculations of the expected assay variance.[33] To quantify the expected reduction in count time, an FNCC with 50% efficiency and 3-μs die-away time was compared with a TNCC also having 50% efficiency but a 50-μs die-away time. Input to the assay variance code includes efficiency, die-away time, predelay, coincidence gate length, dead time, count time, and sample neutron rates. A commonly used gate length of 32 μs and a pre-delay time of 3 μs were chosen for the TNCC, while values of 4 μs and 1 μs, respectively, were used for the FNCC. Dead time was assumed to be 25 ns for the TNCC and 100 ns for the FNCC. Table 1-5 presents the performance comparison of these two detection systems for some high (alpha,n) plutonium samples by showing the count time required to achieve 1% precision on the assay.[34]

The data presented in Table 1-5 assume that the neutron events are completely separated. This assumption is quite good for the TNCC with ^{3}He proportional counters, but it is not as good for the BC454 scintillator because the 93-keV$_{ee}$ peak resides on a

background of gamma-ray and proton-recoil events. The ratio of neutron to gamma-ray background will then depend on the overall gamma-ray emission from the sample and the specific shielding for a given sample/detector configuration.

Table 1-5. Count Time Required for 1% Assay Precision: TNCC vs. FNCC

	10 g Pu		50 g Pu		100 g Pu	
α[a]	TNCC[b]	FNCC[c]	TNCC	FNCC	TNCC	FNCC
3	5 min.	90 s	6 min.	28 s	8 min.	18 s
5	13 min.	2 min.	19 min.	54 s	31 min.	40 s
10	56 min.	5 min.	2.3 hr	3 min.	3.7 hr	3 min.
30	19 hr	30 min.	3 d	34 min.	5.3 d	46 min.
50	4 d	1.3 hr	14 d	2.2 hr	27 d	3.1 hr

[a](alpha,n)-to-spontaneous fission ratio.
[b]Efficiency 50%, die-away time 50 μs, coincidence gate 32 μs.
[c]Efficiency 50%, die-away time 3 μs, coincidence gate 4 μs.

One method to improve the neutron isolation property of the BC454 is to combine it with bismuth germanate (BGO), an inorganic scintillator detector capable of sensing the 478-keV gamma ray arising from the neutron capture reaction. A prompt coincidence between the two detector elements would then unambiguously identify a neutron captured in the BC454.

1.6. ORGANIZATION OF DISSERTATION

Chapter 2 contains a description of the BC454/BGO phoswich detector. General characteristics of the detector are presented along with details of the physical processes

involved with gamma-ray and neutron interactions resulting in specific detection properties. Spectra of the combined signal resulting from exposure to gamma rays and neutrons are presented and described.

In Chapter 3, custom electronics are used to separate the BC454 and BGO principal components and to time-tag each event. Neutron interactions can thereby be identified, along with their time, and used for quantitative measurement of neutron emitting materials.

Chapter 4 contains analyses that have been developed and simulations that were performed, including a pulse-separation model, simulation of detector response to both gamma rays and neutrons, neutron-discrimination techniques, and time-correlation analysis.

Analyses developed in Chapter 4 are applied to the data acquired from the experiments described in Chapter 3 and presented in Chapter 5. The use of the BC454/BGO phoswich detector array for the measurement of neutron-emitting materials is demonstrated through proof-of-principle experiment, and simulations are used to estimate the performance of other detector designs.

Conclusions and suggestions for further work are presented in Chapter 6.

2. DETECTOR CHARACTERISTICS

2.1. INTRODUCTION

The BC454/BGO phoswich detectors used in this work were originally constructed as part of a neutron imaging system for application in space, the Advanced Neutron Detection and Analysis System (ANDAS),[35] where their purpose was to provide information about both the energy and the direction of fast neutrons at energies above about 0.5 MeV. Source imaging was to be obtained by recording which detector had fired and correlating with other detectors in the array; neutron spectra were to be collected as described previously in Chapter 1, using the BGO to enhance identification of neutron events. The mission was canceled prior to any real testing of the ANDAS hardware, and as a result a number of the phoswich detectors were fabricated but never used. The only published work involving these detectors was by Byrd and Russo,[36] who used the combined detector output without separation and collected singles counts in experiments designed to evaluate their use in the location of radioactive sources.

2.2. GENERAL PROPERTIES

A photograph of a detector is shown in Fig. 2-1, showing the inner BC454 core surrounded by BGO, glass light guide (top), and light-reflecting tape.[37] Figure 2-2 is a

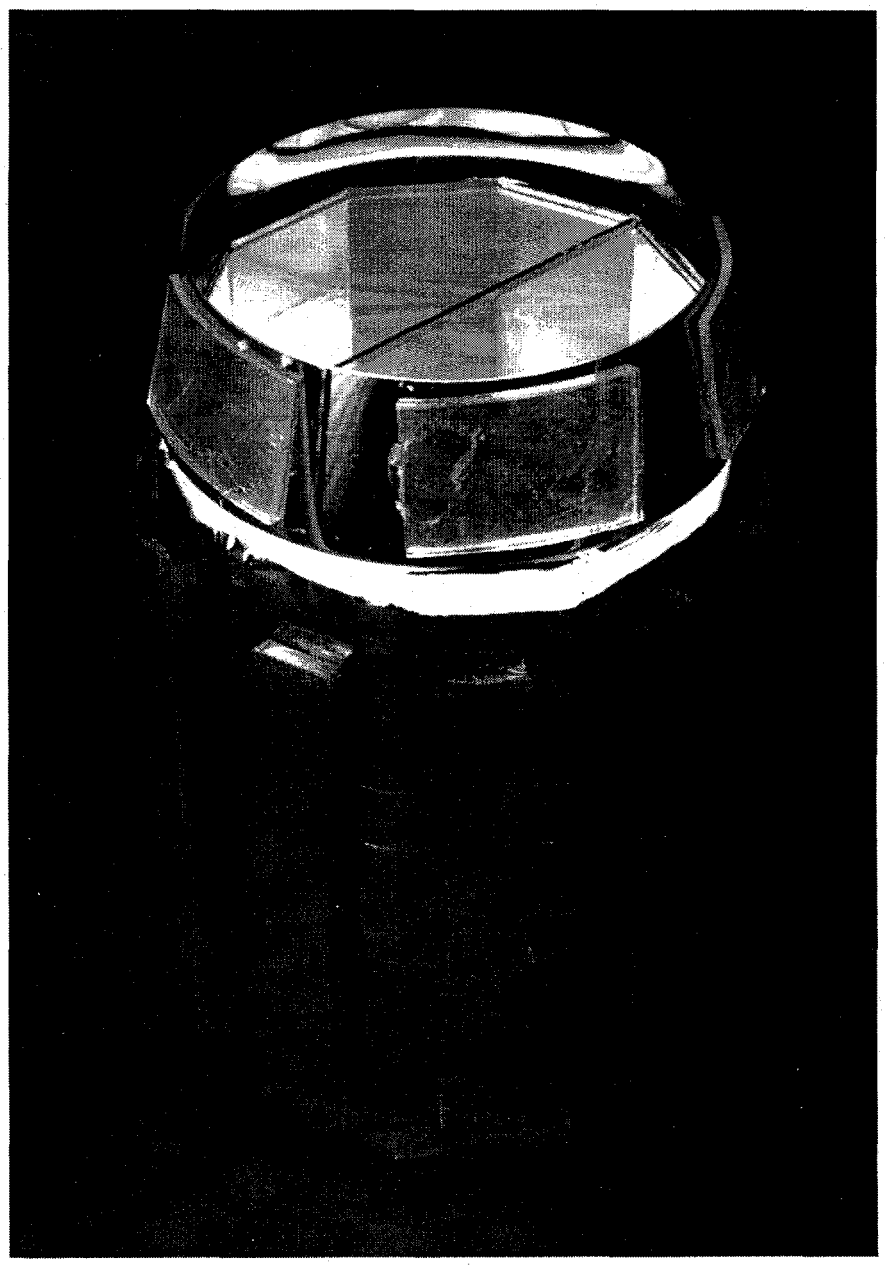

Figure 2-1. Photograph of Phoswich Detector

Figure 2-2. Photograph of Phoswich Detector and Housing

photograph showing the detector housing, photomultiplier tube, and high-voltage bleeder/preamplifier electronics.[38] Each detector consists of a right decagonal cylinder of boron-loaded plastic scintillator (BC454) with a diameter of 7.2 cm and a height of 10.0 cm. This scintillator has essentially the same density (ρ = 1.026 g/cm^3) and hydrogen-to-carbon ratio (H/C = 1.17) as conventional BC408 scintillator, but nominally 5% by weight of natural boron has been added to provide sensitivity to neutrons at very low energies.[39]

The added boron effectively displaces some of the carbon, resulting in a chemical composition by weight that is 87% C, 8% H, and 5% B. Given the 20% isotopic abundance of ^{10}B, the net result is a scintillator that is roughly 1% ^{10}B by weight. This inner BC454 core is surrounded on all sides, including the top and bottom, with 4-mm thick segments of bismuth germanate ($Bi_4Ge_3O_{12}$, commonly known as BGO) scintillator. The combined detector assembly is coupled at one end to a glass light guide and then to a single photomultiplier tube, an arrangement often referred to as a phoswich. Figures 2-3 and 2-4 show the detector construction and dimensions in cross sectional and plan views, respectively.[40] As can be seen from Fig. 2-2, the end of the photomultiplier tube is exposed; therefore, use of the detector in this configuration requires a light-tight enclosure. Two types of enclosures were used in experiments with these detectors: a light-tight box that can accommodate a single detector, and the original ANDAS flight hardware for measurements involving more than one detector.

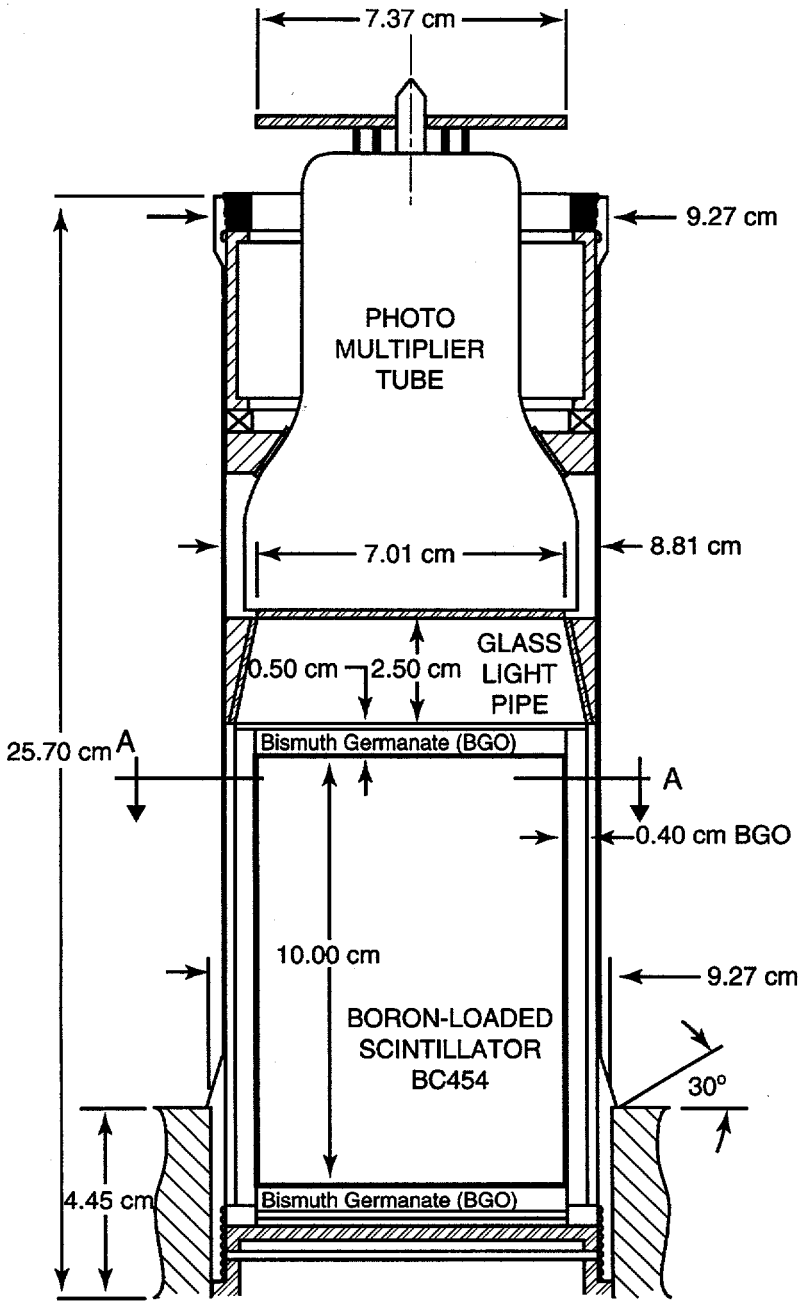

Figure 2-3. Cross Sectional View of Detector and Housing

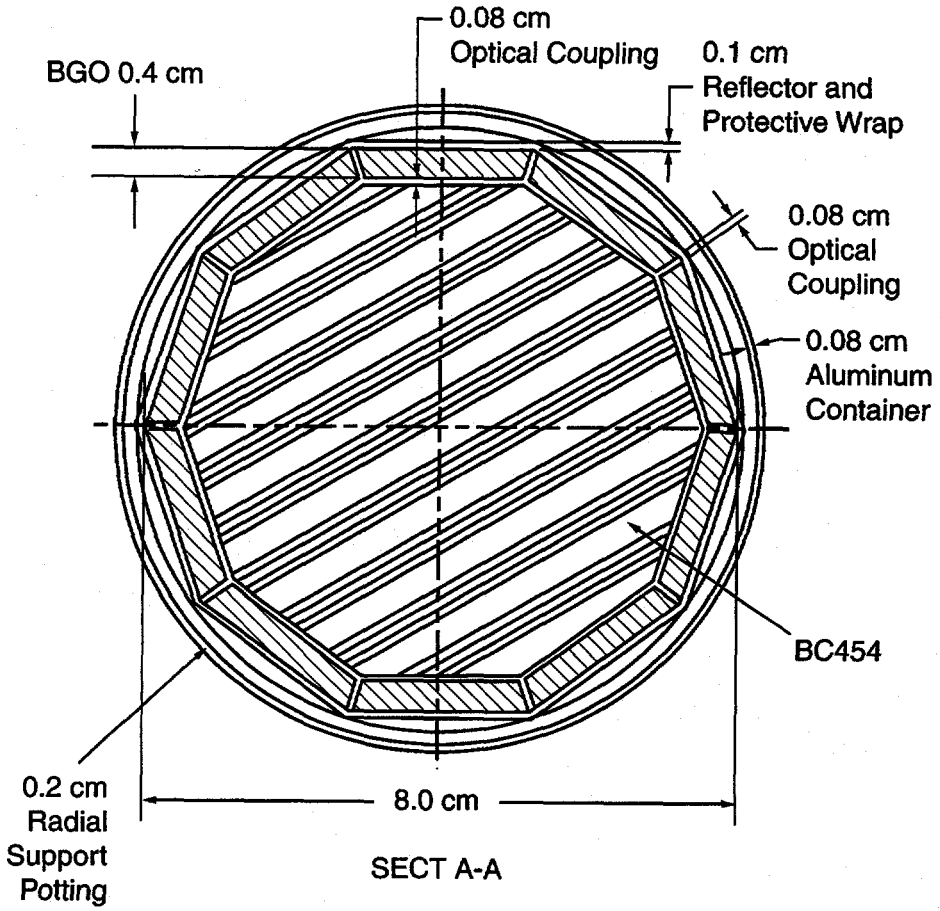

ANDAS
Scintillator/PMT Packaging Concept

Figure 2-4. Plan View of Detector and Housing

Throughout this manuscript the following terminology will be used: a detector will refer to a single BC454/BGO phoswich, a detector element will refer to the BC454 or BGO component of the phoswich, a detector array will refer to multiple detectors operating together, and a detection system will refer to one or more detectors and the associated hardware (processing electronics, power supplies, computer, etc.) needed to collect and store the data that is acquired.

2.3. INTERACTION PHYSICS

The addition of BGO to the BC454 results in a medium-resolution (~20% full-width-at-half-maximum (FWHM) at 662 keV) gamma-ray detector capability being added. Gamma-ray interactions in the outer BGO layer are primarily photoelectric absorption and Compton scattering. For example, a 0.5-MeV gamma ray incident normal to the detector surface has an absorption probability of about 16%, whereupon it deposits essentially all its energy in the BGO. At the higher energy of 1 MeV, the absorption probability drops to 4%, and by 2 MeV it has fallen to 1%. Those scattered or unscattered gamma rays that pass through the BGO layer enter the inner BC454 plastic scintillator, for which Compton scattering is the dominant interaction except at the lowest energies (below about 100 keV), where photoelectric absorption increases rapidly. The phoswich detector response to gamma rays then corresponds to a combination of a medium-resolution spectrum containing photopeaks superimposed on a Compton continuum resulting from interaction with BGO plus a Compton spectrum arising from interactions in the BC454. The overall light production per unit energy deposited is greater for BC454 than BGO by a factor of about 2.5, resulting in spectral features being

located at different relative places for each detector element. For example, the Compton edge from a ^{137}Cs source (477 keV) produces more light in BC454 than the unscattered gamma ray (662 keV) in BGO, giving rise to a Compton edge at a higher location in the combined spectrum than the corresponding photopeak.

The plastic scintillator serves as the primary detector for incident neutrons at fission energies. Few incident neutrons at fission energies interact with the outer layer of BGO; those that do are simply scattered with little energy loss. Because the plastic scintillator is composed almost equally of hydrogen and carbon, at most energies almost all interactions are simply elastic scattering from one of these two materials. Because scattering from carbon causes little energy loss, it is n-p scattering on hydrogen that is responsible for most of the important neutron interactions. Only neutrons with incident energies above ~0.5 MeV produce sufficient ionization to give a detectable light output. After one or two scattering events, most of the incident neutrons escape from the detector. About 10%, however, become trapped in the detector by the rapidly increasing scattering probability at lower energies. In conventional scintillators, the only remaining mechanism for light output from neutron interactions is proton radiative capture, which produces a 2.3-MeV gamma ray, but this capture occurs only with low probability. In our case, however, the 5% added boron (1% ^{10}B by weight) introduces an additional and much more probable interaction mechanism. Capture by ^{10}B produces alpha and ^{7}Li charged particles, whose energy (93 keV_{ee}) is immediately deposited at the capture site. In addition, about 94% of the time the reaction proceeds through the first excited state of ^{7}Li, which subsequently deexcites by the emission of a 478-keV gamma ray. For our scintillator geometry, about 40% of these gamma rays are Compton scattered in the

plastic, and most of these are then absorbed in the outer layer of BGO. Of those 478-keV gamma rays that escape unscattered from the plastic and reach the BGO, approximately 20% deposit their entire energy in the outer BGO layer. Figure 2-5 depicts a typical fast-neutron interaction in the detector. The neutron elastically scatters in the BC454 (producing a proton recoil pulse) and is finally captured by ^{10}B, at which time a 478-keV gamma ray is emitted and detected in the BGO. A coincidence between the two detector elements (93 keV_{ee} in the BC454 and 478 keV in the BGO) identifies a neutron capture event.

2.4. SPECTRA

A series of gamma-ray and neutron spectra were collected in which the detector's combined output (BC454 and BGO) was processed without any separation, to investigate the performance characteristics of the phoswich configuration. Sources measured were: ^{137}Cs, ^{60}Co, ^{54}Mn, ^{22}Na, ^{88}Y, AmB, ^{252}Cf, and PuBe. Detector element resolutions were measured for both gamma rays and neutron-capture events, relative gains were calculated for gamma-ray interactions in BC454 and BGO, the basic neutron capture signature was determined, and the linearity of the detector response was evaluated.

2.4.a. GAMMA-RAY MEASUREMENTS

Spectra were collected in the following configuration: The detector, in a light-tight aluminum housing, was placed horizontally with the source located along side the

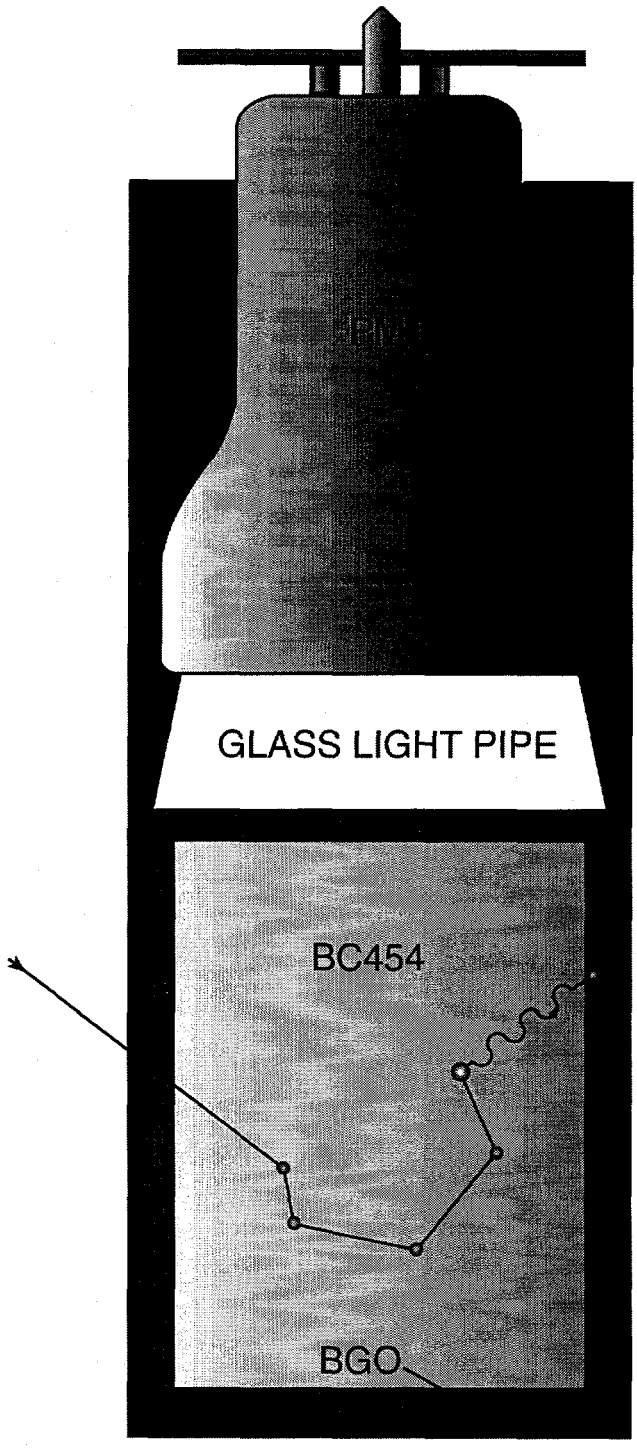

Figure 2-5. Typical Neutron Interaction with Capture Termination

cylinder a few centimeters away in line with the center of the BC454 core. The distance between the source and detector was such that the count rate was 2000 counts/s, and no collimation was used.

Relative gains for the BC454 and BGO were calculated from the gamma-ray spectra by examining the full-energy peak (also referred to as the photopeak) arising from BGO interaction and the corresponding Compton edge due to interaction of the same energy photons in the BC454. Figures 2-6 through 2-10 are spectra from ^{137}Cs, ^{60}Co, ^{54}Mn, ^{22}Na, and ^{88}Y respectively. In each spectrum, the contributions from BGO (photopeaks) and BC454 (Compton edges) are clearly seen.

Table 2-1 gives energies and corresponding channel numbers for each of the sources measured.

Table 2-1. Gamma-ray Energies and Corresponding Channels

	Photopeak (BGO)		Compton Edge (BC454)	
Nuclide	E (keV)	Channel (ch)	E (keV)	Channel (ch)
^{137}Cs	662	222	478	551
^{60}Co	1253[a]	463	1041	1078
^{54}Mn	834	302	638	633
^{22}Na	511	163	341	310
	1275	467	1062	1115
^{88}Y	898	320	699	---[b]
	1836	678	1612	1660

[a]Average of 1173 keV and 1333 keV
[b]Not resolved from 1836 keV

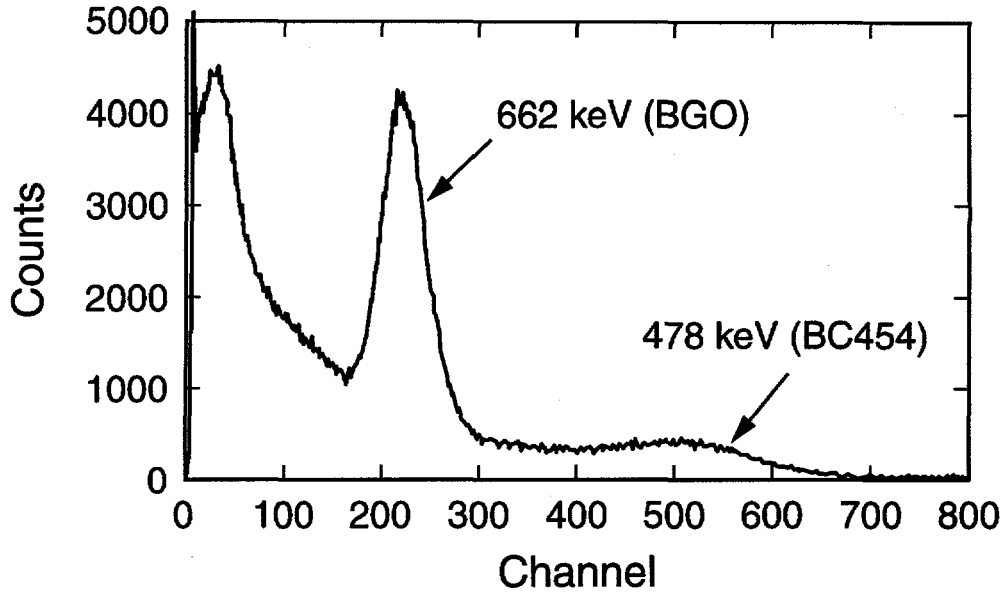

Figure 2-6. Combined ^{137}Cs Spectrum

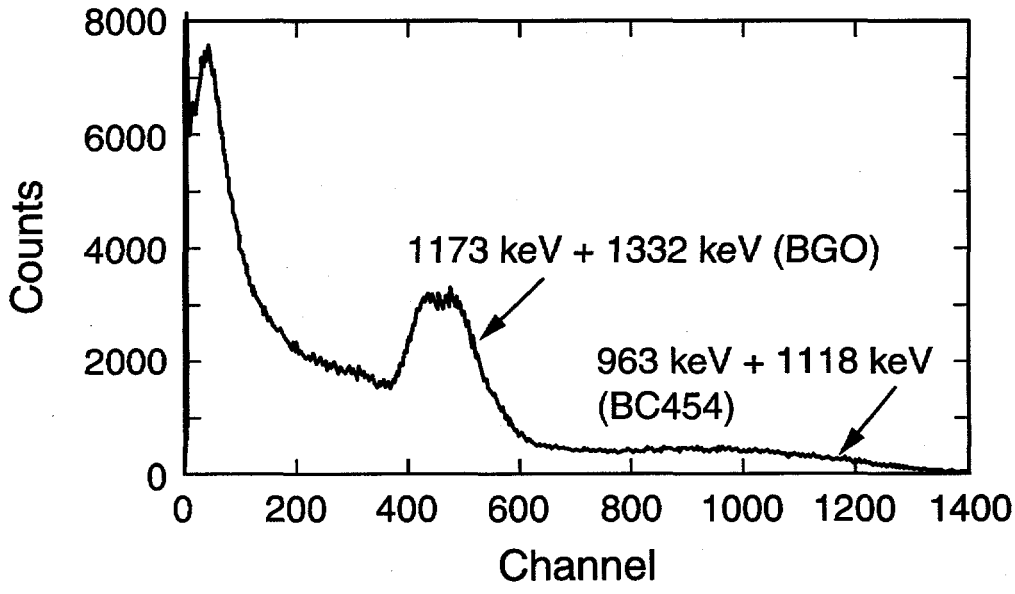

Figure 2-7. Combined ^{60}Co Spectrum

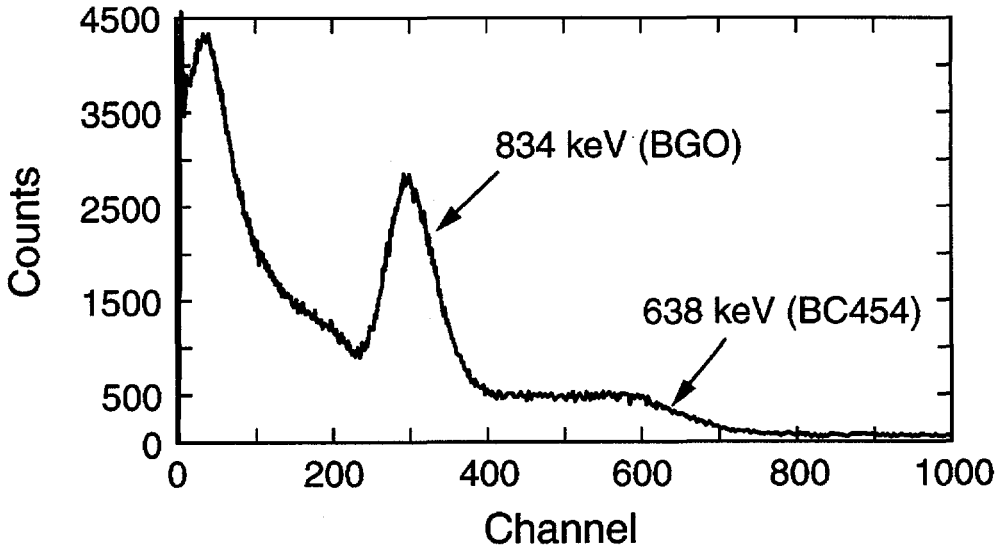

Figure 2-8. Combined ^{54}Mn Spectrum

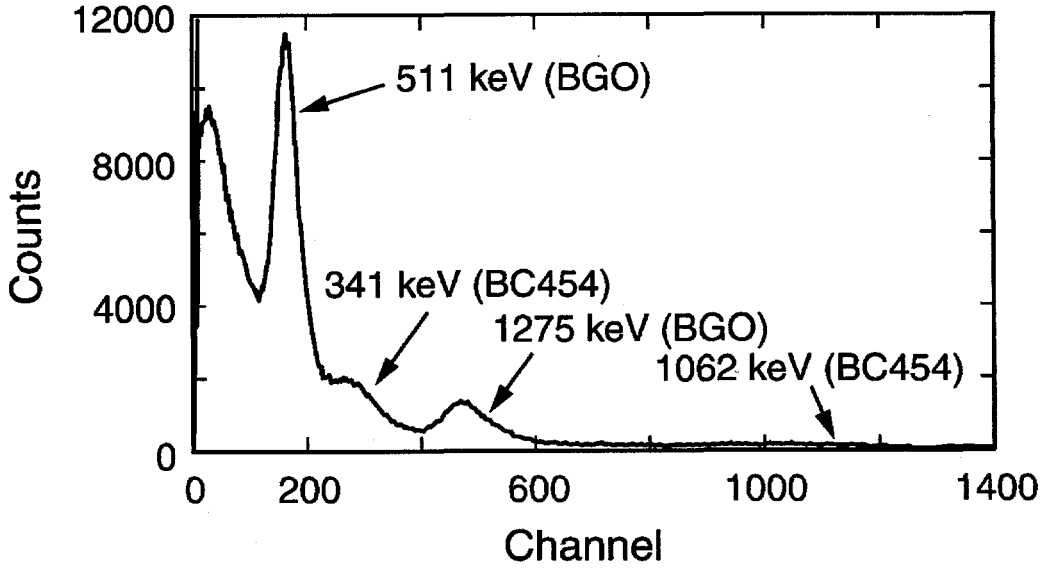

Figure 2-9. Combined ^{22}Na Spectrum

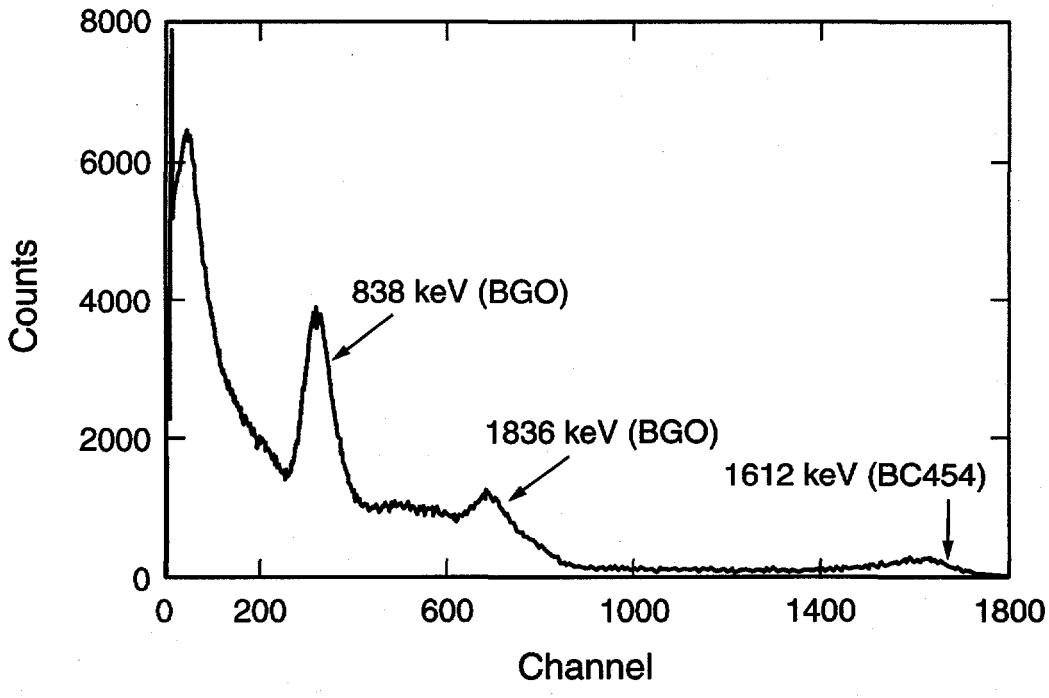

Figure 2-10. Combined ^{88}Y Spectrum

The average value of the two gamma rays from ^{60}Co is used in Table 2-1 because they were not individually resolved, as evidenced by Fig. 2-7. Energy calibrations for gamma rays in the BC454 and BGO are given in Table 2-2 using a linear function ($E = x + y$ch). The correlation coefficient R^2, is also given in Table 2-2 ($R^2 = 1.0$, perfect correlation).

Table 2-2. Gamma-ray Energy Calibration

Detector Element	x (keV)	y (keV/ch)	R^2
BGO	79.0	2.568	0.999
BC454	8.2	0.958	0.995

We see from the energy calibrations given in Table 2-2 that the phoswich detector is relatively linear in response to gamma rays. This result is consistent with the expectation from the linear response of the individual detector elements. Figure 2-11 summarizes the resolution characteristics(full width at half maximum, FWHM) of the BGO element. As shown there, the relative resolution of the BGO element is 30% at 662 keV and follows the expected $1/\sqrt{E}$ behavior (the FWHM is proportional to the square root of the number of photons, which in turn is proportional to E). The measured resolution of 30% is larger than the nominal 15% quoted for single BGO crystals. This degradation is a result of two factors, the first being the relative thinness (0.4 cm) of the BGO in the phoswich detector and the other the differences in light transport to the photomultiplier tube depending on the interaction location.

Figures 2-12 through 2-14 shows the result of collimating a ^{137}Cs source placed along side the cylindrical detector and moving the source and collimator parallel to the

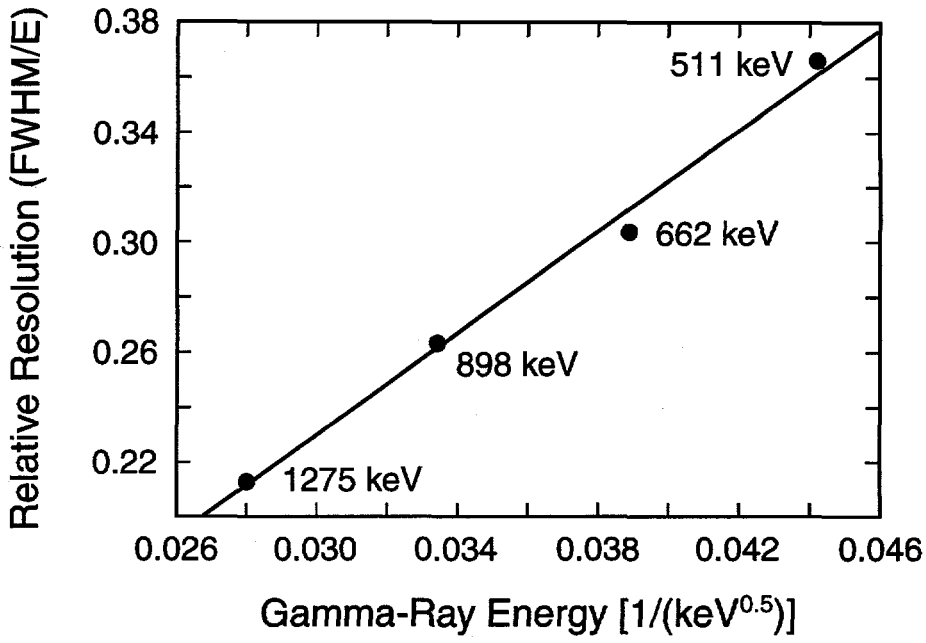

Figure 2-11. Resolution Characteristics of the BGO Element

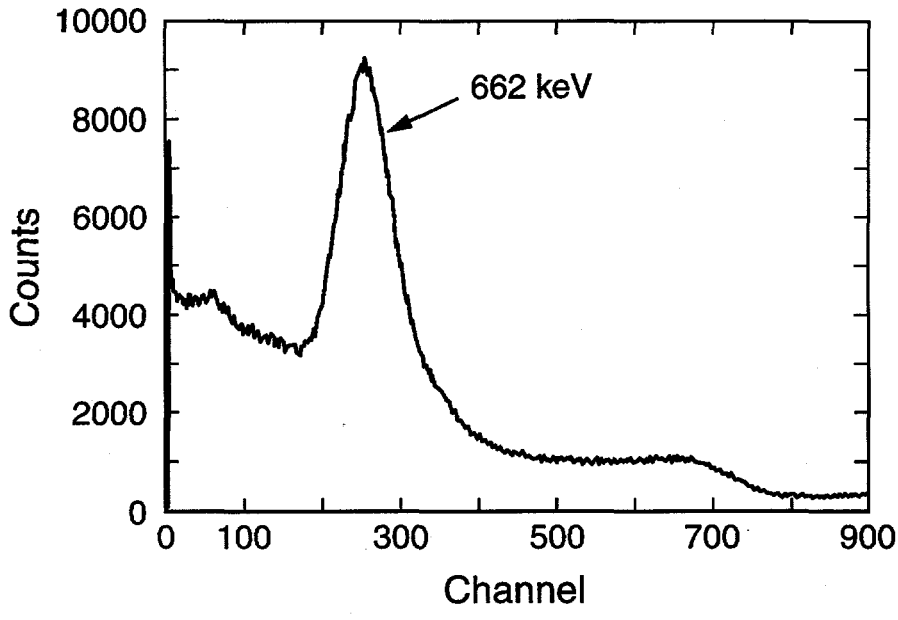

Figure 2-12. Effect of Interaction Location on Resolution, ^{137}Cs Source at Bottom

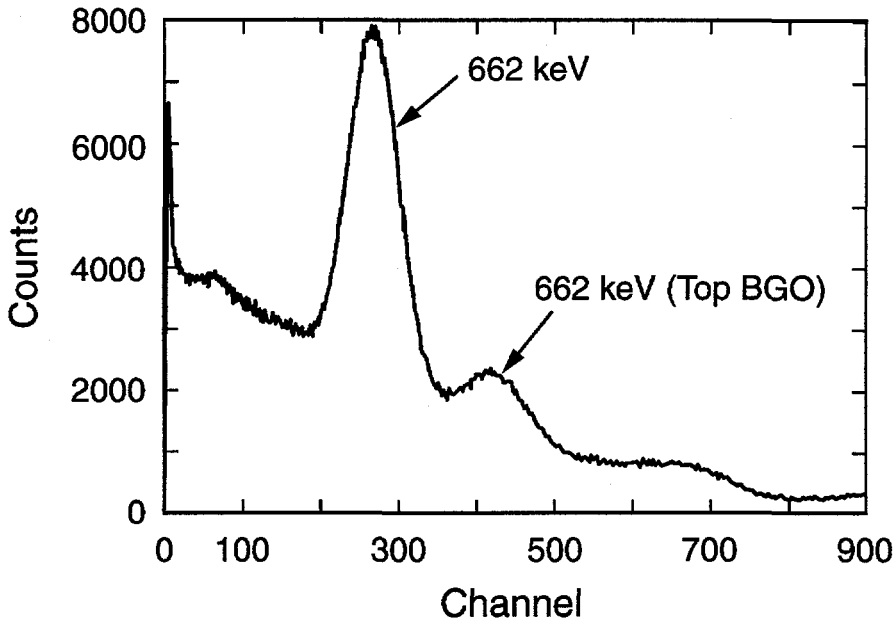

Figure 2-13. Effect of Interaction Location on Resolution, ^{137}Cs Source in Middle

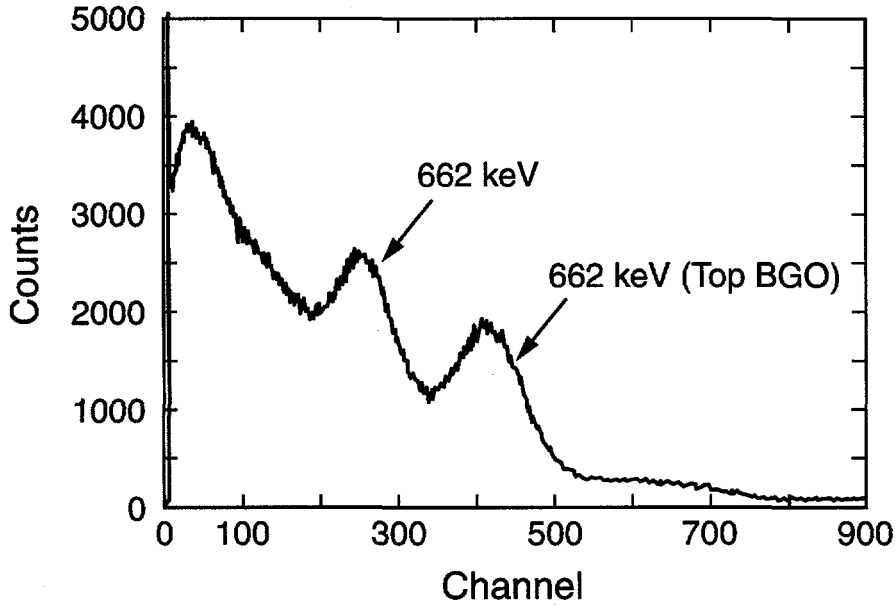

Figure 2-14. Effect of Interaction Location on Resolution, ^{137}Cs Source at Top

vertical axis of the detector. As the source moves to the top (where the photomultiplier couples to the detector), the photopeak shifts to a higher location in the spectrum. This shift occurs because the top piece of BGO has a greater optical coupling to the photomultiplier tube than do the others. As a result, the overall resolution of the BGO is worse than would be expected for a single piece alone.

2.4.b. NEUTRON MEASUREMENTS

Neutron spectra shown in Figs. 2-15 through 2-23 were acquired for AmB, ^{252}Cf , and PuBe for the purpose of determining the neutron capture signature of the phoswich as well as the resolution of the capture peak in the BC454. The geometry of the measurements for the AmB and ^{252}Cf data was similar to that for the gamma-ray spectra except that polyethylene and boron-loaded polyethylene were alternately placed between the source and detector and separate counts obtained for each (see Figs. 2-15 and 2-16, 2-18 and 2-19). Subtraction of the two spectra gives the neutron capture signature of the phoswich detector (see Figs. 2-17 and 2-20). A similar procedure was carried out for the PuBe measurements, except that in this case the source was in the center of a large graphite pile and data was taken with and without the cadmium cover over the thermal port (see Figs. 2-21 and 2-22). Figure 2-23 shows the result of subtracting these spectra. Notice the similarity in the spectral features contained in Figs. 2-17 , 2-20, and 2-23.

Comparison of the subtracted spectra obtained for the phoswich detector and the neutron capture spectrum from pure BC454 (see Fig. 1-5) reveals the expected result: the phoswich detector's neutron capture signature is a combination of 1) the 93-keV$_{ee}$ peak

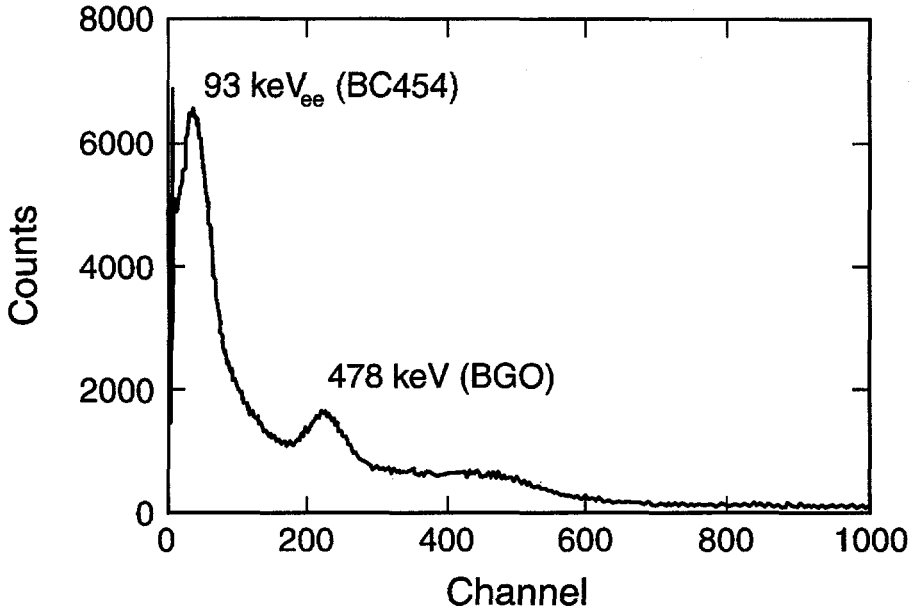

Figure 2-15. Combined AmB Spectrum with Polyethylene

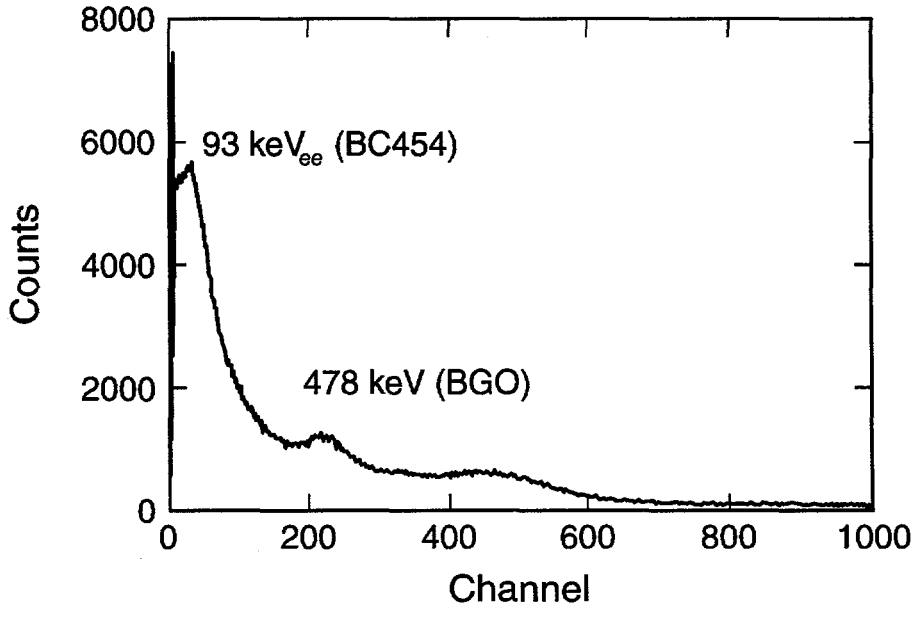

Figure 2-16. Combined AmB Spectrum with Boron-Loaded Polyethylene

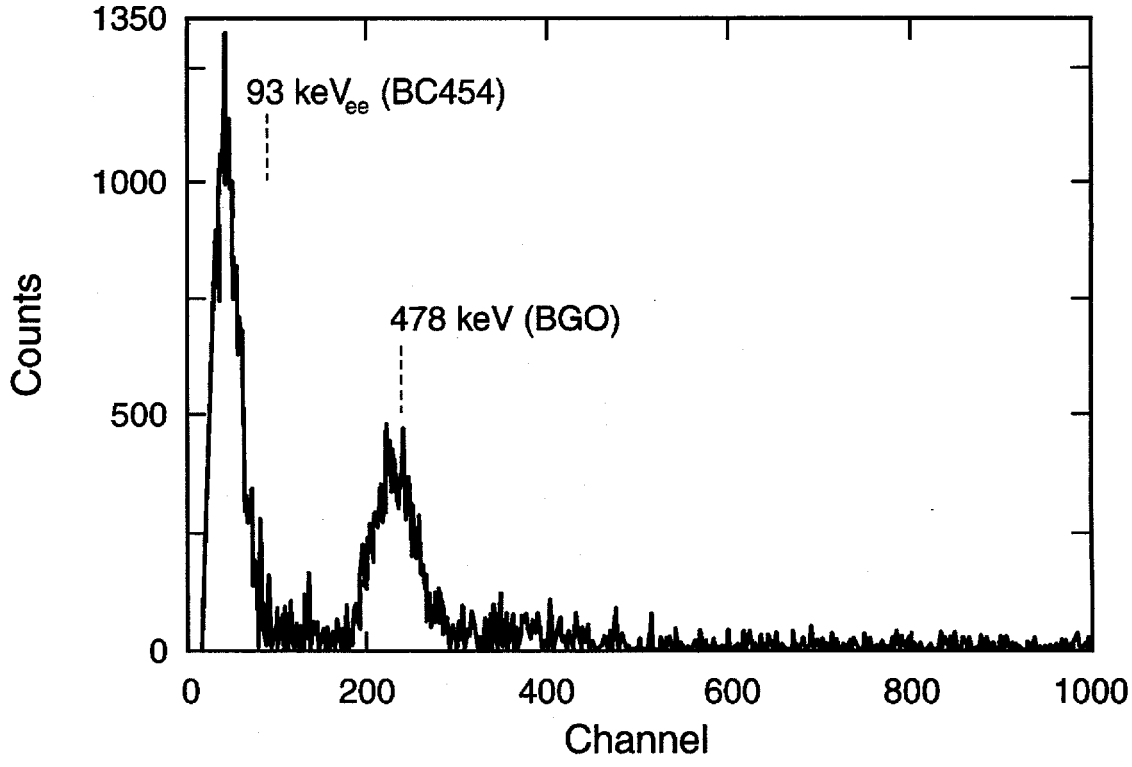

Figure 2-17. Combined AmB Difference Spectrum

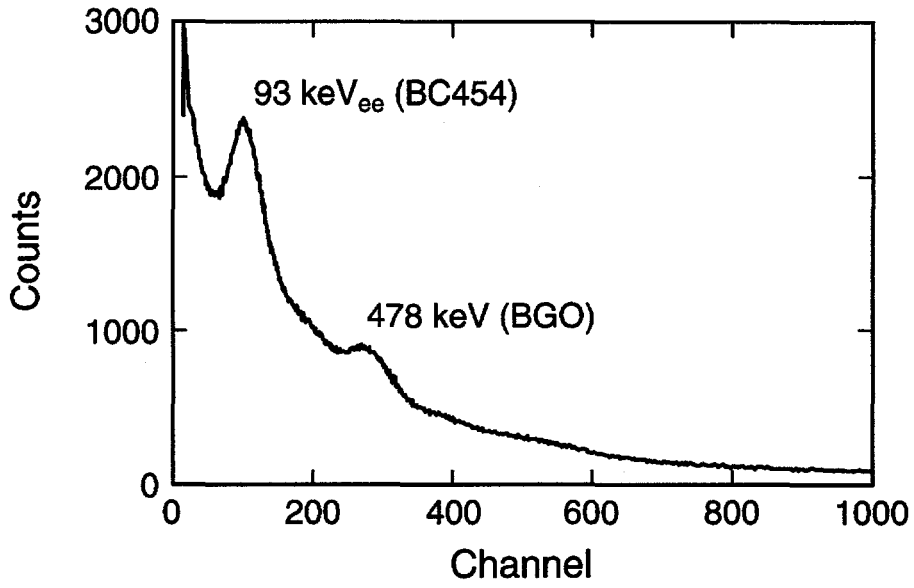

Figure 2-18. Combined ^{252}Cf Spectrum with Polyethylene

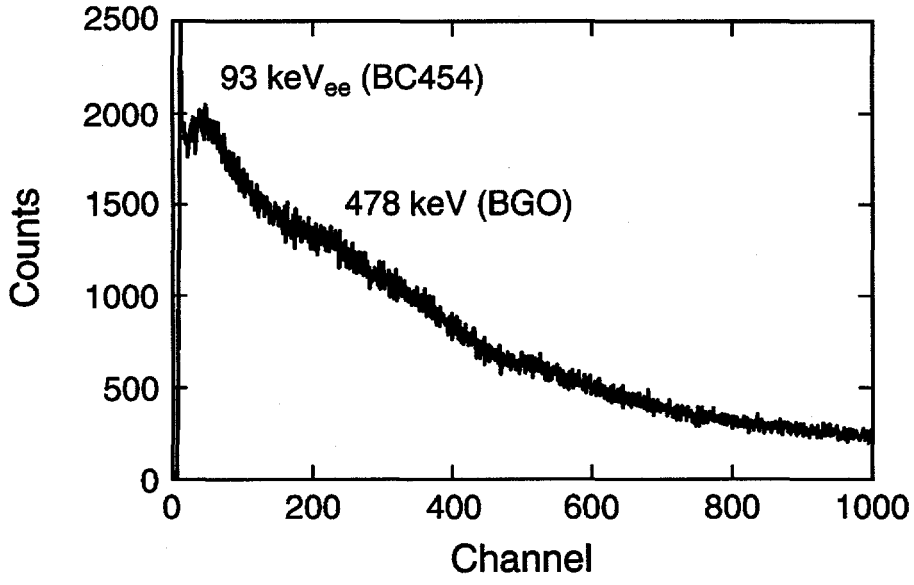

Figure 2-19. Combined ^{252}Cf Spectrum with Boron-Loaded Polyethylene

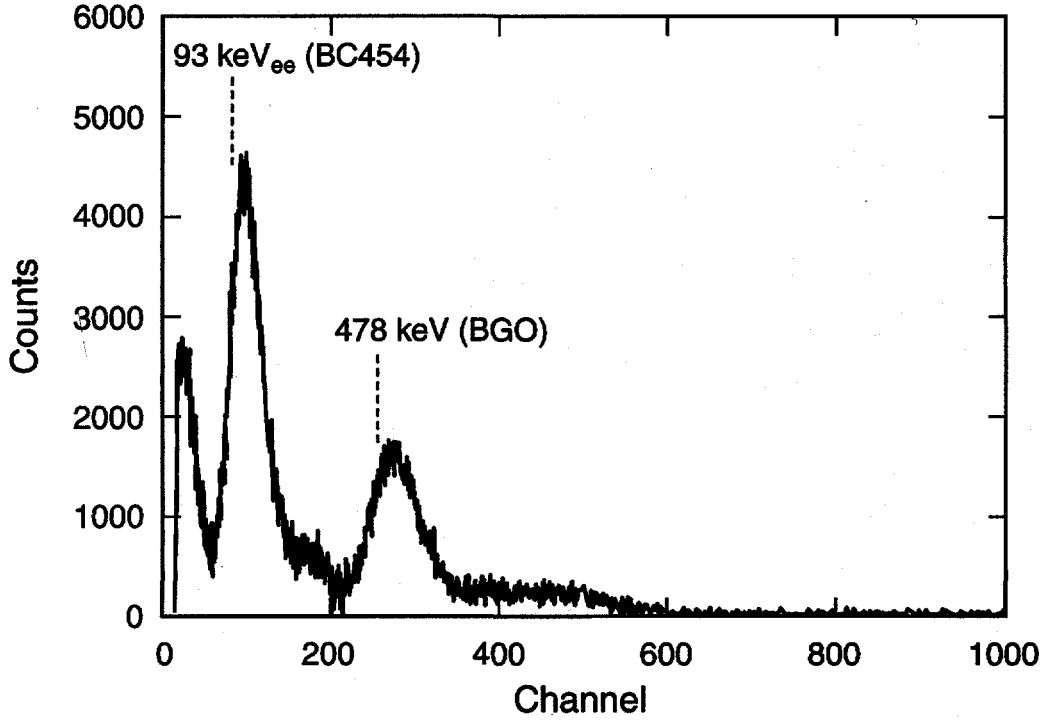

Figure 2-20. Combined ^{252}Cf Difference Spectrum

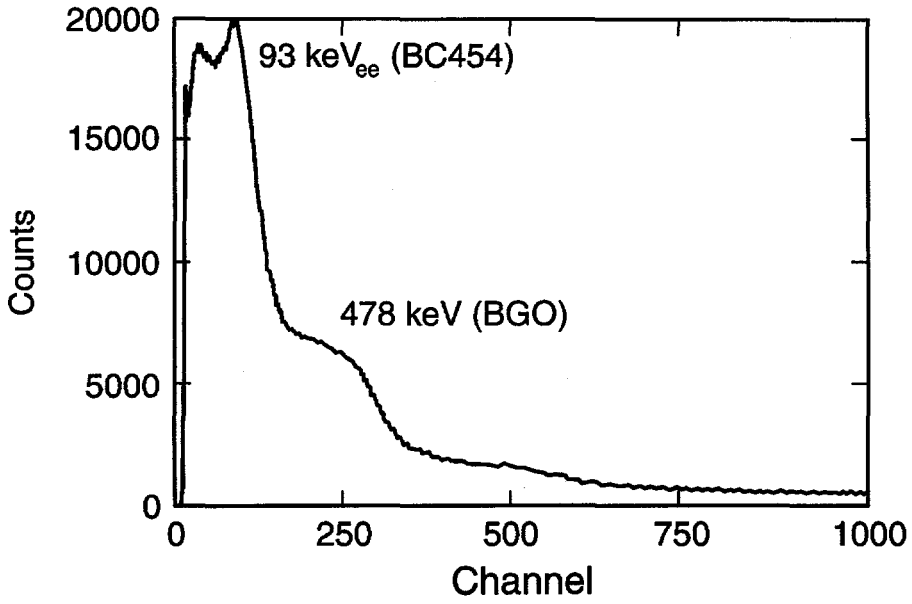

Figure 2-21. Combined PuBe Spectrum without Cadmium

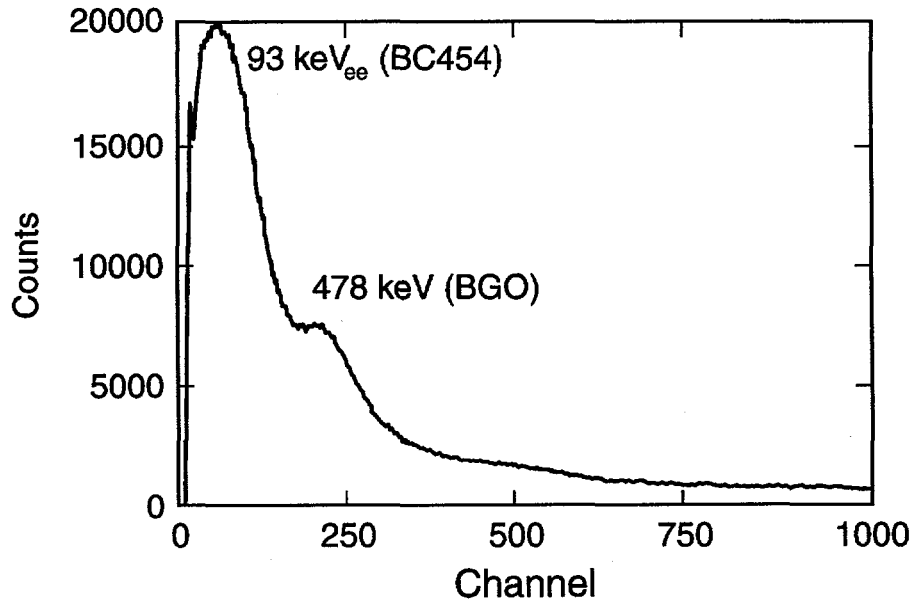

Figure 2-22. Combined PuBe Spectrum with Cadmium

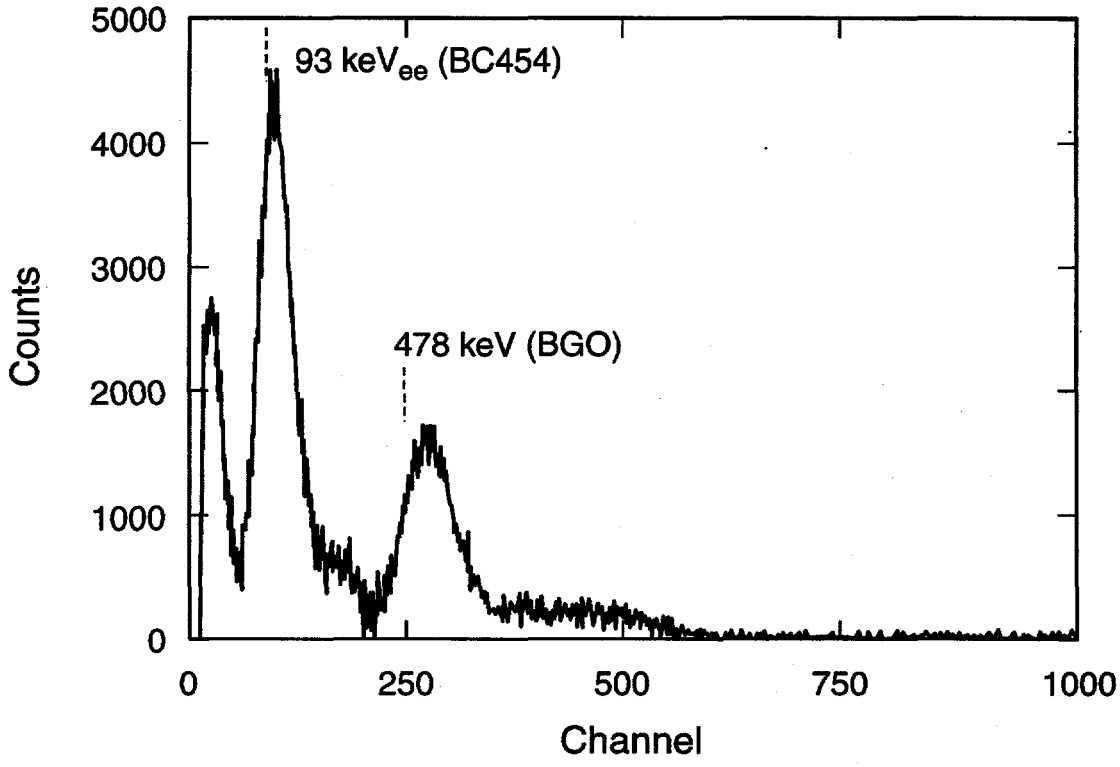

Figure 2-23. Combined PuBe Difference Spectrum

and Compton scatter of the 478-keV gamma ray in the BC454 with 2) the 478-keV gamma-ray spectrum (photopeak and Compton scattering) in the BGO. The predictions of the location in the spectrum of the 93-keV$_{ee}$ capture peak and 478-keV photopeak based on the energy calibration given in Table 2-2 are shown as dashed lines in difference-spectra of Figs. 2-17, 2-20, and 2-23. Displacement from the predicted values indicates a change in the DC offset for a combined BC454/BGO pulse relative to either BC454 or BGO alone, which is the case for the photopeak and Compton edge feature in the spectra.

In this chapter the detection physics and characteristics of the combined phoswich response to both gamma rays and neutrons has been described and measured. The gamma-ray response is observed to be linear for both detector elements, with an overall BC454-to-BGO gain ratio of about 2.5. Resolution of the BGO component of the detector response was observed to be worse than that typically reported for single BGO crystals; however, the resolution was sufficient to clearly identify the 478-keV neutron-capture gamma ray. Neutron spectra were collected in a manner that allowed the capture spectrum to be recorded. This spectrum has contributions from both detector elements: 1) a 93-keV$_{ee}$ peak in the BC454 resulting from the energy deposited by the ^{10}B(n,alpha) reaction products ^{7}Li and ^{4}He, 2) a Compton spectrum in the BC454 arising from the interaction of the 478-keV$_{ee}$ neutron-capture gamma ray as it exits the detector, 3) a 478-keV photopeak in the BGO which results from the full-energy detection of the capture gamma ray, and finally 4) the corresponding Compton-scatter spectrum in the BGO resulting from partial energy deposition of the 478-keV capture gamma ray (transmitted or scattered in the BC454). Individual pulses (BC454 or BGO only) appear to have a

different DC offset than do combined BC454/BGO pulses, as evidenced by the displacement of the 478-keV peak arising from neutron capture. This effect is consistent with the problem of trying to shape two distinctly differently pulses with a single amplifier/baseline circuit (required for combined pulse spectrometry).

The next chapter, Data Acquisition and Measurements, describes the data-acquisition system and custom electronics used to separate the combined BC454/BGO pulse for quantitative determination of neutron-emitting materials.

3. DATA ACQUISITION AND MEASUREMENTS

3.1. INTRODUCTION

Experiments were conducted to evaluate the capability of the BC454/BGO phoswich detector for quantitative measurements by isolating the neutron response and performing time-correlation analysis. Custom electronics were used to separate the combined analog signal of the detector into its principal BC454 and BGO components. Separation of the signal is relatively easy in this case because of the large difference in pulse shapes for BC454 and BGO (decay times of 3 and 300 ns, respectively). Measurements were conducted with a single detector and a close-geometry array. Gamma-ray and neutron sources were measured in both the energy and time domains. Application to the quantitative measurement of plutonium was explored.

The short die-away time (~2 μs) and potential for high neutron-detection efficiency of BC454 (>90% capture for a large-volume detector) make it an attractive material for multiplicity counting applications. The primary drawback of BC454 for neutron counting, and indeed of organic scintillators in general, is their sensitivity to gamma rays. The addition of boron allows a degree of discrimination of neutron capture events from others by isolation of the 93-keV$_{ee}$ peak that results from the charged particles produced in the ^{10}B(n,alpha) reaction. In the case of the phoswich detector, another level of discrimination can be realized by requiring a prompt coincidence

between the BC454 (93-keV$_{ee}$ peak) and the BGO (478-keV gamma ray from decay of the first excited state of ^{7}Li) signals. A data acquisition system has been assembled that will enable analysis of the data in a variety of ways: 1) using only the 93-keV$_{ee}$ (BC454) capture peak for neutron discrimination, 2) requiring a prompt coincidence between the 93-keV$_{ee}$ (BC454) and 478-keV (BGO) peaks, and 3) requiring a proton recoil to precede a capture event by recording the energy and time for each BC454/BGO event.

3.2. DATA ACQUISITION

Phoswich detectors using a new preamplifier with a differential output (two outputs having a 180° phase difference), but otherwise of the same type as shown in Fig. 2-2, were used for the quantitative measurements. Changes in baseline level affect both outputs equally, therefore this type of design affords a greater protection against noise. This preamplifier shares a common heritage with another project, the National Aeronautics and Space Administration Discovery Mission Lunar Prospector. One of the instruments on board this 1997 mission to the moon is the Gamma-ray Spectrometer (GRS), consisting of a large BGO detector surrounded by a BC454 anticoincidence shield.[41] The two detectors are optically isolated in this case, and the primary purpose of the GRS is gamma-ray rather than neutron detection.

Output from the preamplifier feeds into a custom constant-fraction discriminator (CFD), for timing control, and into the gated-integrator (GI) circuit, thereby performing a first-order separation of the phoswich signal. The GI outputs are in turn sent to an analog-to-digital converter (ADC) and subsequently stored in the computer. In parallel with the integration, CFD triggers are sent to a custom time-tag module (TTM) that

provides a time stamp for each event. Analysis is done in software using the time and energy data. Figure 3-1 presents a block diagram of signal routing for the detection system. Figure 3-2 is a diagram of the data-acquisition electronics rack used for the quantitative measurements.

3.2.a. DETECTOR ASSEMBLY

The phoswich detectors housed in an aluminum casings (the original flight hardware for the ANDAS project) were placed symmetrically around a central source location. A cylindrical sample chamber was fabricated that positioned the source in the center of the detector array and provided gamma-ray shielding (0.6-cm thick tungsten) as well as some neutron moderation (3-cm thick polyethylene) and scattering (10-cm thick graphite). Figure 3-3 is a schematic of the detector housing, showing the locations of the detectors and sample chamber. The construction of the sample chamber is presented in Fig. 3-4. An additional piece of graphite, 10 cm thick by 30 cm square, was available to be positioned at one end to further enhance scattering of neutrons back to the detectors.

3.2.b. CONSTANT FRACTION DISCRIMINATOR/GATED INTEGRATOR

As shown in Fig. 3-5, output from the preamplifier is routed to the CFD and GI electronics. The CFD/GI unit is a custom Nuclear Instrument Module (NIM) designed and built for these experiments. As the signal enters the board it is split, with one leg

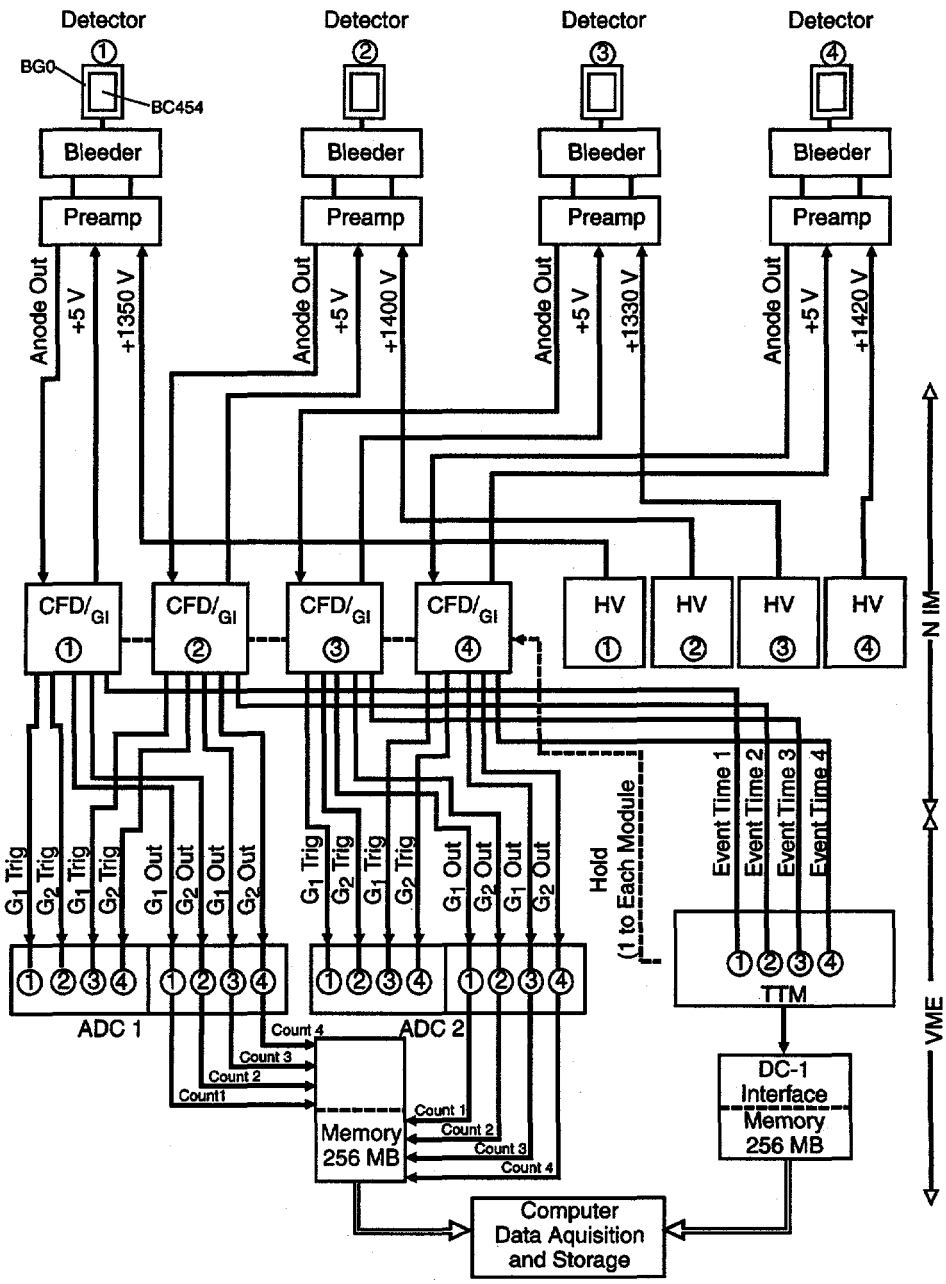

Figure 3-1. Diagram of Signal Routing

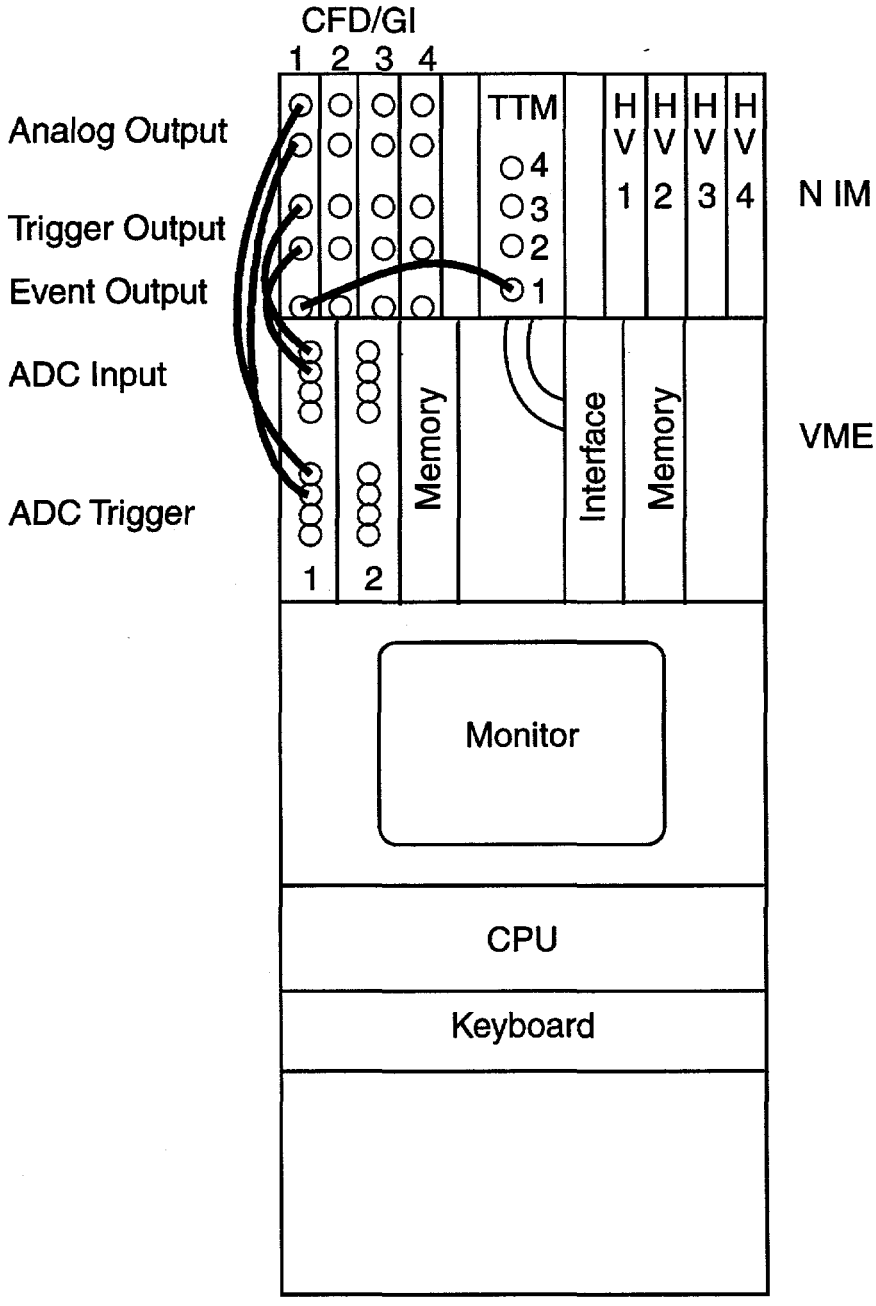

Figure 3-2. Diagram of Data-Acquisition Electronics Rack (Top View)

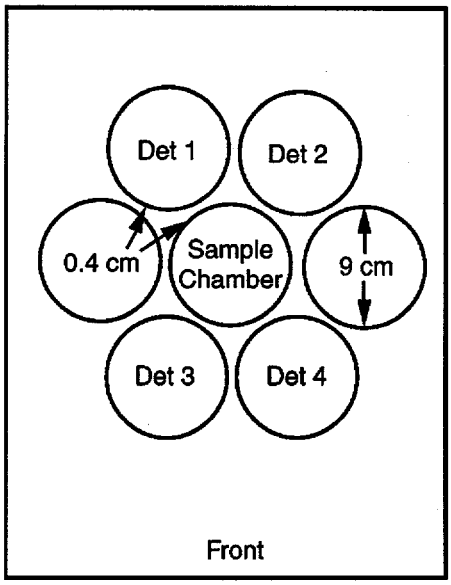

Figure 3-3. Schematic Layout of the Detector Housing (Side View)

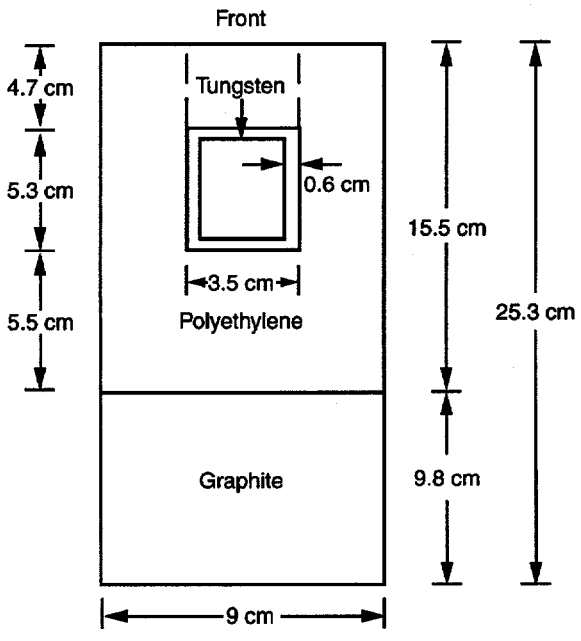

Figure 3-4. Sample Chamber Construction

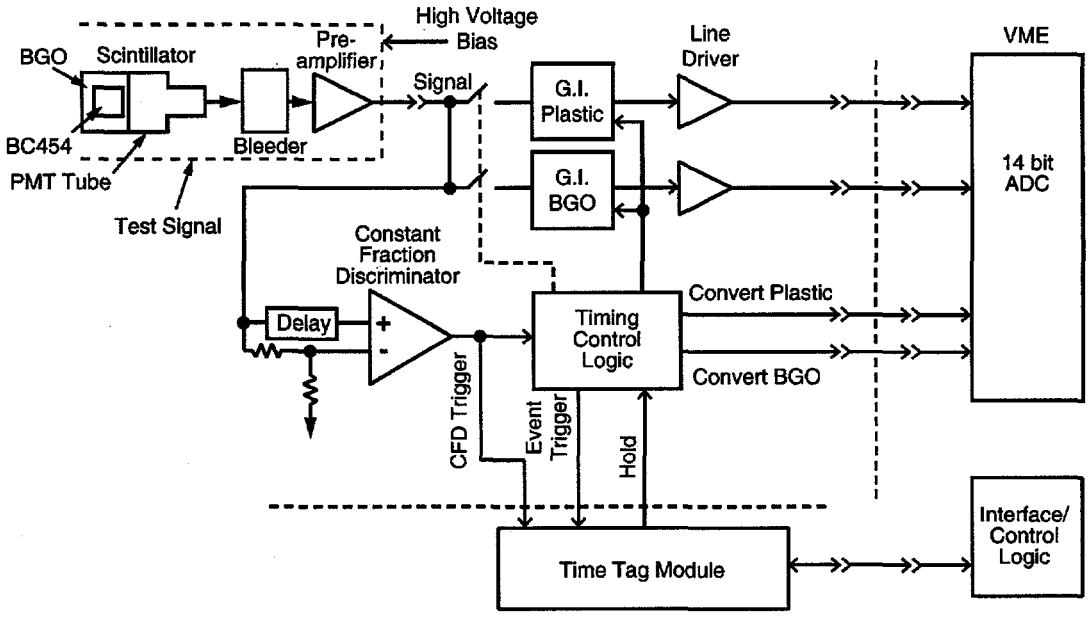

Figure 3-5. Constant Faction Discriminator, Gated Integrator and Time-Tag Module

going to the CFD circuitry and the other going to the GIs. The signal entering the GI is delayed so that the CFD has time to respond prior to arrival at the GI input. Outputs of the CFD control logic are as follows: triggers to initiate the integration of the BC454 and BGO portions of the combined signal, triggers to the TTM, and triggers to the ADC board to initiate digitization of the integrator outputs. The CFD also receives a signal from the TTM that acts to suspend CFD operation to allow transfer of timing data to the computer if the TTM buffer becomes full.

Integration of the signal is done by a pair of GIs, one for the first 80 ns (primary BC454 component) and the other for the subsequent 400 ns (primary BGO component). Triggers from the CFD initiate the integration. The integration over the first 80-ns gate contains almost all of the BC454 and a small portion of the BGO, while the integration in the following 400-ns gate contains a majority of the BGO. Figure 3-6 is a schematic of the analog BC454 and BGO pulses and their relation to the integration gates. Once the GIs have finished, the signal is held for 200 ns to allow sampling by the ADC. After that, the GIs are ready to accept another event. The total cycle time is 800 ns. Each CFD/GI module can accommodate a single phoswich detector. A total of four modules were used for these experiments.

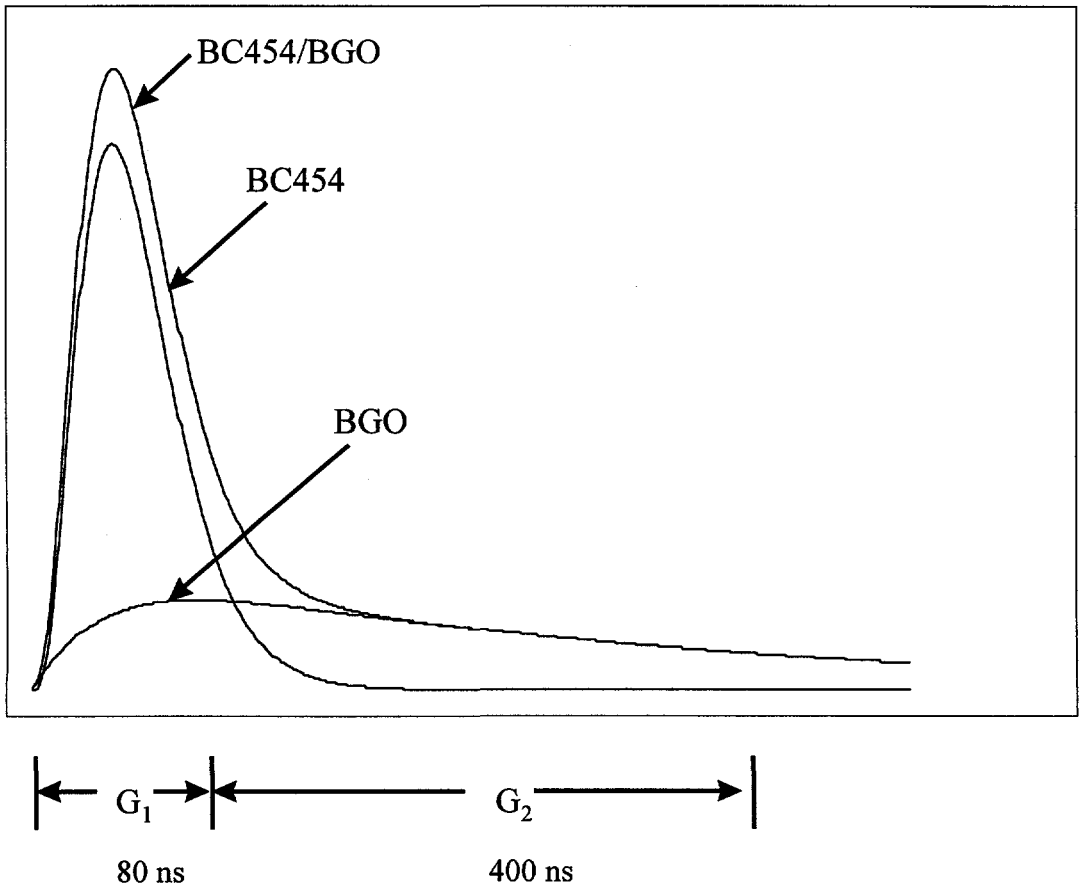

Figure 3-6. Schematic of BC454 and BGO Pulses Showing Integration Gates

3.2.c. ANALOG-TO-DIGITAL CONVERTER

Conversion of the output of the integrators to digital form is done by an Alphi Technology[†] model AD42m ADC board. Each ADC board has 4 inputs, each individually triggerable by the CFD. The model AD42m is a fast, 14-bit flash ADC with total cycle time less than that of the CFD/GI module and with on-board buffer (64 kB) capability. It is housed in a Versa Module Eurocard (VME) crate along with a 256-MB memory module (Chrisslin model 256M)[‡]. The AD42m and memory module reside on a local VME Subsystem Bus (VSB) bus to allow fast transfer of ADC data into memory. Output from the AD42m is a 16-bit word composed of 14 bits of ADC data and 2 bits of channel identifier. These 16-bit words are packed in groups of two into the 32-bit memory. Each AD42m can process data from two CFD/GI modules (two detector channels). Two AD42m units were used in these experiments.

3.2.d. TIME-TAG MODULE

Event time tagging is accomplished by custom NIM electronics using programmable logic modules. The TTM receives triggers from the CFD corresponding to the event being integrated and subsequently digitized by the ADC. Time tags produced by the TTM are stored in memory in a synchronous fashion with the ADC

[†] Alphi Technology , 6202 S. Maple Ave. #128, Tempe, AZ 85283.
[‡] Chrisslin Industries Inc., 31312 Via Colinas, Westlake, CA 91362-3905.

outputs, thereby allowing reconstruction of the event stream preserving both energy and time. Ten channels of input can be handled by the TTM.

If other events occur during the cycle time of the integrators, the CFD sends a corresponding trigger to the TTM (refer to Fig. 3-5). The presence of these additional time tags provides a basis for event rejection during analysis. This rejection is required because the integrators are not protected from additional pulses that arrive during the cycle time. A time is recorded for a second event, and a flag is set if two or more events occur during the cycle time.

A 32-bit word is used for the time-tag data. The first 22 bits are used for recording the time of the event being integrated. This time is generated on a 4-MHz clock (250-ns resolution). The next 5 bits are used to record the time from the first event to any second event that occurs during the integration. A 16-MHz clock (62.5-ns resolution) is used to generate this time. The next bit is used as a flag to indicate whether or not two or more events occurred during the primary event. The last 4 bits are used for channel identification. Each channel in the time-tag module has a buffer that can store two results. If any of these buffers fills up, a hold is sent to the CFD that suspends all data processing until the buffers are emptied. A rollover is recorded approximately every second, providing time continuity even during holds.

A VME parallel interface, Access Dynamics[§] model DC-1, is used to interface the TTM to the memory module (another Chrisslin 256M) and the data-acquisition software.

[§] Access Dynamics Inc., 3823 Hawkins St. NE, Albuquerque, NM 87109.

The DC-1 resides on a separate VSB bus within the same VME chassis as the ADC modules and communicates directly with the second memory module.

3.2.e. SYSTEM CONTROL

Software to control the data acquisition was created with LabWindows**, a C-based programming interface to the Windows environment and VME hardware. The data-acquisition program controls the collection of data, its retrieval from the two memory modules, and collation of the energy and time data. An output file is generated with the following format: detector identification, ADC counts from the short gate (BC454), ADC counts from the long gate (BGO), event fine time, event flag, and event coarse time. The event coarse time is the primary event time and corresponds to the event integrated. Event fine time is the time between the primary time and a subsequent trigger (if any). The event flag indicates whether two or more triggers occurred during the integration. Post processing of the output from the data acquisition program is performed for analysis of the collected data.

3.3. EXPERIMENTS

Single-detector measurements were performed using small individual detectors of BC454 and BGO as well as with a BC454/BGO phoswich detector. The single-element experiments were designed to test the pulse separation electronics and analysis, as well as

---

** National Instruments, 6504 Bridge Point Parkway, Austin, TX 78730-5039.

to provide calibration data for the phoswich detector array. Simulation of the phoswich detector was accomplished by placing both individual detectors simultaneously on the face of the same photomultiplier. Tests were then conducted with a real phoswich detector, primarily to test the calibration procedure developed using the individual detector data. Several gamma-ray and neutron sources were measured, including ^{137}Cs, ^{54}Mn, AmLi, and ^{252}Cf.

An array of four detectors in a close-packed geometry was used in proof-of-principle measurements to explore the possible quantitative capability of the detection system for assay of SNM. Sources were placed between the detectors in the housing as shown in Fig. 3-3. Measurements were made of ^{137}Cs, ^{54}Mn, AmLi, ^{252}Cf, and a small sample of plutonium.

3.3.a. SINGLE DETECTOR

A preamplifier and high-voltage bleeder were coupled to a bare photomultiplier tube for the individual-detector experiments. Optical coupling jelly was used to join the detector and photomultiplier tube. A schematic of the experimental configuration is shown in Fig. 3-7, showing the detector configuration and electrical connections (output, test in, low voltage LV, and high voltage HV).

Specifications of the two individual detectors are given in Table 3-1. Both detectors were covered with a coating of white paint on all surfaces except one end. The optically coupled photomultiplier tube and detector were placed in a light-tight housing containing feedthroughs for HV, LV, test input, and signal output connections.

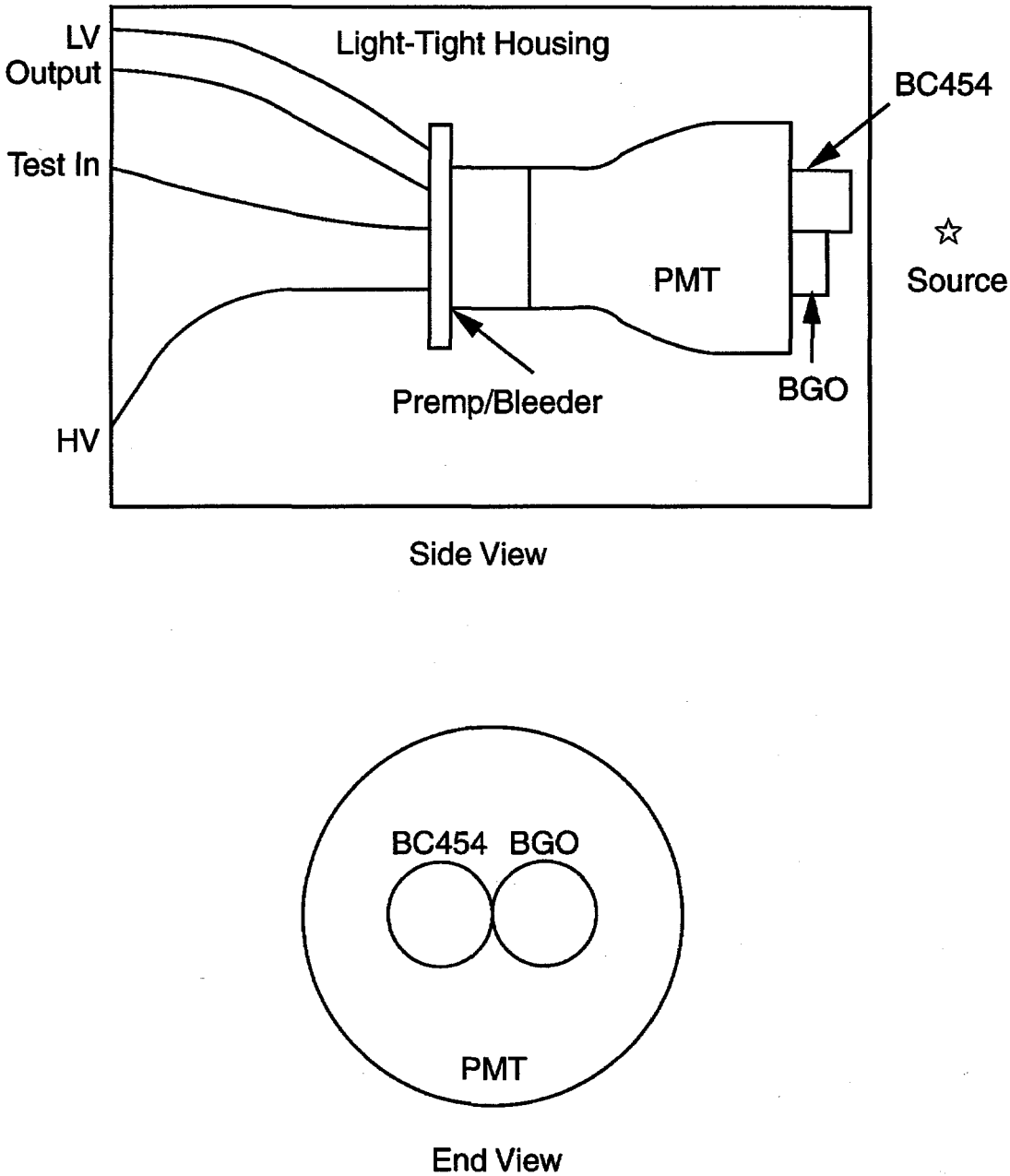

Figure 3-7. Experimental Configuration used for Individual Detector Measurements

Table 3-1. Specifications of the Small Individual BC454 and BGO Detectors

Detector	Diameter (cm)	Height (cm)	Volume (cm^3)
BC454	2.0	2.0	2π
BGO	2.0	0.5	$\pi/2$

Sources were placed in front of the detector/photomultiplier tube arrangement on the outside of the light-tight housing. Rates were kept low to minimize any electronic deadtime effects. The location of each detector was kept constant relative to the center of the photomultiplier tube in each measurement: BC454 only, BGO only, and BC454 plus BGO.

Figures 3-8 and 3-9 show the responses to ^{137}Cs for the G_1 (short-gate) integration and G_2 (long-gate) integration for the case where only the BC454 detector was present. In Fig. 3-8 we see the expected Compton spectrum, including the Compton edge (corresponding to 478 keV). Figures 3-10 and 3-11 present similar spectra from the BGO-only measurement. The upper part of Fig. 3-11 shows the familiar photopeak (662keV) and Compton continuum. Even though only a single detector is present for each of these measurements, data exists in both the G_1 and G_2 gates because pulses for either BC454 or BGO overlap both gates (see Fig. 3-6). The counts that must be removed from the G_1 and G_2 gates and restored for the BC454 and BGO responses to be complete are shown in Figs. 3-9 and 3-10, for the case of the BC454-only and BGO-only measurements respectively. This correction is done during post processing. Figures 3-12 and 3-13 contain the G_1 and G_2 spectra from the ^{137}Cs source obtained when both the BC454 and BGO detectors were in place, an arrangement that simulates the phoswich

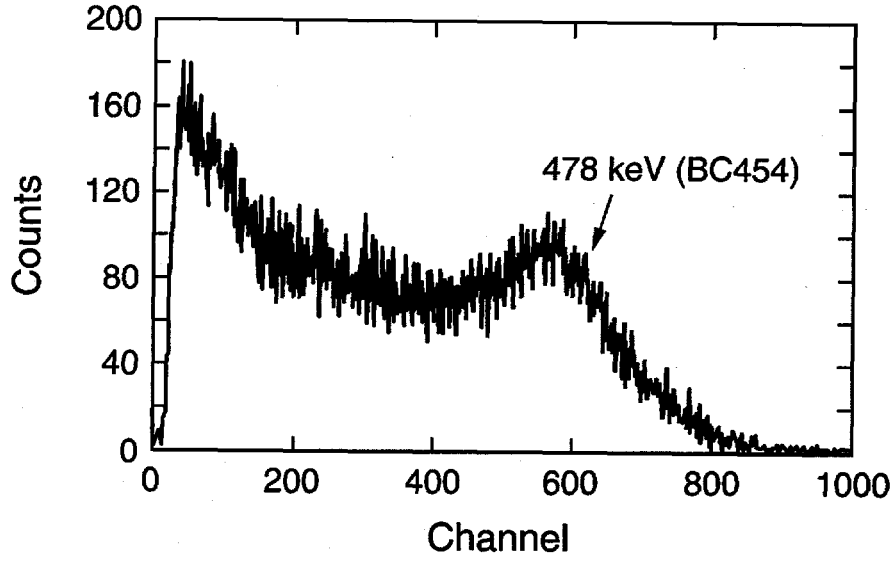

Figure 3-8. G_1 Spectrum of ^{137}Cs Obtained from BC454 Only

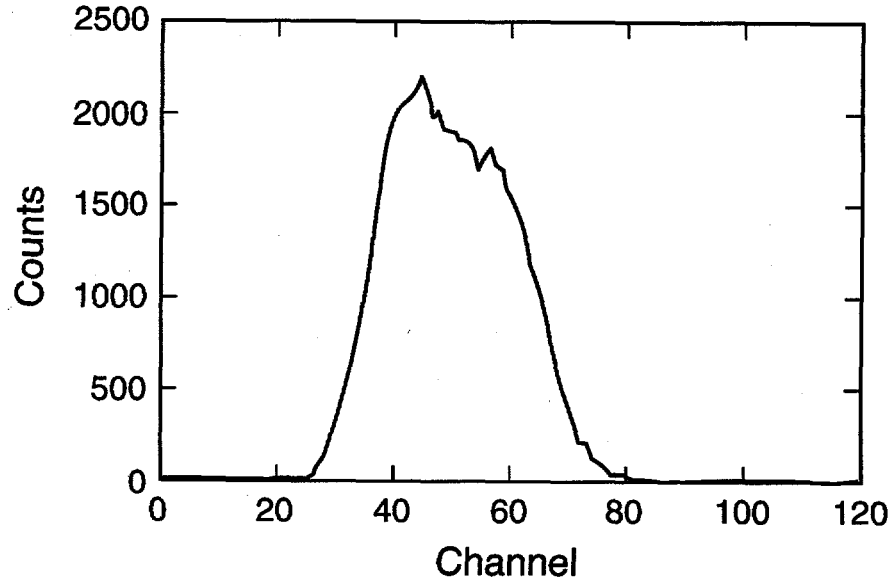

Figure 3-9. G_2 Spectrum of ^{137}Cs Obtained from BC454 Only

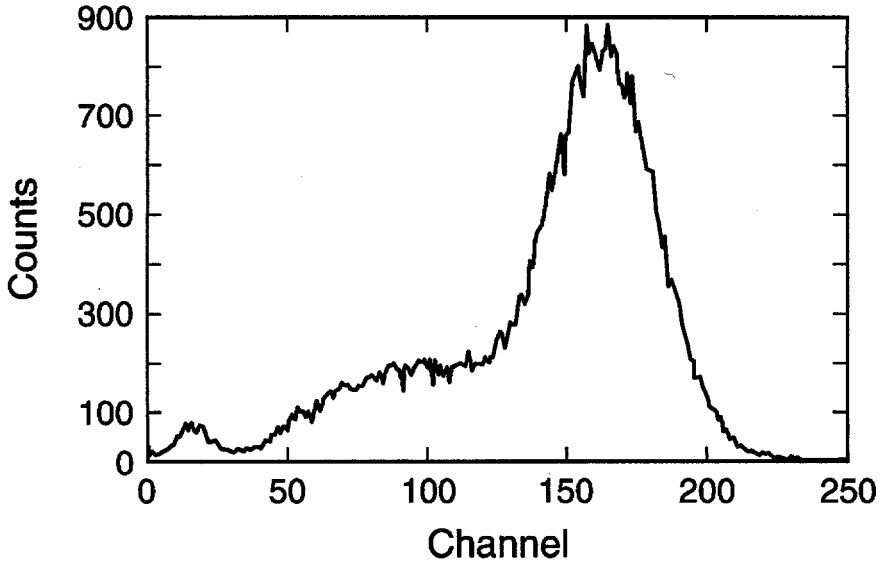

Figure 3-10. G_1 Spectrum of ^{137}Cs Obtained from BGO Only

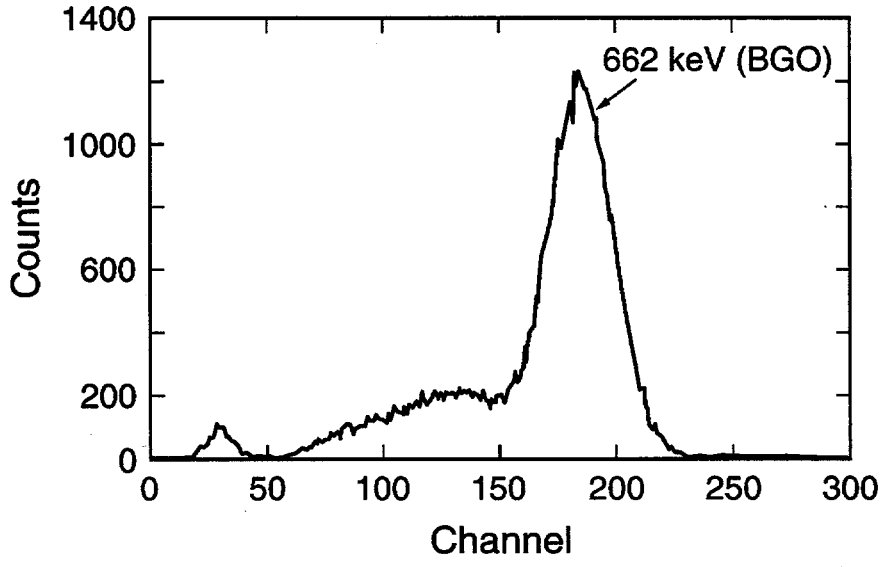

Figure 3-11. G_2 Spectrum of ^{137}Cs Obtained from BGO Only

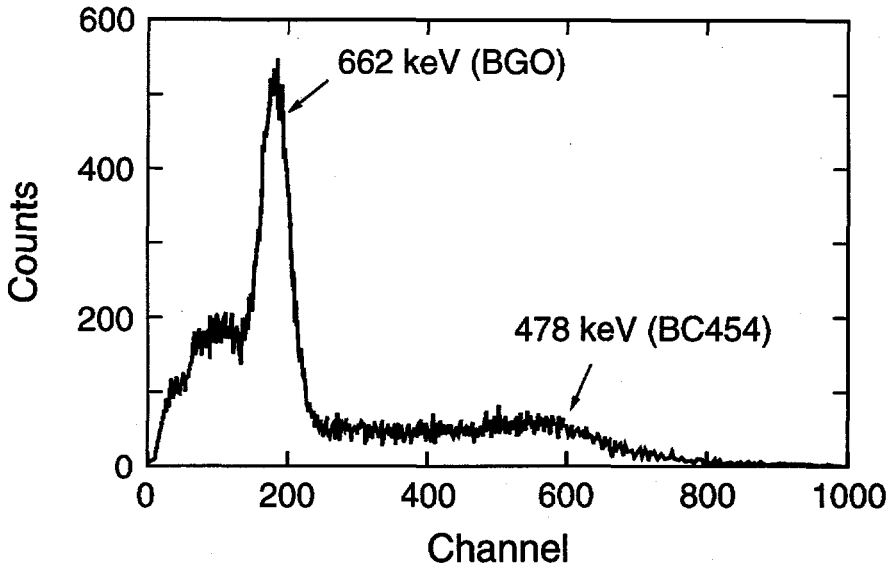

Figure 3-12. G_1 Spectrum of ^{137}Cs Obtained from BC454 plus BGO

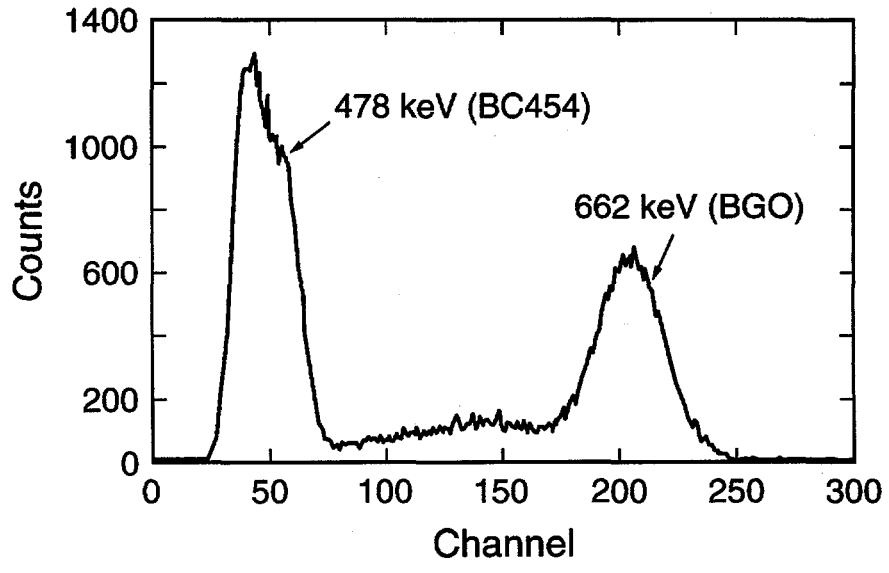

Figure 3-13. G_2 Spectrum of ^{137}Cs Obtained from BC454 plus BGO

detector actually used. Successful correction of these spectra was used to demonstrate proper pulse separation. Similar sets of measurements were made with a ^{54}Mn source. Measurements were also made of a ^{252}Cf source with the BC454 scintillator alone. Data were acquired under the following conditions: 1) the source was enclosed in a lead/polyethylene shield with an additional 5 cm of polyethylene between the source and detector (thermal spectrum), 2) the source was shielded only by lead (fast spectrum), and 3) the source was in the same configuration as 1), but the 5-cm polyethylene was replaced by boron-loaded polyethylene (fast spectrum). Figures 3-14 through 3-16 show these spectra. In Fig. 3-14 we see a large peak in the lower part of the spectrum that is not present in either Figs. 3-15 or 3-16. This peak corresponds to the 93-keV_{ee} neutron capture peak discussed in Chapter 1 (see Fig. 1-5). It is nearly absent in the fast spectra of Figs. 3-15 and 3-16 because the detector is too small to provide efficient moderation of the source by itself. Therefore, when the source spectrum was modified by either removing moderation or replacing it with a thermal-neutron absorbing material, the 93-keV_{ee} peak was reduced significantly.

A set of spectra was also taken with a combined BC454/BGO phoswich detector, in an experimental configuration similar to that of the individual detector measurements. Figures 3-17 and 3-18 are the G_1 and G_2 spectra from ^{137}Cs. These spectra are more complicated than their individual detector counterparts because 1) both elements of the detector are larger than the individual detector, 2) the geometry of the two elements is different, with BGO completely surrounding the BC454, and 3) the actual physical coupling to the photomultiplier tube is different. Nevertheless, the spectra are similar enough to identify the Compton edge in Fig. 3-17 and photopeak in Fig. 3-18.

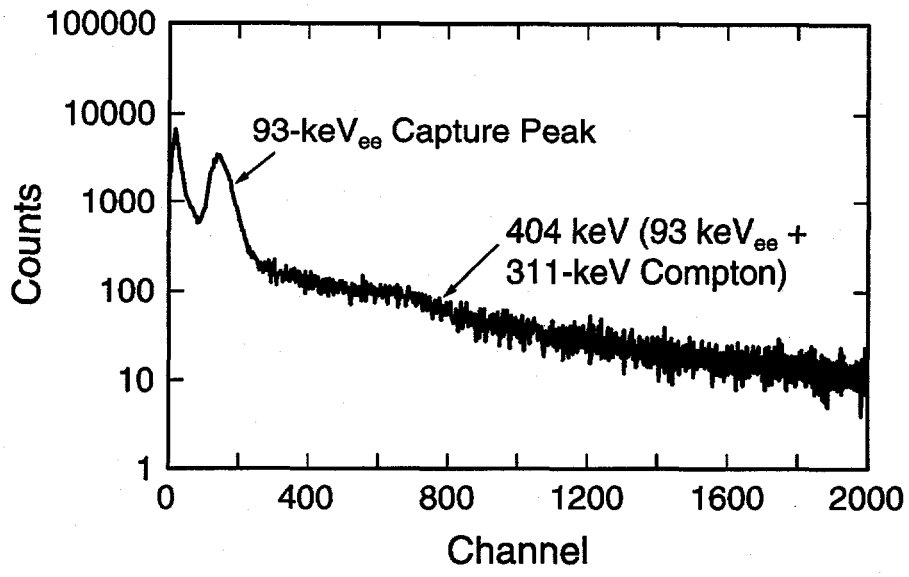

Figure 3-14. G_2 Spectrum of ^{252}Cf Obtained from BC454 With Moderation

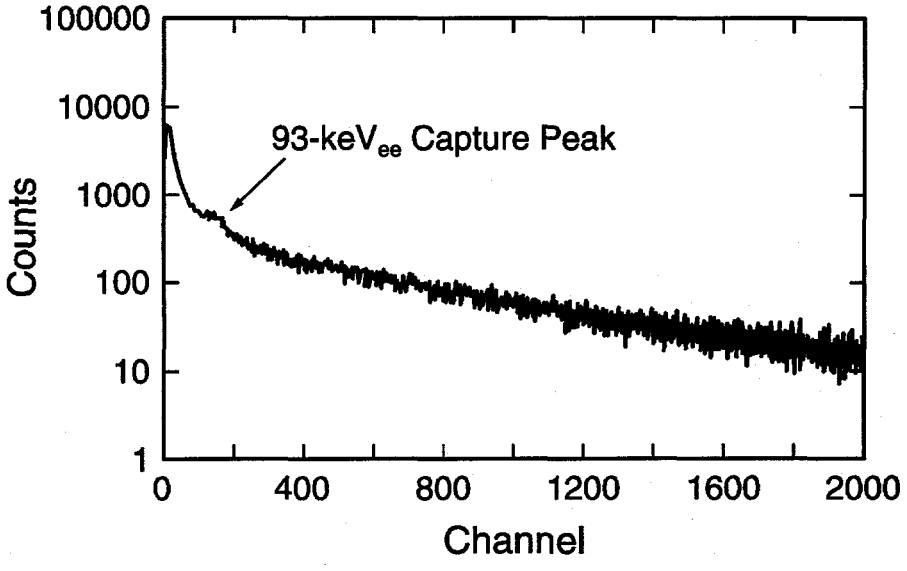

Figure 3-15. G_2 Spectrum ^{252}Cf Obtained from BC454 Without Moderation

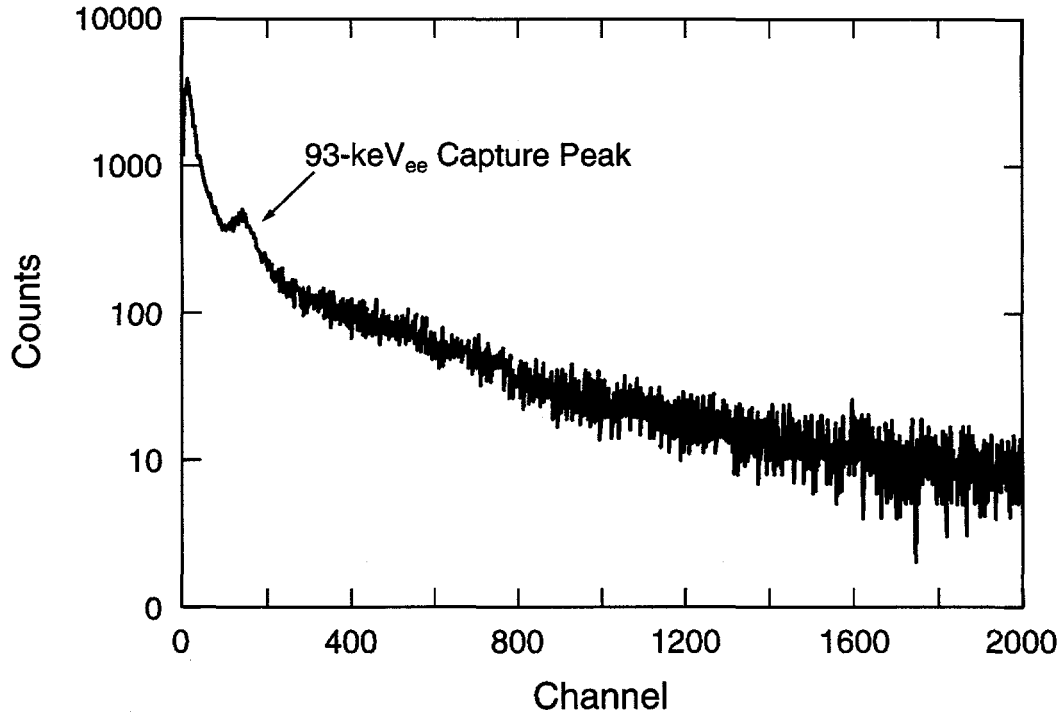

Figure 3-16. G_2 Spectrum ^{252}Cf Obtained from BC454 With Absorptive Moderation

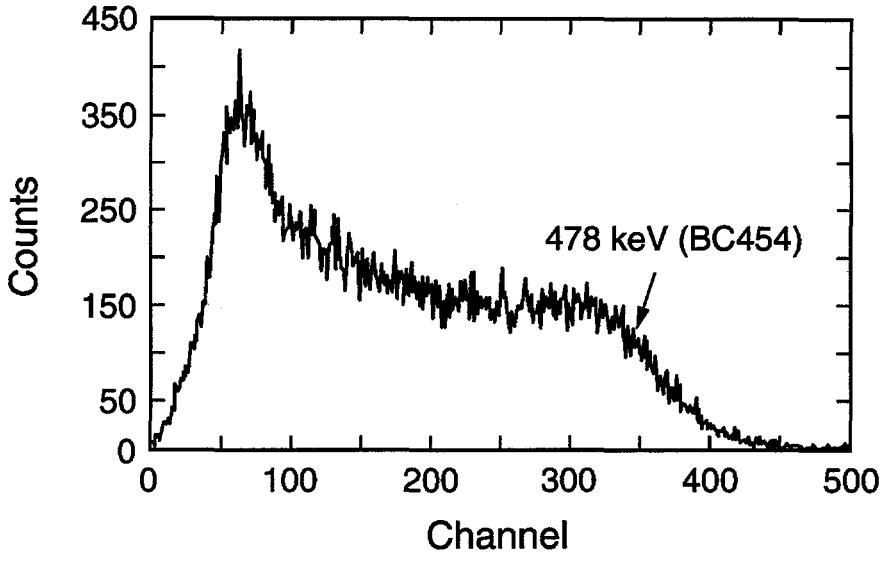

Figure 3-17. G_1 Spectrum of ^{137}Cs Obtained with BC454/BGO Phoswich

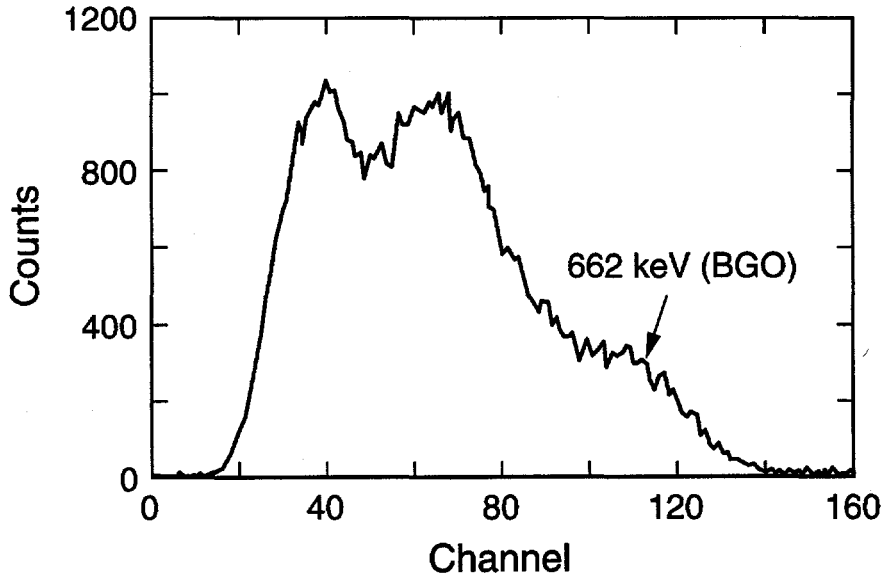

Figure 3-18. G_2 Spectrum of ^{137}Cs Obtained with BC454/BGO Phoswich

Neutron spectra were collected with the phoswich detector as well. A ^{252}Cf source was placed in the lead/polyethylene shield with 5 cm of polyethylene between the source and detector. The spectra are shown in Figs. 3-19 and 3-20 for the G_1 and G_2 outputs, respectively. Comparison to Fig. 3-14 shows a large difference because there is a BGO component in the signal, whereas this is not the case for Fig. 3-14. In each spectrum, however, there is a discernible feature corresponding to the neutron-capture signature. Separating these two spectra completely is accomplished during post processing of the data and is described in Chapter 4, Analysis and Simulation.

Another feature that is clear from Figs. 3-8 through 3-13 is that the gains of the G_1 and G_2 channels are not equal, as is especially evident by the compression of the BC454 signal in the G_2 gate for the BC454-only ^{137}Cs data (Fig. 3-9). This difference is important in the final separation of the BC454 and BGO data and was measured by injection of a pulse pair of equal shape and amplitude. Each pulse was shorter than the short gate (80 ns) and spaced such that one would be integrated fully in G_1 and the other in G_2 (see Fig. 3-21).

Table 3-2 presents the results of the relative gain measurements for each of the preamplifier and GI combinations used.

Table 3-2. Relative Gain Results for Specific Preamplifier/GI Assemblies

Flight Assembly No.	Gated Integrator No.	Relative Gain (k)
FA0[a]	2	1.830
FA17	1	1.926
FA20	2	1.820
FA21	3	1.674
FA18	4	1.843

[a]Preamplifier used with individual BC454 and BGO detectors.

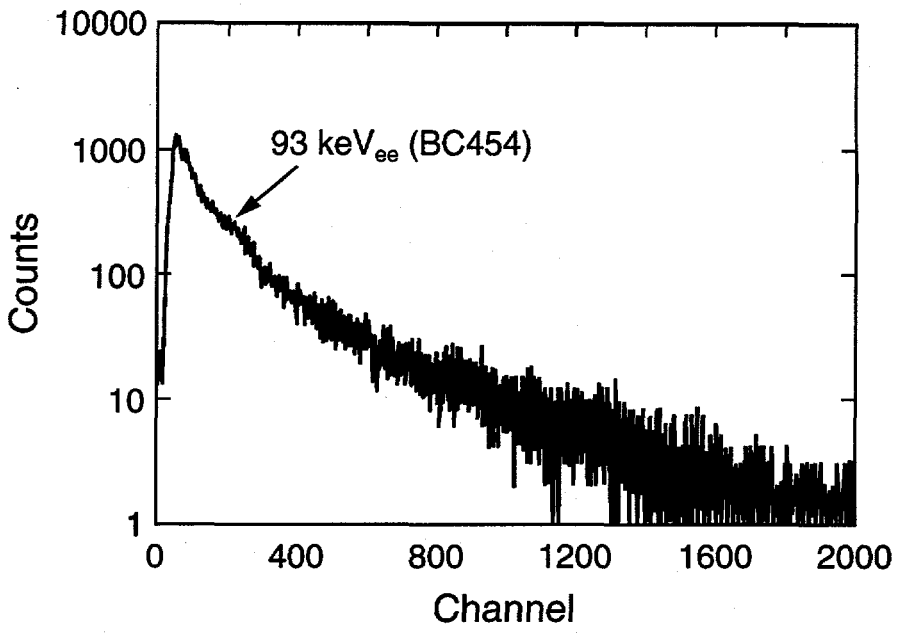

Figure 3-19. G_1 Spectrum of ^{252}Cf Obtained with BC454/BGO Phoswich

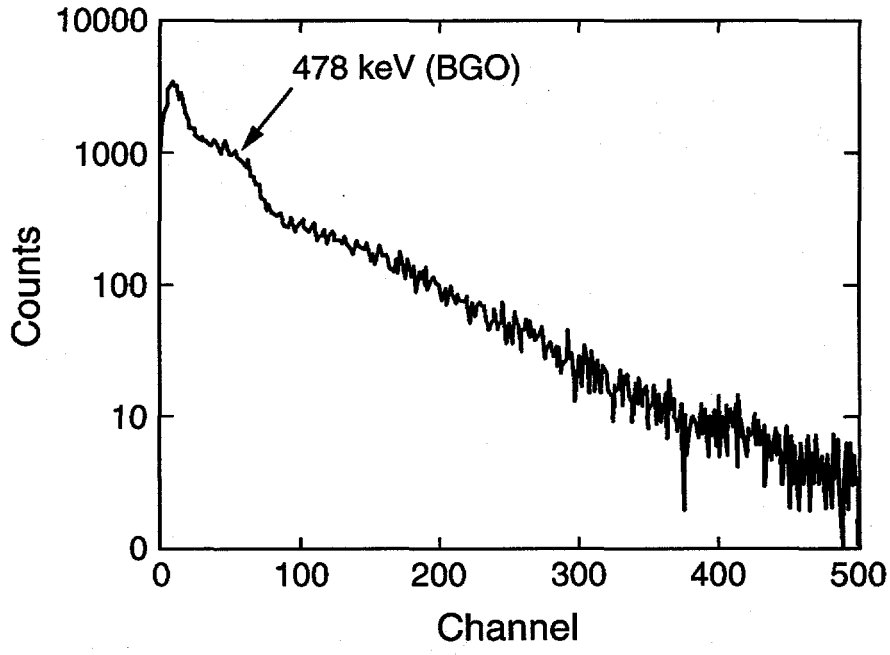

Figure 3-20. G_2 Spectrum of ^{252}Cf Obtained with BC454/BGO Phoswich

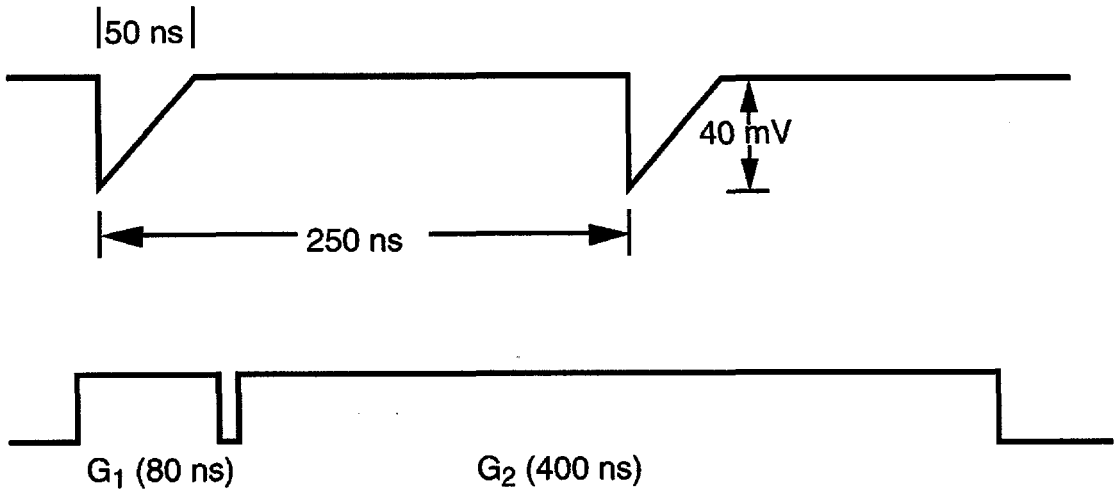

Figure 3-21. Pulse Pair Used to Determine the Relative Gain Parameter, k

3.3.b. MULTIPLE DETECTOR

In addition to the single-detector experiments, an array of four phoswich detectors was constructed in a close-packed geometry. A relatively high-solid-angle geometry was chosen to maximize the neutron capture probability so that time-correlation analysis could be performed with sufficient precision. Data were collected from a variety of sources, including ^{137}Cs, ^{54}Mn, AmLi, ^{252}Cf, and a small plutonium sample. The detectors were configured as shown in Fig. 3-3, and samples were placed in the central sample cavity (Fig. 3-4). The primary goal of these measurements was to demonstrate proof-of-principle for the potential application of BC454/BGO detector arrays in quantitative measurements using energy discrimination and time-correlation analysis.

A simple indication of the system's ability to be sensitive to fission is obtained by taking the time difference between successive events and plotting the result as a histogram (interval distribution). Figures 3-22 through 3-24 show these results for the 4-detector array for ^{137}Cs, AmLi, and ^{252}Cf sources, respectively. On a logarithmic plot the interval distribution of a random source is a straight line corresponding to the singles count rate. Any correlation in the detected events is seen as an increase in the slope at short times. As can be seen from Figs. 3-22 through 3-24, both ^{137}Cs and AmLi appear random; the only source exhibiting correlations is the ^{252}Cf.

Time-correlation analysis of the 4-detector array data is presented in Chapter 4, Analysis and Simulation. In Chapter 5 this analysis is applied to the quantitative determination of the source. In addition, detector simulations are performed and compared to the experimental data.

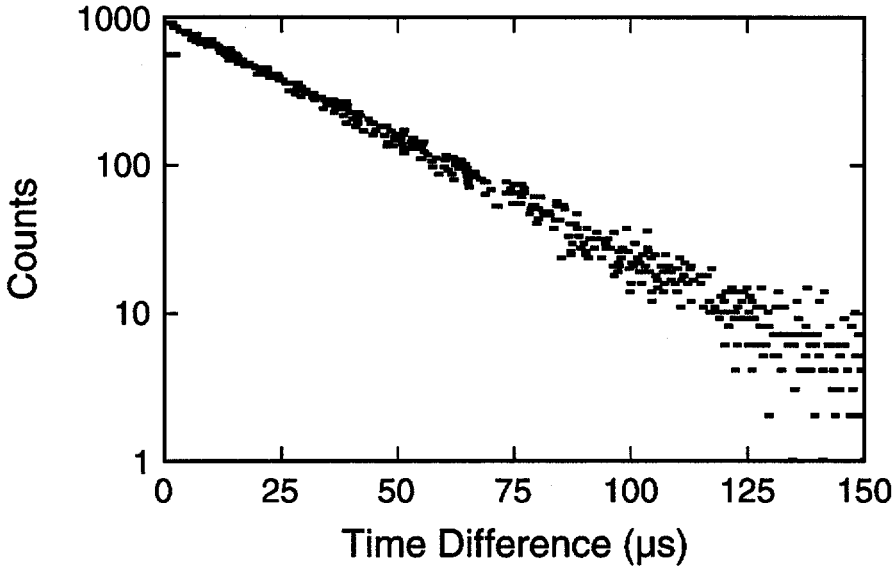

Figure 3-22. Interval-Distribution Spectrum for ^{137}Cs

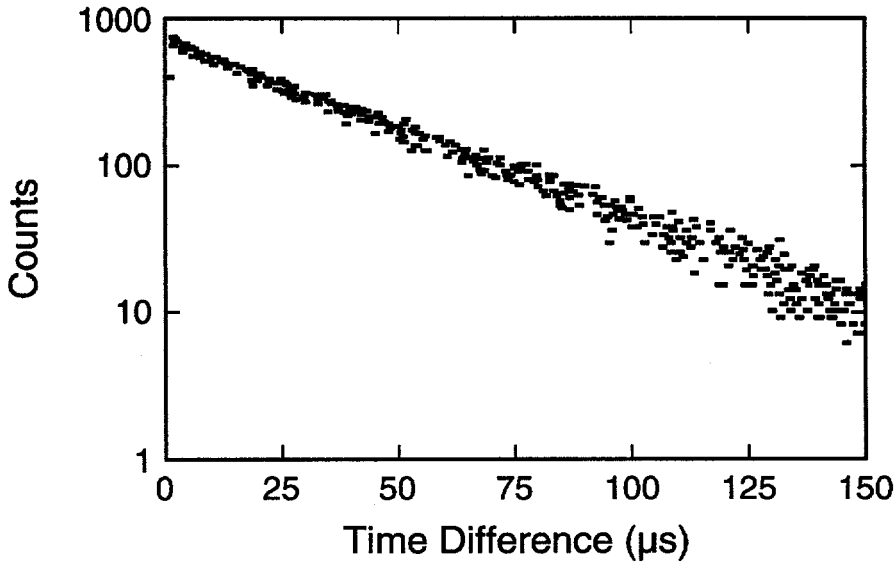

Figure 3-23. Interval-Distribution Spectrum for AmLi

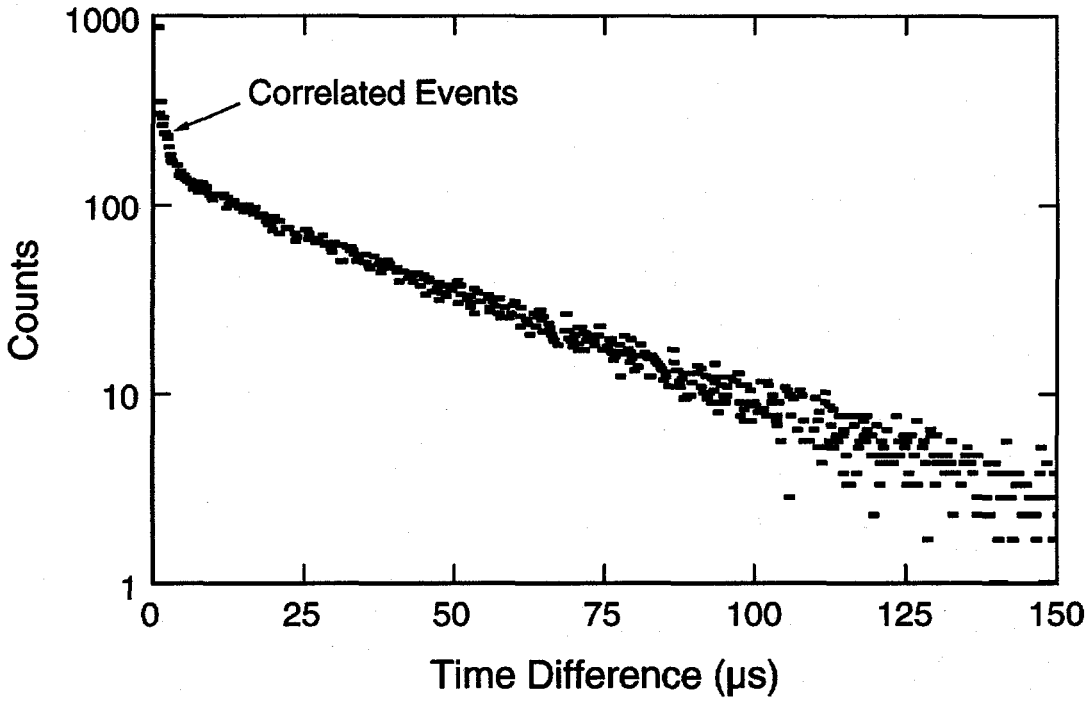

Figure 3-24. Interval-Distribution Spectrum for ^{252}Cf

4. ANALYSIS AND SIMULATION

4.1. INTRODUCTION

Analysis and simulation techniques applied to the data obtained from the experiments described in Chapter 3 included: pulse-shape model for separation of BC454 and BGO response, computer simulation of the detector response to both neutrons and gamma rays for evaluation of the relative merits of neutron discrimination via neutron capture in the BC454 versus neutron capture in BC454 in coincidence with the detection of the 478-keV neutron capture gamma ray in the BGO element, and time-correlation analysis of the time-tagged event data.

Calibration of the BC454/BGO detector array for the quantitative assay of nuclear material based on time-correlated neutron emission rates requires the following steps:

1) The combined BC454 and BGO output pulse is separated into its component parts.
2) An energy calibration is performed for each BC454 and BGO element pair.
3) Discrimination of neutron events is accomplished using the results of the energy calibrations.
4) Time-correlation analysis is performed on the resulting time-tagged event stream.

Results of this calibration procedure were compared against computer simulations in which the neutron capture probability was estimated and then used to validate the multiplicity point model.

4.2. PULSE SEPARATION

The CFD/GI module performs only a first-order pulse separation of the BC454 and BGO response, with the complete separation being accomplished pulse-by-pulse during post processing. After conversion by the ADC, the digitized GI outputs of the pulse area residing within G_1 and G_2 are given by

$$I_1 = f_{P1}P + f_{B1}B + O_1, \tag{4-1}$$

and

$$I_2 = \frac{1}{k}\left(f_{P2}P + f_{B2}B\right) + O_2 \tag{4-2}$$

where

P, B = total digitized BC454 (P) and BGO (B) pulse areas (completely integrated pulse),

I_1, I_2 = digitized pulse integration values for the G_1 and G_2 integrator channels,

k = relative gain for the G_1 and G_2 integrator channels,

f_{P1}, f_{P2} = fraction of BC454 pulse area residing within the G_1 and G_2 integrator channels,

f_{B1}, f_{B2} = fraction of BGO pulse area residing within the G_1 and G_2 integrator channels, and

O_1, O_2 = digitized integration value of baseline offset for the G_1 and G_2 integrator channels.

Figure 4-1 shows an analytical model of the BC454 and BGO pulse shape, where $f(t)$ and $g(t)$ are given by (each normalized as probabilities)

$$f(t) = \left(\frac{1}{6\tau_P^4}\right) t^3 e^{-t/\tau_P} \tag{4-3}$$

and

$$g(t) = \frac{1}{\tau_{B1} - \tau_{B2}} \left(e^{-t/\tau_{B1}} - e^{t/\tau_{B2}} \right), \tag{4-4}$$

where

$f(t)$ = model for BC454 pulse shape,

$g(t)$ = model for BGO pulse shape,

τ_P = shaping parameter for BC454 pulse shape ($\tau_P = 15$ ns), and

τ_{B1}, τ_{B2} = shaping parameters for BGO pulse shape ($\tau_{B1} = 60$ ns, and $\tau_{B2} = 180$ ns).

The pulse-shape model for the BC454 output is Gaussian with n = 3, while that for the BGO output is RC-CR.[42]

If k, $f_{P1}, f_{P2}, f_{B1}, f_{B2}$, O_1, and O_2 are known, the solutions for P and B from Eqs. 4-1 and 4-2 are given by

$$P = \frac{f_{B2}(I_1 - O_1) - f_{B1} k (I_2 - O_2)}{f_{P1} f_{B2} - f_{P2} f_{B1}} = a(I_1 - O_1) - b(I_2 - O_2) \tag{4-5}$$

and

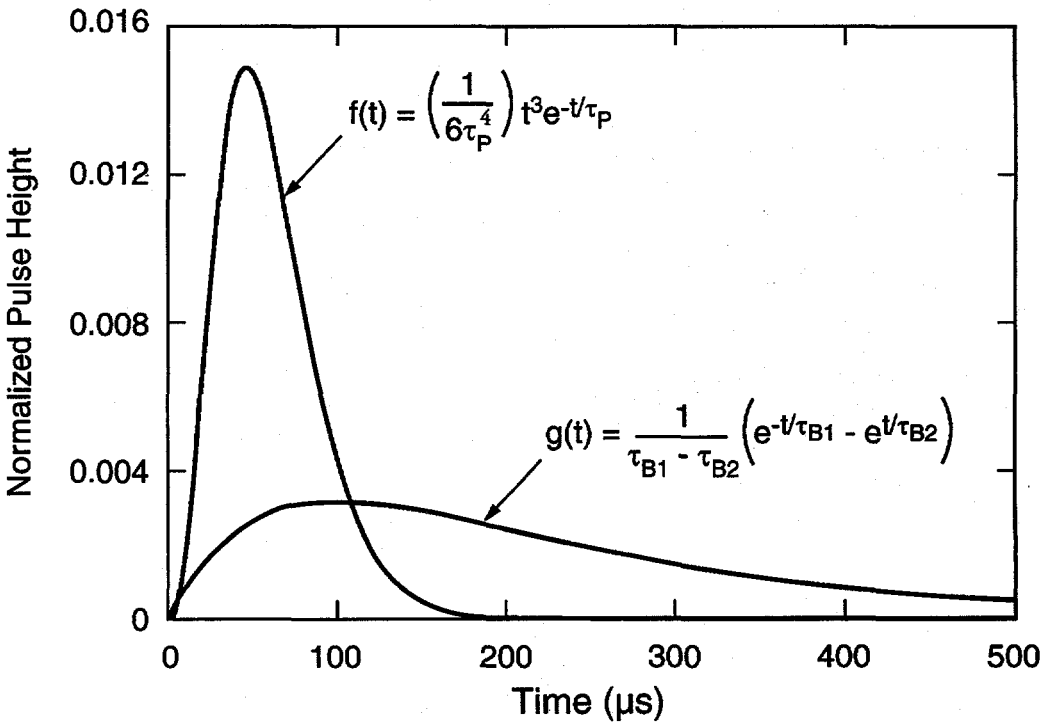

Figure 4-1. Analytical Representation of Detector Element Pulse Shapes

$$B = \frac{f_{P1}k(I_2 - O_2) - f_{P2}(I_1 - O_1)}{f_{P1}f_{B2} - f_{P2}f_{B1}} = c(I_2 - O_2) - d(I_1 - O_1). \tag{4-6}$$

As described in Chapter 3, the relative gain k of the G_1 and G_2 channels (see Table 3-2) was obtained by the introduction of a matched pulse pair into each preamplifier/GI combination, where the width of each pulse and the spacing between the pair were such that they fully resided within the time windows for each gate (see Fig. 3-21).

Fractions of the BC454 and BGO pulses that are integrated in the G_1 and G_2 gates can be measured experimentally using single detectors of BC454 and BGO as well as estimated analytically using the model for each pulse shape described above. Analytical determinations are accomplished by integration of Eqs. 4-3 and 4-4 over the times that correspond to the gate lengths in G_1 and G_2,

$$f_{P1} = \int_0^{t_1} f(t)dt = \frac{1}{6\tau_P^4}\left\{\begin{array}{l} -\tau_P t_1^3 e^{-t_1/\tau_P} \\ +3\tau_P\left[-\tau_P t_1^2 e^{-t_1/\tau_P} + 2\tau_P\left(-\tau_P t_1 e^{-t_1/\tau_P} - \tau_P^2 e^{-t_1/\tau_P} + \tau_P^2\right)\right] \end{array}\right\}, \tag{4-7}$$

$$f_{P2} = 1 - f_{P1}, \tag{4-8}$$

$$f_{B1} = \int_0^{t_1} g(t)dt = \frac{1}{\tau_{B1} - \tau_{B2}}\left[-\tau_{B1}\left(e^{-t_1/\tau_{B1}} - 1\right) + \tau_{B2}\left(e^{-t_1/\tau_{B2}} - 1\right)\right], \text{ and} \tag{4-9}$$

$$f_{B2} = \int_{t_1}^{t_2} g(t)dt = \frac{1}{\tau_{B1} - \tau_{B2}}\left[-\tau_{B1}\left(e^{-t_2/\tau_{B1}} - e^{-t_1/\tau_{B1}}\right) + \tau_2\left(e^{-t_2/\tau_{B2}} - e^{-t_1/\tau_{B2}}\right)\right]. \tag{4-10}$$

Evaluation of the above equations using gate times corresponding to 80 and 400 ns for G_1 and G_2 respectively (t_1 = 80 ns and t_2 = 480 ns) and shaping parameters of τ = 15 ns (BC454), τ_1 = 80 ns, and τ_2 = 180 ns (BGO) yields the following pulse fractions ($O_1 = O_2 = 0$)

$f_{P1} = 0.775$,

$f_{P2} = 0.225$,

$f_{B1} = 0.168$, and

$f_{B2} = 0.728$.

Gate fractions of the BC454 and BGO pulses were also measured experimentally using the FA0/GI#2 combination and individual detectors of BC454 and BGO. Data obtained from the BC454-only and the BGO-only experiments can be used to define the fractions of each pulse in the G_1 and G_2 integration windows. Setting $B = 0$ in Eq. 4-1 and solving yields

$$\frac{f_{P1}}{f_{P2}} = \frac{I_1 - O_1}{k(I_2 - O_2)} \tag{4-11}$$

and setting $P = 0$ in Eq. and 4-2 and solving yields

$$\frac{f_{B1}}{f_{B2}} = \frac{I_1 - O_1}{k(I_2 - O_2)}, \tag{4-12}$$

where I_1 and I_2 correspond to the digitized integration values obtained for either the BC454 or BGO only. It is further noted that the entire BC454 pulse resides within the total integration time of 480 ns, whereas the BGO pulse does not, leading to the following relationships

$$f_{P1} + f_{P2} = 1 \tag{4-13}$$

and

$$f_{B1} + f_{B2} = X, \tag{4-14}$$

where X is the fraction of the BGO pulse area residing in the sum of the two gates. In the case of the analytical model described above, $X = 0.90$. Figure 4-2 shows the analytical model superimposed on a plot obtained from a digital oscilloscope.

Combining Eqs. 4-11 through 4-14 yields the following solutions for the fractions of BC454 and BGO pulses in the G_1 and G_2 integration windows:

$$f_{P1} = \frac{1}{\left(1 + \frac{k(I_2 - O_2)}{I_1 - O_1}\right)}, \tag{4-15}$$

$$f_{P2} = 1 - f_{P1}, \tag{4-16}$$

$$f_{B1} = \frac{X}{\left(1 + \frac{k(I_2 - O_2)}{I_1 - O_1}\right)}, \tag{4-17}$$

and

$$f_{B2} = X - f_{B1}. \tag{4-18}$$

Because the offsets O_1 and O_2 appear in the solutions for P and B (Eqs. 4-5 and 4-6), as well as for the pulse fractions given above, iteration is required to obtain the final values for the pulse-separation algorithm. The iteration scheme is as follows:

1) Determine initial values of f_{P1}, f_{P2}, f_{B1}, and f_{B2} from Eqs. 4-15 to 4-18 using I_1 and I_2, setting $O_1 = O_2 = 0$, and inserting the measured value of k from Table 3-2.
2) Calculate a, b, c, and d (Eqs. 4-5 and 4-6).
3) Calculate P and B using I_1 and I_2 for the energy-calibration source runs (^{137}Cs and ^{54}Mn).

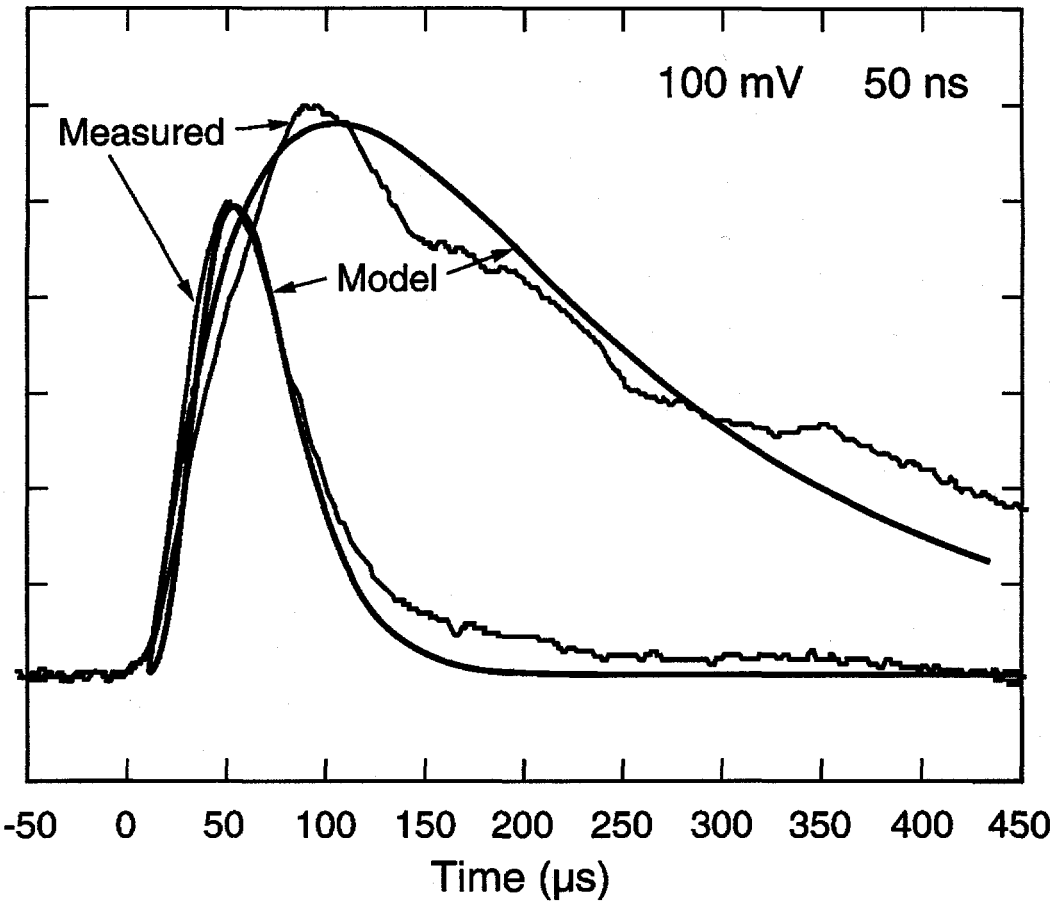

Figure 4-2. Comparison of Analytical Model and Actual Pulse Shape

4) Perform an energy calibration for both the BC454 and BGO, obtaining an estimate for O_1 and O_2.

5) Recalculate f_{P1}, f_{P2}, f_{B1}, and f_{B2} with the O_1 and O_2.

6) Iterate through steps 2–5 until the new energy calibration agrees with the previous one.

Performing this analysis with the single-detector BC454 and BGO data gives the parameters listed in Table 4-1, with $X = 0.90$. Values obtained using the analytical model are included for comparison.

Table 4-1. Gated Integrator #2 Calibration Results

Parameter	Measured	Calculated	Measured/Calculated
k	1.830	---	---
f_{P1}	0.815	0.775	1.05
f_{P2}	0.185	0.225	0.82
f_{B1}	0.331	0.168	1.97
f_{B2}	0.569	0.728	0.78

The results given in Table 4-1 show that the analytical model fractions are in relatively good agreement with the measured values except for the BGO fraction in G_1. The problem can be seen in Fig. 4-2, where the model must try to simultaneously match a short rise time and long decay with poor photon statistics (fluctuations in pulse tail). It is likely that the model for the BGO pulse tails off too slowly as compensation for matching the peaking time of 90 ns and obtaining a reasonable fit to the full width at half maximum (~300 ns), thereby underestimating the relative area of the curve in the first 80 ns.

Figures 4-3 and 4-4 present results of the calibration in spectral form, where the combined ^{137}Cs spectra shown in Figs. 3-12 and 3-13 have been separated into their

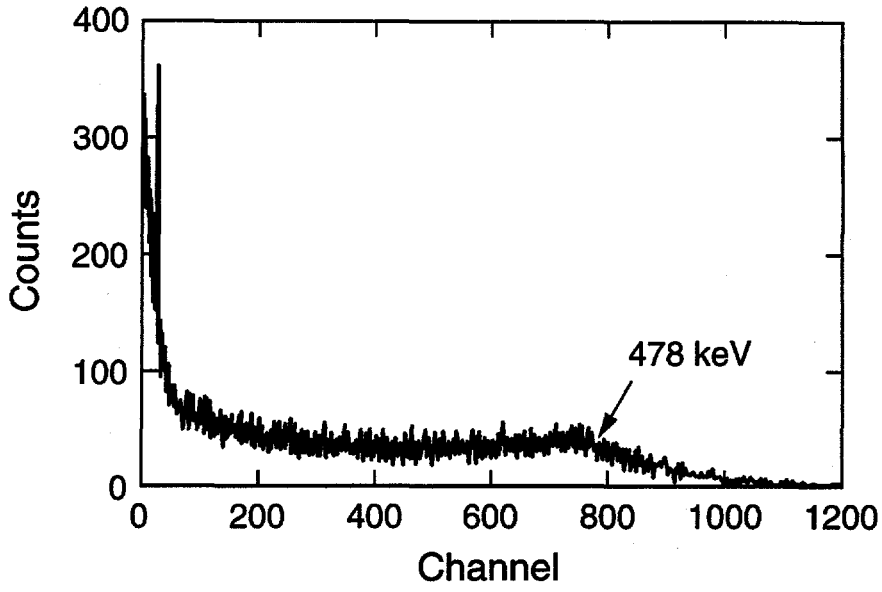

Figure 4-3. BC454 ^{137}Cs Spectrum Corrected for BGO-Individual Detectors

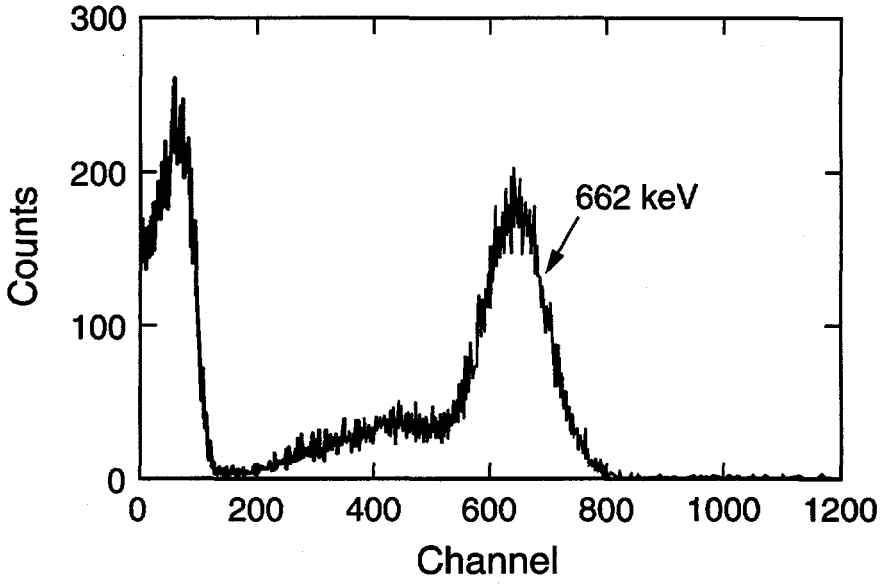

Figure 4-4. BGO ^{137}Cs Spectrum Corrected for BC454 -Individual Detectors

respective BC454 and BGO components using Eqs. 4-5 and 4-6 and the values given in Table 4-1. Ideally, the separation procedure would result in spectra exactly the same shapes as the single-detector data, with some gain change corresponding to compensation for the pulse gate fractions and relative gain between G_1 and G_2 integration channels. Comparison of Figs. 4-3 and 3-8 as well as Figs. 4-4 and 3-11 shows that while the separation is good, there are still some residual effects at the lower end of the spectrum. This results is to be expected because the individual detector data shown in Figs. 3-8 and 3-11 contain photon statistics from only one detector, either BC454 or BGO, whereas the combined detector data and its separation have contributions of photon statistics to the uncertainty from both BC454 and BGO detectors. The relative effect is greater for lower energies. However, this uncertainty does not present a problem to the isolation of neutron events because the peaks of interest reside high enough in the spectrum to avoid any significant problems.

Spectra of ^{54}Mn were also taken, the separation procedure was applied, and energy calibrations were determined for both BC454 and BGO detectors. Figures 4-5 and 4-6 present the separated spectra. Table 4-2 contains the results of the energy calibration ($E = x + y\text{ch}$).

Table 4-2. Energy Calibration for Single Detector Data

	Photopeak (BGO)		Compton Edge (BC454)	
Nuclide	E (keV)	Channel (ch)	E (keV)	Channel (ch)
^{137}Cs	662	640	478	800
^{54}Mn	834	790	638	1100
x (keV)	-71.9		51.3	
y (keV/ch)	1.147		0.5333	

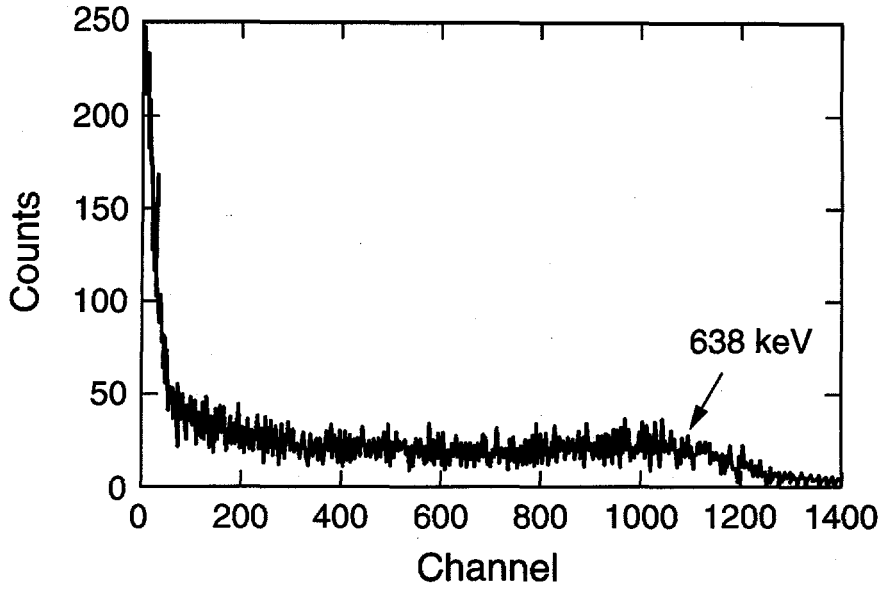

Figure 4-5. BC454 ^{54}Mn Spectrum Corrected for BGO -Individual Detectors

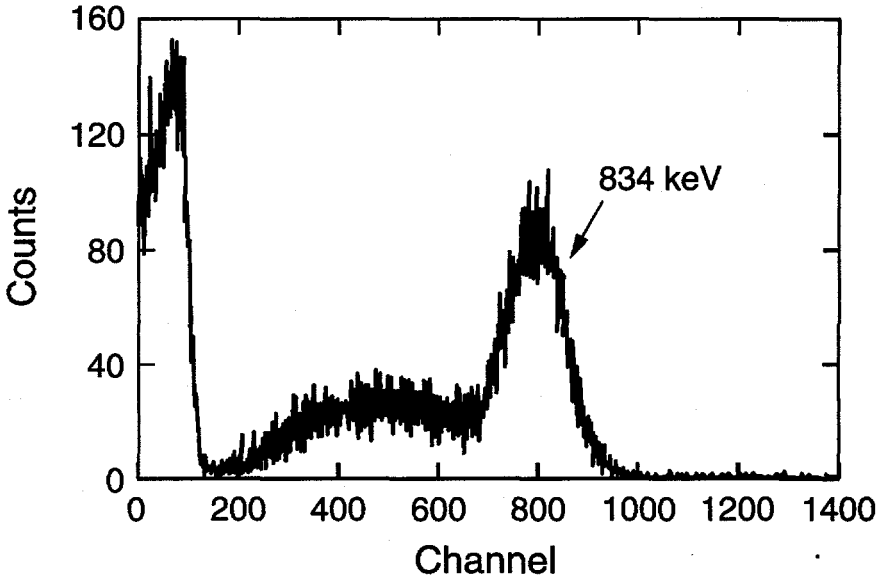

Figure 4-6. BGO ^{54}Mn Spectrum Corrected for BC454 -Individual Detectors

Taking the energy calibration values and applying the separation procedure to a neutron source collected with both BC454 and BGO detectors in place results in the spectrum shown in Fig. 4-7. The dashed lines in Fig. 4-7 indicate the expected locations of the 93-keV$_{ee}$ neutron capture peak and 180° Compton scatter of the 478-keV capture gamma ray, is located at 404 keV (93 keV$_{ee}$ + 311 keV Compton electron). Unlike the actual phoswich detectors, the simulated phoswich with both BC454 and BGO detectors on the PMT does not result in much of a BGO spectrum because of the geometry of the two detectors and the probability for capture of the 478-keV gamma ray is quite small. In the case of the actual detector, however, BGO completely surrounds the BC454 and a significant 478-keV peak is present.

Table 4-3 contains the calibration parameters for the detector/GI combinations used in the four-detector array measurements. The measured results of the pulse fractions (Table 4-1) were combined with the relative gain values for each detector channel (Table 3-2) to obtain values for the pulse-separation parameters *a*, *b*, *c*, and *d*. Final values for the DC offsets O_1 and O_2 were obtained by iteration. Once the final parameters were determined, a final energy calibration was performed for each channel. Table 4-4 presents the results of the energy calibrations (E = x + $y$ch). Figures 4-8 and 4-9 show the separated phoswich spectra for the ^{137}Cs source in Figs. 3-17 and 3-18. The result of separating the ^{252}Cf spectra in Figs. 3-19 and 3-20 is given in Figs. 4-10 and 4-11.

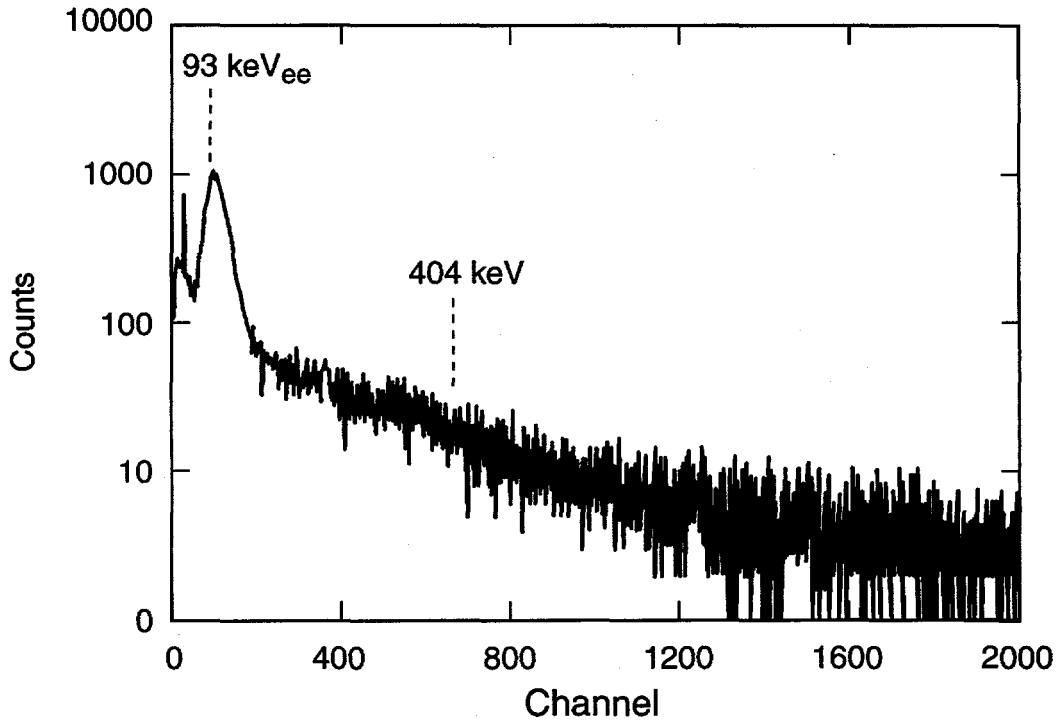

Figure 4-7. BC454 Neutron Spectrum Corrected for BGO- Individual Detectors

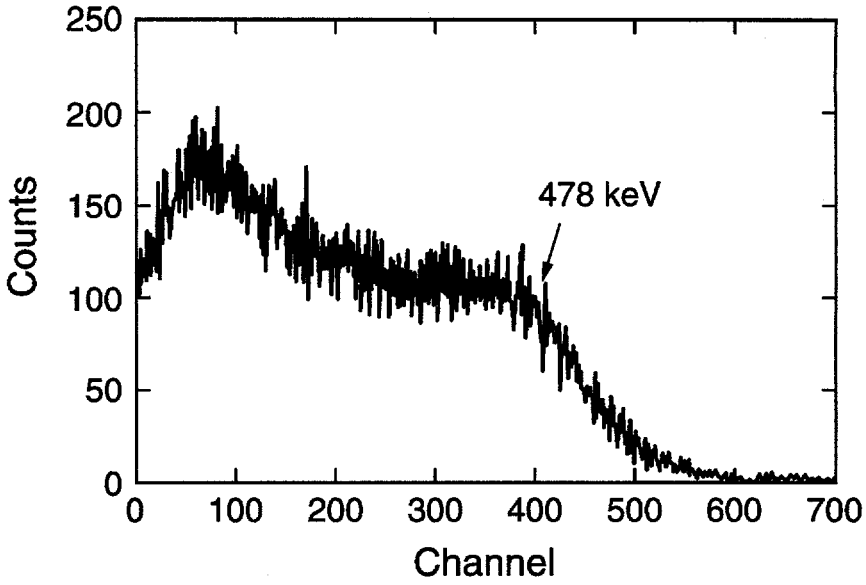

Figure 4-8. Phoswich BC454 ^{137}Cs Spectrum Corrected for BGO

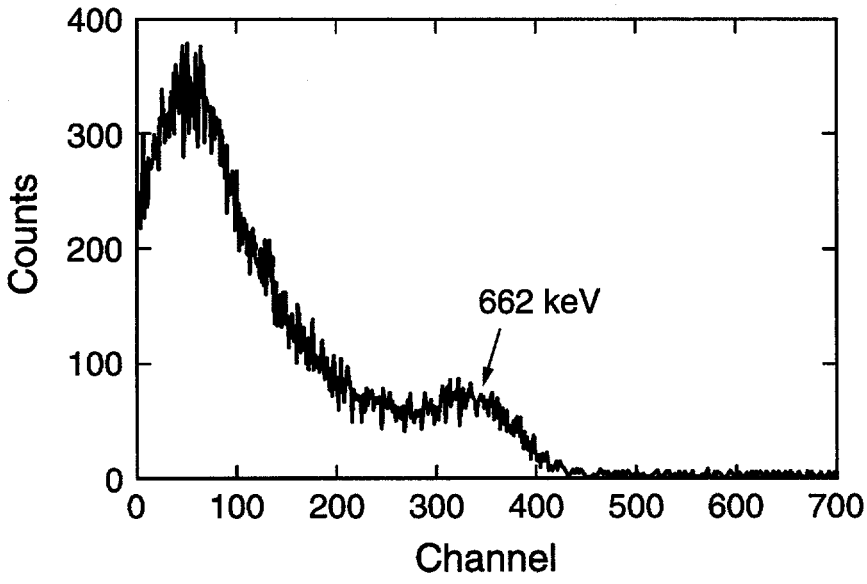

Figure 4-9. Phoswich BGO ^{137}Cs Spectrum Corrected for BC454

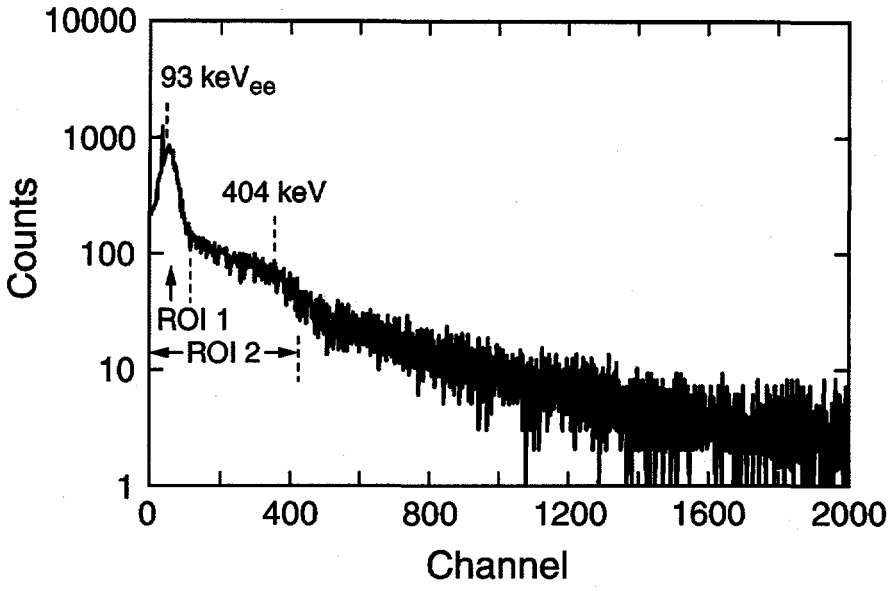

Figure 4-10. Phoswich BC454 Neutron Spectrum Corrected for BGO

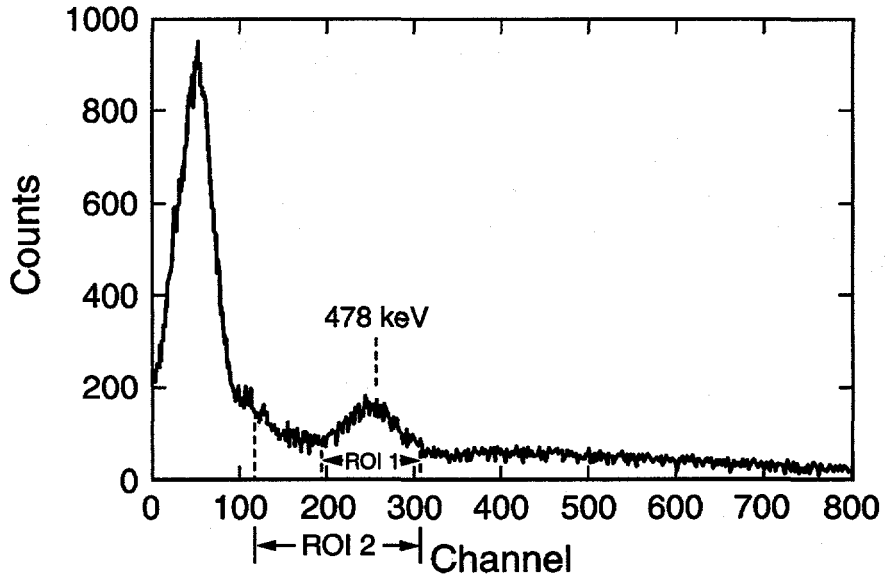

Figure 4-11. Phoswich BGO Neutron Spectrum Corrected for BC454

Table 4-3. Calibration Results for Each Detector/GI Assembly

Parameter	FA17/GI#1	FA20/GI#2	FA21/GI#3	FA18/GI#4
k	1.926	1.820	1.674	1.843
a	1.41366	1.41366	1.41366	1.41366
b	1.58387	1.49670	1.37663	1.51561
c	3.89985	3.68522	3.38959	3.73179
d	0.459627	0.459627	0.459627	0.459627

Table 4-4. Energy Calibrations for Each Detector/GI Assembly

Parameter	FA17/GI#1	FA20/GI#2	FA21/GI#3	FA18/GI#4
BC454				
x (keV)	83.3	58.0	72.7	-13.4
y (keV/ch)	1.067	1.000	1.067	1.143
BGO				
x (keV)	77.2	-148.9	146.0	-99.7
y (keV/ch)	2.293	2.457	2.457	2.457

Examination of Figs. 4-8 through 4-11 leads to the conclusion that the separation procedure works, as evidenced by the expected features in each spectrum (478-keV Compton edge in BC454, 662-keV peak in BGO for ^{137}Cs, 93-keV$_{ee}$ neutron-capture peak in BC454, and 478-keV neutron-capture gamma-ray peak for ^{252}Cf). Also, note that the resolution of the phoswich detector is not as good as the individual detector data, but it is adequate for the discrimination of neutron events.

4.3. NEUTRON DISCRIMINATION

Discrimination of neutron capture events must precede time-correlation analysis. This discrimination is accomplished by applying the measured energy calibration to regions of interest (ROI) in the separated BC454 (corrected I_1) and BGO (corrected I_2) spectra. A program, ANALYZE (see Appendix D), was written to allow this discrimination to be performed by requiring 1) an event only in the 93-keV$_{ee}$ ROI in the

separated BC454 spectrum, or 2) a coincidence between the BC454 and BGO elements, corresponding to the 93-keV$_{ee}$ peak in BC454 and the 478-keV peak in BGO. The ANALYZE program reads in the measured set of energies and times, performs the pulse separation, and filters out events of interest.

Filtering the data based on requiring a response only in the region of the 93-keV$_{ee}$ peak was performed initially. The purpose was to evaluate the benefit of adding BGO to the detector as a means of improving neutron event detection. The ROI used is shown in Fig. 4-10, labeled ROI 1. Figures 4-12 and 4-13 show the result of requiring only an event in the 93-keV$_{ee}$ energy region. We can see from Fig. 4-12 that the 93-keV$_{ee}$ peak appears in the general place expected in the spectrum, but Fig. 4-13 has counts in it that do not correspond to interaction of the 478-keV gamma ray in BGO. The fact that there are counts in Fig. 4-13 that are not due to a 478-keV source implies that there is some contamination in the 93-keV ROI of the BC454 spectrum that does not arise from neutron capture. This is most likely caused by gamma rays that scatter and deposit an amount of energy included in the 93-keV$_{ee}$ ROI for the BC454 spectrum. Time-correlation analysis using only the 93-keV$_{ee}$ peak will include non-neutron events, thereby resulting in a loss of precision from a higher accidental coincidence background. The degree to which this increase represents a problem depends on the neutron peak-to-background.

Alternatively, the neutron-event requirement can be a prompt coincidence between the BC454 and BGO elements. This coincidence is performed by adding another ROI in the analysis program for the 478-keV gamma ray in the BGO separated spectrum. Figure 4-11 shows the ROI used, labeled ROI 1. Figures 4-14 and 4-15

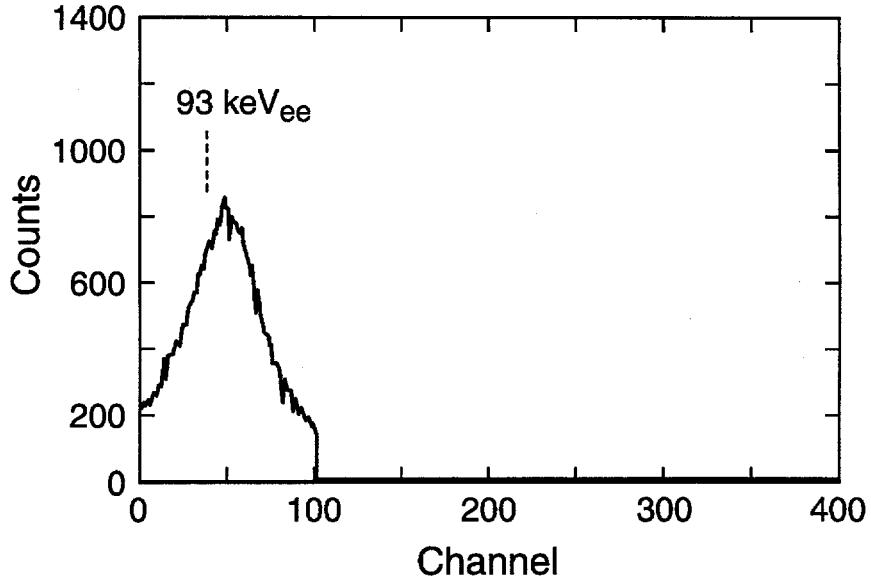

Figure 4-12. BC454 Neutron Discrimination- 93-keV$_{ee}$ ROI Only

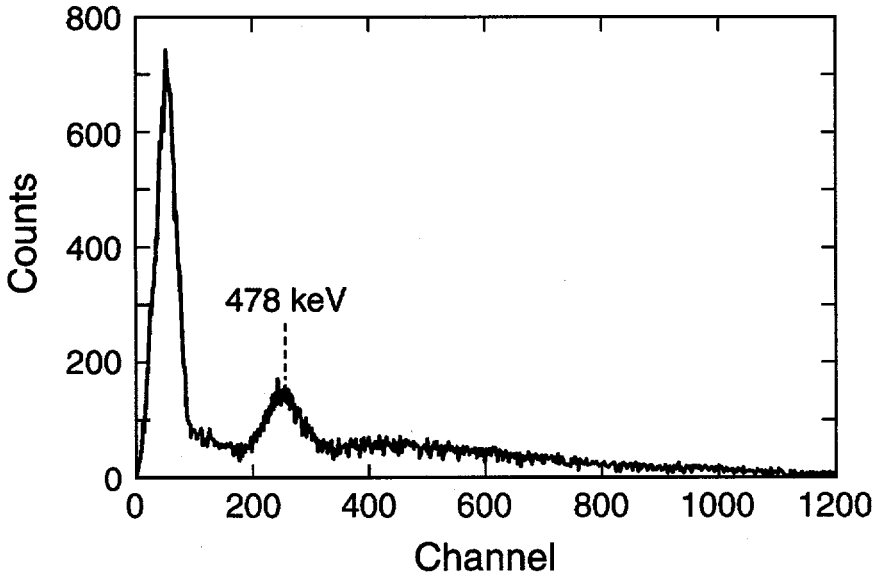

Figure 4-13. BGO Neutron Discrimination- 93-keV$_{ee}$ ROI Only

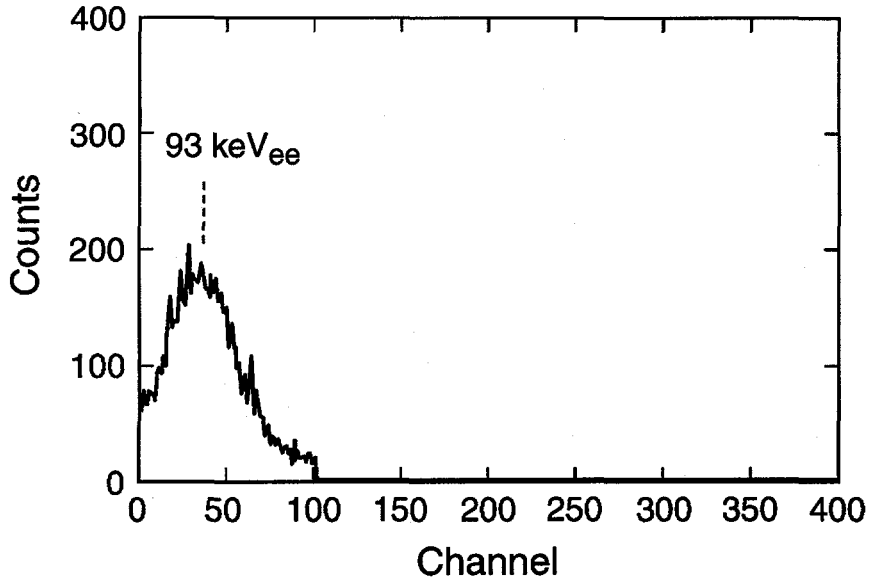

Figure 4-14. BC454 Neutron Discrimination- 93-keV$_{ee}$ + 478-keV ROI

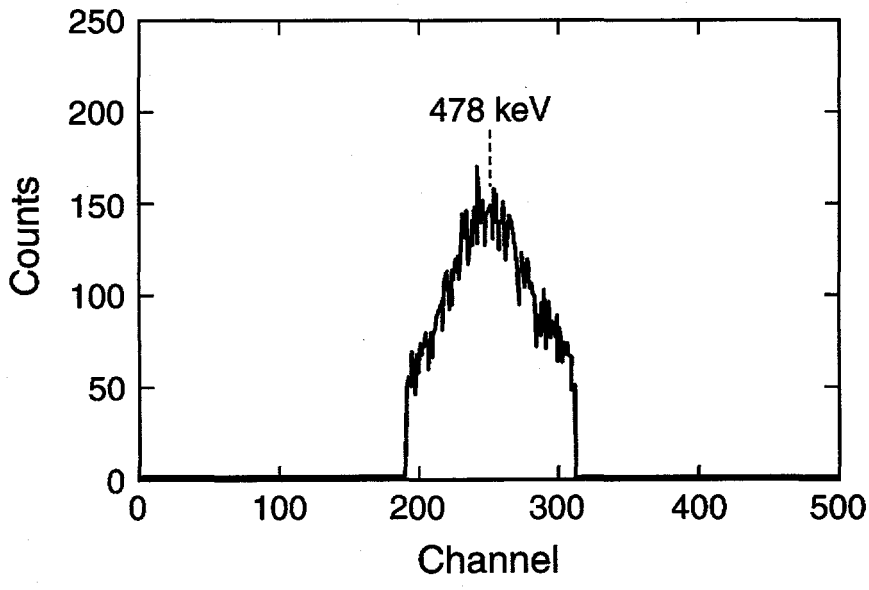

Figure 4-15. BGO Neutron Discrimination- 93-keV$_{ee}$ + 478-keV ROI

present the results of this filter. The 93-keV$_{ee}$ peak shown in Fig. 4-14 appears very similar in character to that shown in Fig. 4-12 except that the intensity has decreased. This decrease is because only events in the 93-keV$_{ee}$ window that coincided with those in the 478-keV window in the BGO were selected. The peak in Fig. 4-15 corresponds to the 478-keV peak and is in the expected location based on the energy calibration.

The distribution of all energies in the BC454 and BGO elements for the ^{252}Cf measurement is shown in Fig. 4-16. All data are plotted in this case (no filter is applied) and the concentration of events at low pulse heights corresponds to 93-keV$_{ee}$ captures where the 478-keV gamma ray escapes added to non-neutron events. The concentration of events in the region around channel 250 in the BGO and channel 50 in the BC454 corresponds to the coincidence between the 93-keV$_{ee}$ capture and 478-keV peaks. Events corresponding to the Compton scattering of the 478-keV gamma ray in the BC454 and subsequent detection by the BGO are located in the exponentially-decreasing area (lower channel number in BGO and higher channel number in BC45) from the 93-keV$_{ee}$ and 478-keV coincidence region. Expansion of the ROIs to include the Compton scatter portion of the 478-keV response in the BC454 and corresponding decrease in deposited energy in the BGO is shown in Figs. 4-17 and 4-18. The ROIs used are those shown in Figs. 4-10 and 4-11 and labeled as ROI 2. We see from Fig. 4-17 that the number of counts in the spectrum has increased and the overall shape is consistent with that shown in Fig. 1-5. Figure 4-18 shows the 478-keV spectrum in BGO, with the photopeak and the Compton continuum clearly visible. Fast-neutron scatters in the BC454 appear as a tail from the 93-keV$_{ee}$-only detection region.

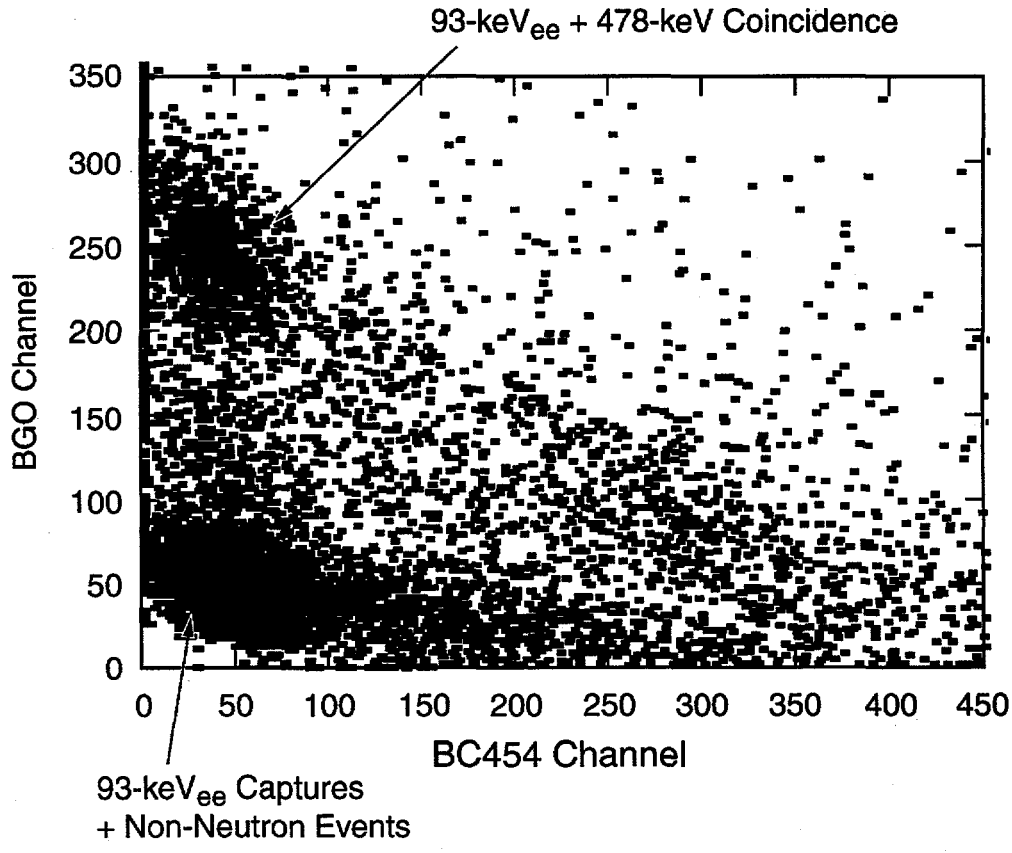

Figure 4-16. BC454 vs. BGO Counts for ^{252}Cf Source

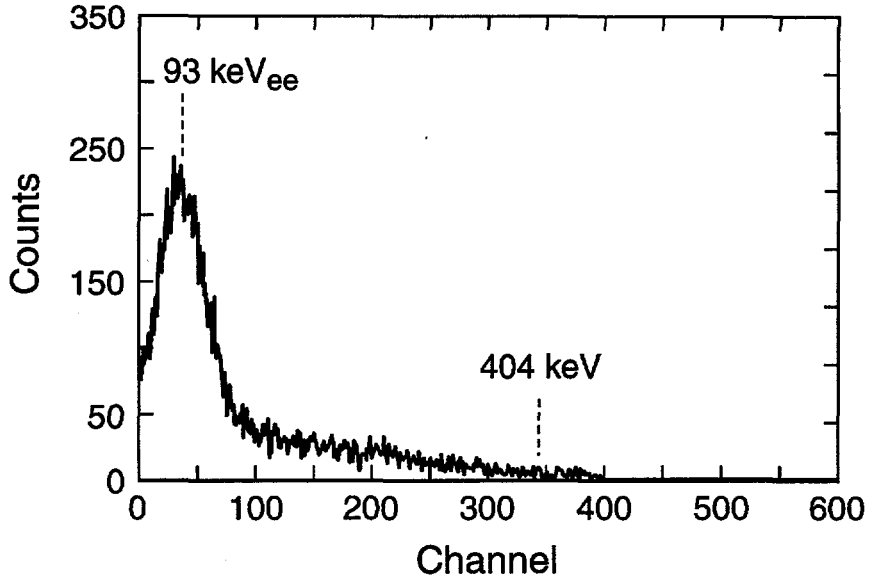

Figure 4-17. BC454 Component of Neutron Discrimination- Expanded Window

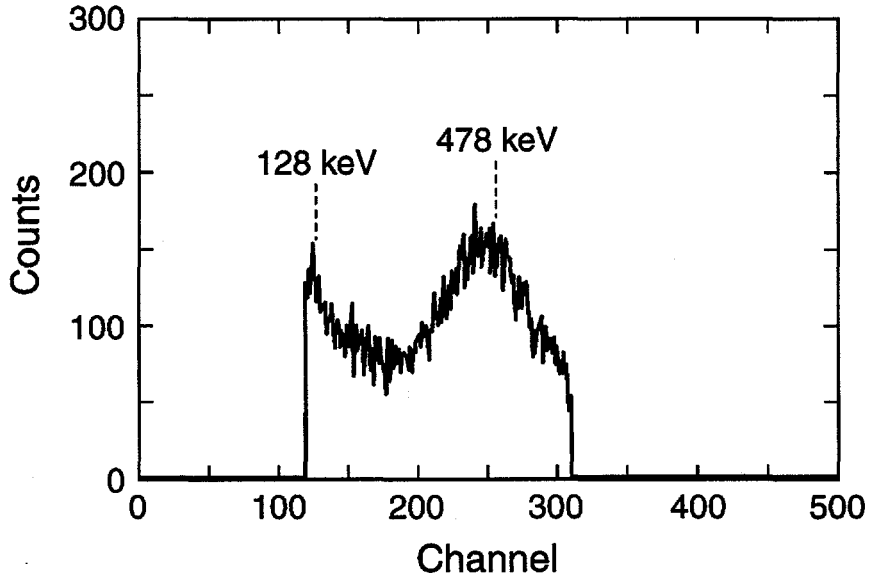

Figure 4-18. BGO Component of Neutron Discrimination- Expanded Window

Evaluation of the relative performance of these neutron discrimination methods is explored in Chapter 5, Results. The key factors will be the trade-off between including non-neutron events and therefore creating an increase in the noncorrelated background (offsetting some of the gain from the short die-away time) versus not including all of the neutron events, thereby decreasing the efficiency.

Another method of neutron discrimination is to require a proton recoil to occur before the capture happens. This method is the basis for the use of BC454 as a neutron spectrometer. When AmLi is used as a source of interrogation neutrons (a good choice in the case of uranium measurements), the proton-recoil requirement can be used to filter out the unwanted AmLi neutron captures. This method of discrimination is possible because the average energy of AmLi is only 0.3 MeV,[43] below the threshold for light production in the BC454. Filtering the data in this way involves accepting only those capture events that are preceded by any other pulse within a few microseconds. Time-correlation analysis is then performed on the resulting event stream. In principle, this method would greatly reduce the accidental background associated with active interrogation of uranium as compared to thermal-neutron counting techniques, where there is no mechanism for distinguishing between the AmLi interrogation source and the induced fission neutrons from ^{235}U.

4.4. TIME-CORRELATION ANALYSIS

Time-correlation analysis is performed on the neutron-capture filtered data. The TIMEPREP program (see Appendix D) reads in the output from the ANALYZE program and writes out only the associated time tags. The MULTDIST program (see Appendix D)

is then used to sort through the filtered event stream and to construct the $(R+A)$ and A multiplicity distributions. Singles and doubles are determined in the standard way from the measured distributions (see Eqs. 1-7 and 1-8.) Triples were not measured because of the relatively low detection efficiency in the proof-of-principle experimental configuration.

For every event there is a corresponding time tag in addition to the energy information from the G_1 and G_2 integration channels. This time tag is a 32-bit word (rollovers are accounted for in the data acquisition software), giving up to 1073 s (2^{32} clock ticks times 250 ns/tick) of counting time per run. The filtered data preserves the time tags along with the corrected I_1 and I_2 channel values, and the MULTDIST program sorts through them by looking for events that are within the chosen predelay and coincidence gate length. Two passes are made through the data: the first one is equivalent to the pulse-triggered accumulators in the shift register (R+A scalers), and the second is equivalent to the randomly triggered accumulators (A scalers). The result of the MULTDIST program is the formation of the $(R+A)$ and (A) multiplicity distributions for the measured source.

Although the form of the point equations does not need to be altered for use with the BC454/BGO phoswich detector, the definition of some of the terms has to be modified. All terms have the same meaning as given in Eqs. 1-4 through 1-6 except:

$$\varepsilon = p_c p_\gamma \tag{4-19}$$

$$\alpha = \alpha + \Delta_\alpha, \tag{4-20}$$

where p_c is the probability for neutron capture in the BC454 and p_γ is the probability that the 478-keV neutron capture gamma ray will be detected in the BGO. If only the 93-keV_{ee} peak is used, $p_\gamma = 1$. The term Δ_α takes into account any non-neutron events that are selected as part of the filtering process, and it is negligible unless only 93-keV_{ee} ROI for the BC454 is used (no BC454/BGO coincidence requirement).

4.5. DETECTOR SIMULATION

Response of the detector to both gamma rays and neutrons was simulated to aid in the evaluation of the experimental hardware and analysis techniques. Calculations were performed with the Los Alamos radiation transport code MCNP, in which the neutron-capture probability in the BC454, the 478-keV capture gamma ray detection probability in the BGO, and the general shape of the BC454 and BGO response to gamma rays were made. In addition, estimates of the neutron die-away time were made for the 4-detector array in a variety of configurations.

Estimates of the ^{137}Cs response were made with the following geometry: a single detector (BC454/BGO) with a ^{137}Cs source located 5 cm from the long axis of the detector. Results of the calculation are given in Figs. 4-19 and 4-20. The measured BC454 Compton spectrum (see Fig. 4-8) compares in its general shape quite well with the calculation, whereas the measured BGO spectrum (see Fig. 4-9) is somewhat degraded relative to the calculated one. A partial explanation for this is the lack of any light transport in MCNP, a factor that is important in the phoswich response.

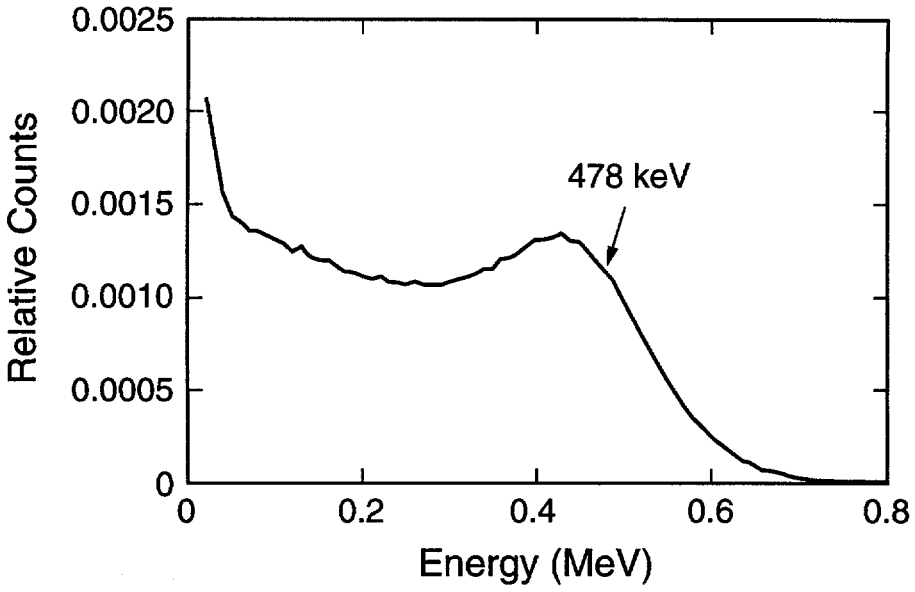

Figure 4-19. Detector Response Simulation of a ^{137}Cs Source- BC454 Component

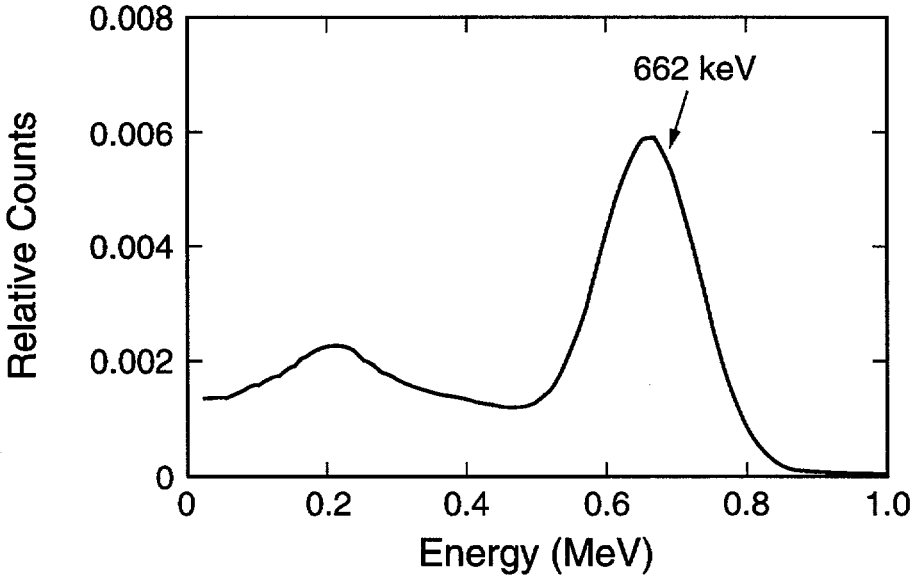

Figure 4-20. Detector Response Simulation of a ^{137}Cs Source- BGO component

Additionally, the calculated spectrum does not include any imperfection in the pulse-separation model, which contributes particularly at the lower end of the spectrum.

Simulation of the detector response for the gamma-ray portion arising from neutron capture in the BC454 was done by creating an internal volume source (478-keV gamma rays) that was homogeneously distributed within the BC454, and tallies made in the BGO so that the detection probability of the 478-keV gamma ray could be estimated as well as the probability of escape without interaction. Figures 4-21 and 4-22 show the results. The calculation was done with and without a resolution function (25% for BC454 and 30% for BGO). The primary result of this calculation is that with 0.4 cm of BGO, 49% of the 478-keV photons produced from neutron capture in the BC454 escape without interaction, while 23% deposit all of their energy and end up in the photopeak. Increasing the thickness of the BGO significantly enhances detection probability of the 478-keV gamma ray. If the BGO is 1 cm thick, only 27% of the 478-keV gamma rays escape the detector without interaction and 44% end up in the photopeak. Similarly, 2 cm of BGO increases the photopeak to 59% of the 478-keV gamma rays, with only 6% escaping without interaction.

The neutron capture response of the 4-detector array was also simulated with MCNP in a variety of configurations. The geometry is shown in Fig. 4-23. A ^{252}Cf source was located within the sample cavity (see Fig. 3-4) and symmetrically placed with respect to all four detectors. Tallies of the neutron-capture probability as a function of time were made so that the array efficiency and die-away time τ could be estimated. Table 4-5 presents the results of the calculations.

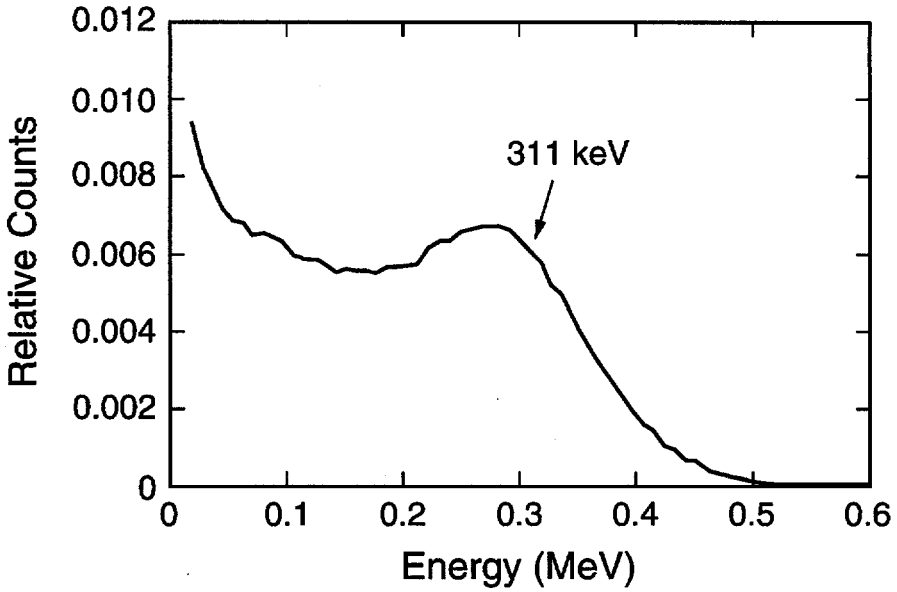

Figure 4-21. Simulated BC454 Response to an Internal 478-keV Source

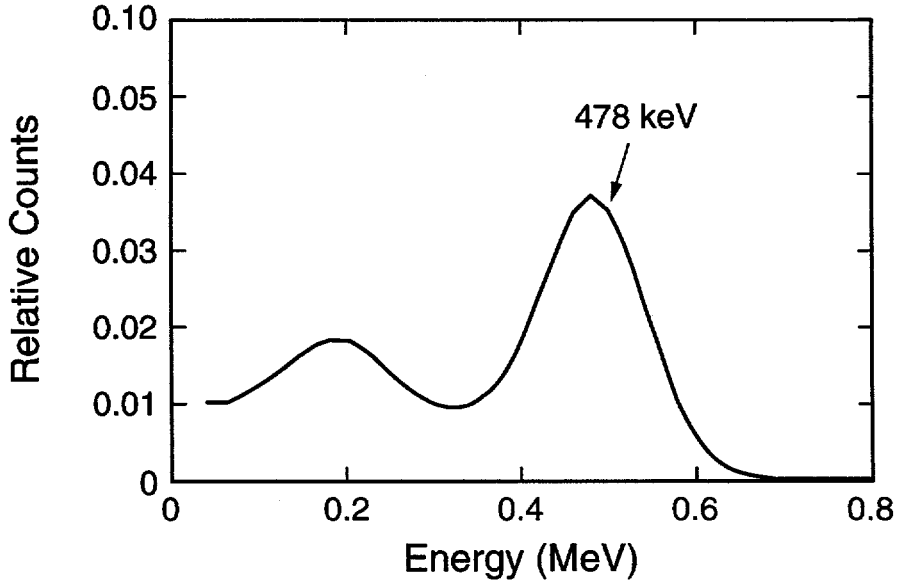

Figure 4-22. Simulated BGO Response to an Internal 478-keV Source

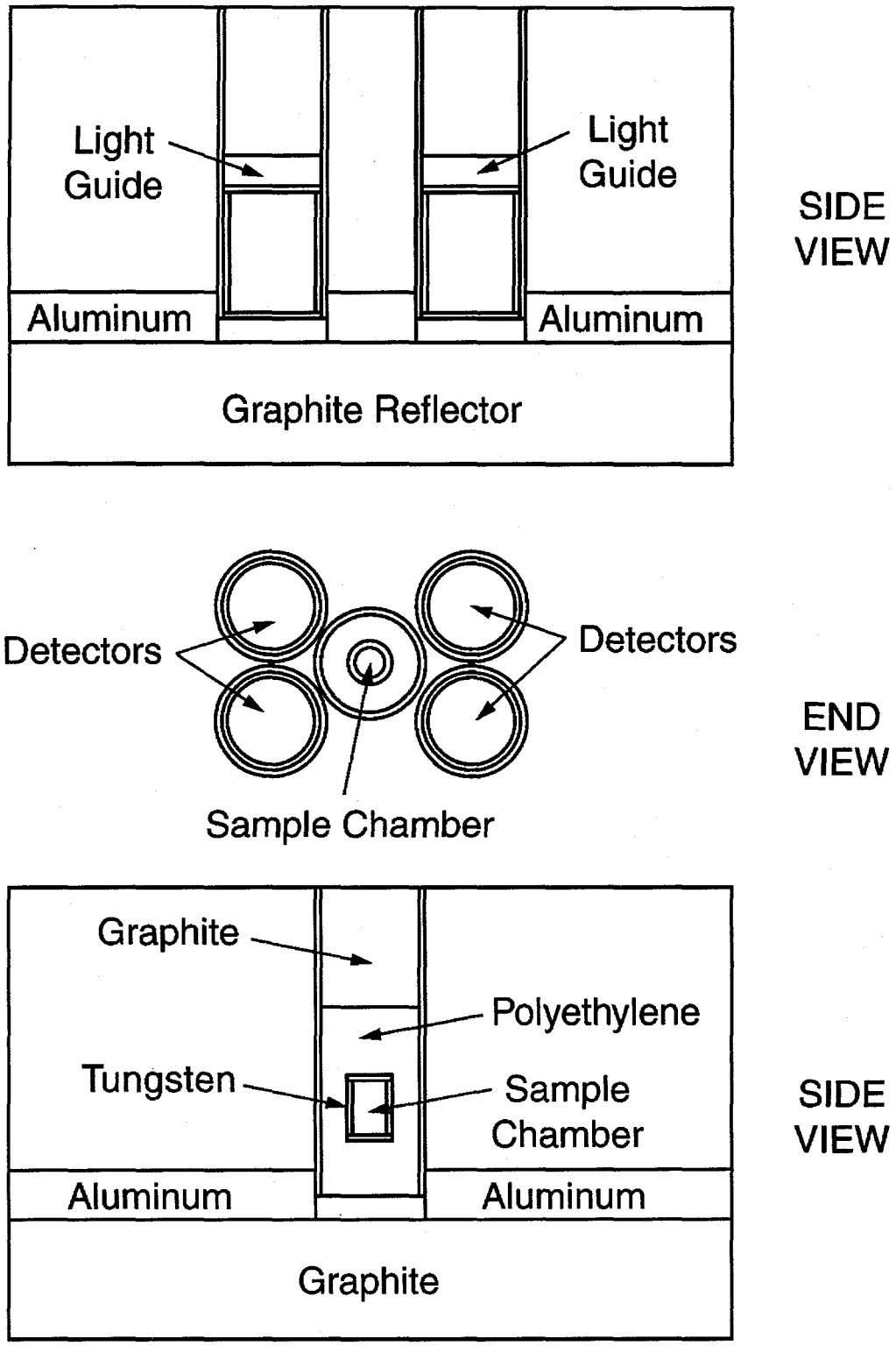

Figure 4-23. MCNP Geometry for the 4-Detector Array

Table 4-5. MCNP Results for the 4-Detector Array

Sample Chamber	Graphite Reflector	Capture probability	τ (μs)
yes	yes	0.1043	12.4
yes	no	0.0855	11.8
no polyethylene	yes	0.0429	2.8
W only	no	0.0378	2.4

Four different cases were simulated: 1) full sample chamber (polyethylene, tungsten, and graphite plug as shown in Fig. 3-4) with reflecting graphite block (10-cm thick by 30-cm square) located at the detector end of the assembly, 2) full sample chamber without graphite block, 3) sample chamber with polyethylene removed and graphite block in place, and 4) sample chamber with graphite plug and polyethylene removed and graphite block removed also. We see from Table 4-5 that the efficiency and die-away time are related, with a higher efficiency obtained at the expense of a longer die-away time. This is because there is not enough detector material present to moderate the neutron source by itself. When scattering and moderation are added, the neutron capture probability increases, but so does the average time-to-capture. If, on the other hand, additional detector material is added, efficiency can be increased and the die-away time decreased by reducing the need to provide external moderation (see Table 1-4, for example).

A general problem with simulation of the detector response is that no single code exists that will adequately handle all of the aspects of the BC454/BGO phoswich response. Traditional scintillator codes, such as KSUEFF,[44] do not contain low-energy neutron interaction physics, including neutron capture, because they were designed for simulation of light production by a process which has a neutron energy threshold of about

0.5 MeV. These codes are also restricted in the geometry that can be accommodated. Other radiation transport codes such as MCNP have general geometry packages, but no light-production interaction physics is incorporated in them. One can, however, build up the response in a piece-wise fashion.

The proton-recoil response of BC454 to fast neutrons (courtesy of Roger Byrd using the KSUEFF code)[45] was added to the MCNP gamma-ray simulations and compared to measured data. The KSUF calculations simulated the generic response to a field of monoenergetic neutrons, whose energy ranged from 0.4 MeV to 12.8 MeV in 0.2 MeV steps. A Watt fission shape for ^{252}Cf was then used to weight the results, thus obtaining an estimate the BC454 response for fast neutron interaction from ^{252}Cf.

Results of the calculations made with the KSUEFF code were combined with the MCNP-simulated spectra in Figs. 4-21 and 4-22 (gamma-ray contribution to BC454 and BGO arising from neutron capture in BC454) and compared to the measured ^{252}Cf spectrum shown in Fig. 2-20. The resulting spectra are shown in Fig. 4-24 , where the difference between the calculated and measured spectra is shown as the 93-keV capture peak (curve 5) and ^{252}Cf source gamma-ray contribution (curve 4). The neutron-capture spectrum was assembled by combining the 93-keV$_{ee}$ response (curve 5) with the simulation results for the 478-keV gamma-ray response in the BC454 and the BGO (curves 3 and 6). Note the similarity in shape between the estimated neutron-capture signature (enlarged portion of Fig. 4-24) and the measured neutron-capture spectrum of Fig. 2-20.

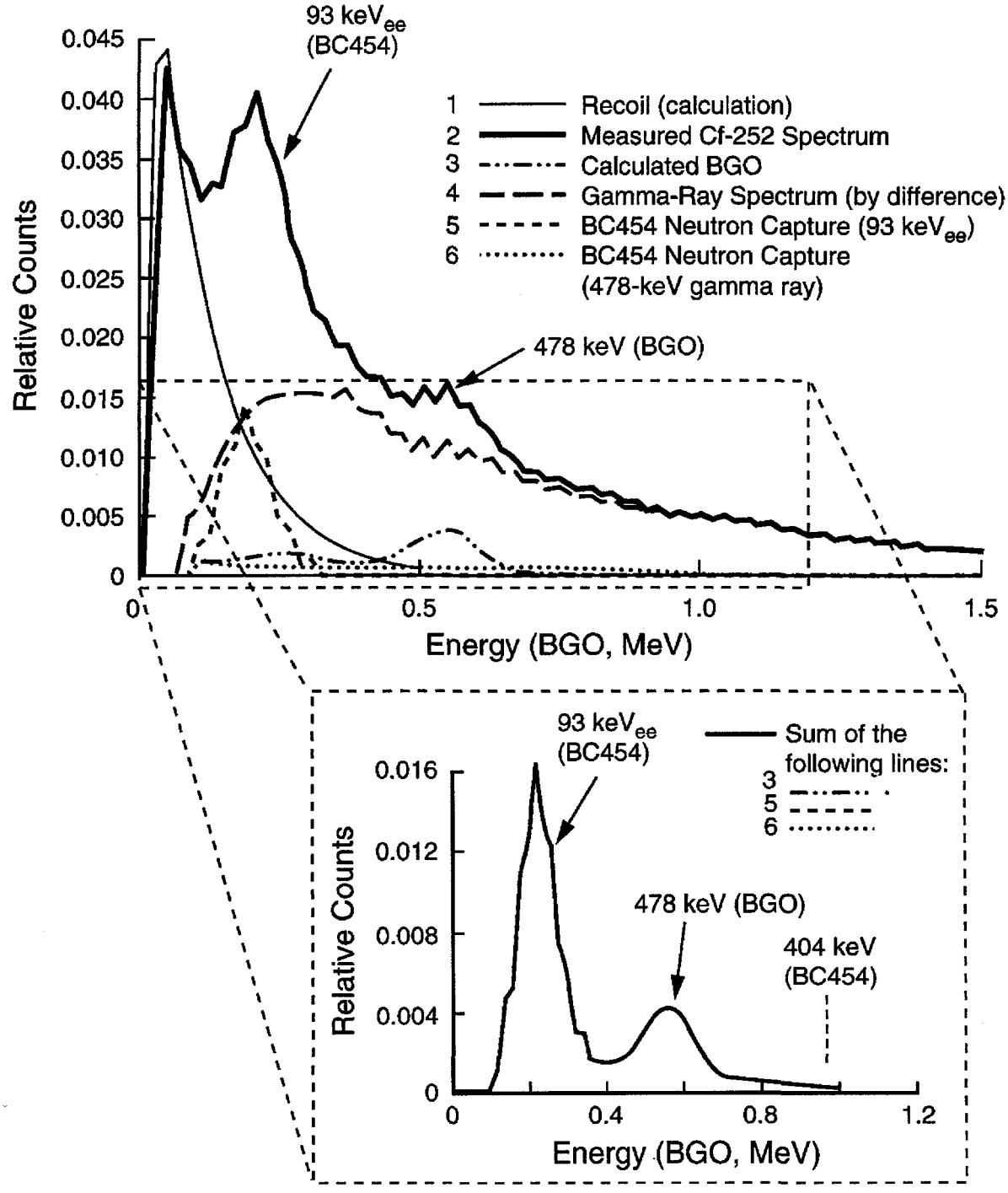

Figure 4-24. Calculated ^{252}Cf Spectrum- BC454/BGO Phoswich

In this chapter the pulse-separation algorithm was developed and demonstrated, enabling the data stream to be filtered for only neutron events. Discrimination of neutron events was performed using the following criteria: 1) 93-keV$_{ee}$ region only, and 2) a coincidence requirement between the BC454 and BGO elements (93-keV$_{ee}$ region plus 478-keV region). Post-processing of the filtered event stream was described and included the computerized shift register, calculation of the $R + A$ and A multiplicity distributions, and conversion of the distributions to singles and doubles, and triples. In addition, simulations of the detector response to both gamma rays and neutrons were carried out. Chapter 5, Results, combines the experimental data with the analyses and simulations to demonstrate the quantitative measurement proof-of-principle for the BC454/BGO phoswich detector array.

5. RESULTS

5.1. INTRODUCTION

In this chapter, the experimental data from Chapter 3 is combined with analyses and simulations developed in Chapter 4 to provide proof-of-principle results for the detection concept. Results of applying the time-correlation analysis (singles and doubles) are given for the different neutron discrimination methods. Consistency between the experimental data and simulation results is shown and extensions to other detector designs are explored. The potential quantitative assay capability of the BC454/BGO phoswich detector array is demonstrated in this way.

5.2. CALIBRATION AND PROOF-OF-PRINCIPLE

Demonstration of proof-of-principle of the quantitative nature of the BC454/BGO phoswich detector array is accomplished in the following manner:

- measure efficiency and die-away time of the detector array with ^{252}Cf sources,
- compare measured efficiency and die-away time with MCNP results,
- compare measured results with the point model predictions,
- estimate yield of AmLi source and compare with known value,
- compute f_d, and

- measure a known plutonium sample using measured efficiency and gate fractions.

Initially, the neutron discrimination method used was to require a coincidence between the BC454 (93-keV$_{ee}$ peak) and the BGO (478-keV peak), using the ROI-1 set (see Figs. 4-10 and 4-11). Evaluation of the other neutron discrimination techniques is reported in the next section.

Table 5-1 presents the yields, observed net rates (singles and doubles), and estimated precision (obtained from counting statistics) for the ^{252}Cf sources measured. These sources are part of a calibrated series whose activities are known with approximately 2% accuracy. The neutron detection efficiency, ε, is defined as

$$\varepsilon = \frac{S}{\text{Yield}}, \tag{5-1}$$

where the yield corresponds to the total neutron output (n/s) on the measurement date and is given in Table 5-1. Table 5-2 gives the calculated neutron detection efficiencies (ε) for the data presented in Table 5-1, using Eq. 5-1. We see from Table 5-2 that the measured neutron detection efficiencies are self-consistent, with an average value of 0.0274.

Estimates of the die-away time (τ) are obtained by forming a Rossi-Alpha arrival-time distribution of the filtered time-tag data and then fitting it with an exponential. The Rossi-Alpha distribution is obtained by choosing an arbitrary event as $t = 0$, then histogramming the arrival times up to a predetermined time (in this case 1024 μs). Results of fitting an exponential to the data corresponding to the runs in Table 5-1 are also presented in Table 5-2, with the measured distribution for CR-8 and corresponding

fit shown in Fig 5-1. The agreement of the independent measurements is relatively good, with the average die-away time measured as 11.4 μs.

Table 5-1. ^{252}Cf Measurement Results- 4-Detector Array

Source ID	Yield (n/s)[a]	Gross Rate	$S \pm \sigma$	$D \pm \sigma$
CR-7	14995	4678	420 ± 2	9.2 ± 0.4
CR-8	37792	8160	1011 ± 5	30.6 ± 1.3

[a]Reference date- 1/15/97

Table 5-2. Measured Detection Parameters- 4-Detector Array

Source ID	ε	τ (μs)	p_γ
CR-7	0.0280	12.0	0.327
CR-8	0.0268	10.8	0.313
Average	0.0274	11.4	0.320
MCNP estimate	0.0257	11.8	0.301

Comparison of the measured die-away times with those estimated using the MCNP model is straightforward. The calculated value of 11.8 μs (see Table 4-5) is in good agreement with the average measured value of 11.4 μs, with the ratio of average measured-to-calculated die-away time being 0.97. Comparison of the measured efficiency to that estimated by simulation is not as direct, because the simulation results are given as neutron capture probabilities whereas the measured efficiencies include the probability of detection of the 478-keV neutron-capture gamma ray. As such, combination of the MCNP results and measured values defines the 478-keV detection probability,

$$p_\gamma = \frac{\varepsilon \text{ (measured)}}{\varepsilon \text{ (MCNP)}}. \tag{5-2}$$

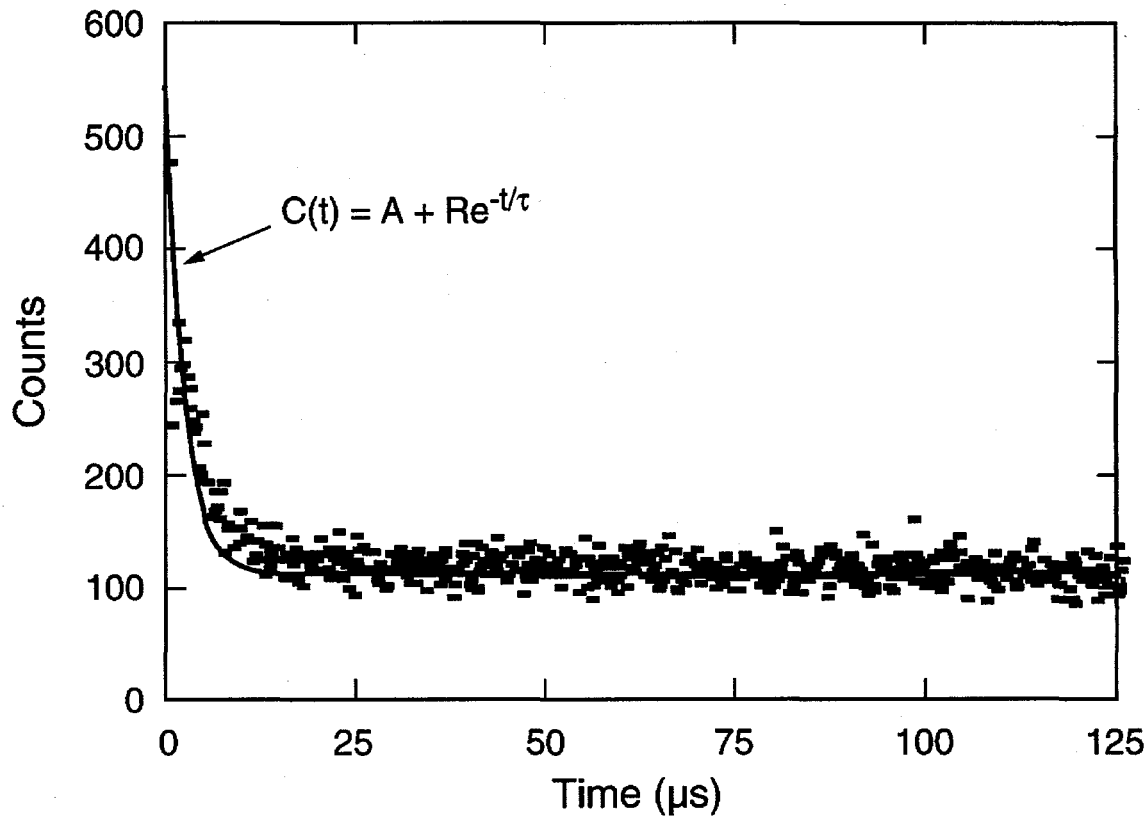

Figure 5-1. Rossi-Alpha Distribution for ^{252}Cf Source with Exponential Fit

Measured values of p_γ are also included in Table 5-2. The value of p_γ is obtained from MCNP (for a volumetric 478-keV source within the BC454), by tallying the probability of detection of the 478-keV gamma ray within the energy range corresponding to the ROI used multiplied by the neutron-capture reaction's branching ratio to the first excited state of ^{7}Li (0.94). This result is given in Table 5-2 as well. Combining the MCNP estimates for the neutron capture probability and 478-keV detection probability gives the estimate for the absolute detection efficiency as 0.0257. This agrees well with the measured value of 0.0274, with the ratio of measured-to-calculated efficiency being 1.066.

Validation of the point-model equations as applied to the BC454/BGO phoswich detector can be accomplished by calculating the doubles from the measured singles and the estimated gate fraction (based on measured die-away time) as

$$D = \frac{S\varepsilon f_d \nu_{s2}}{2\nu_{s1}}, \tag{5-3}$$

using the nuclear data for ^{252}Cf from Table 1-2 and Eqs. 1-4 and 1-5. Equation 5-3 assumes that $M = 1$ and $\alpha = 0$. The doubles gate fraction is estimated by a assuming single exponential die-away time

$$f_d = e^{-p/\tau}(1 - e^{-g/\tau}), \tag{5-4}$$

where p is the predelay and g is the coincidence gate length.

Table 5-3 shows the results for the comparison of measured and estimated doubles based on the data given in Table 5-1. As can be seen from Table 5-3, the measured

values agree well in the case of CR-8 and not as well for CR-7, with the overall ratio of measured-to-estimated doubles being 0.82.

Table 5-3. Doubles Comparison- 4-Detector Array

Source ID	Measured *D*	Estimated *D*	Measured/Estimated
CR-7	9.2	13.4	0.69
CR-8	30.6	32.3	0.95
Average			0.82

Table 5-4 presents the results of the AmLi source measurements, where we see that the ratio of the singles count rate relative to CR-8 is not the expected value. A partial reason for this discrepancy is the energy dependence of the neutron capture probability. The thermal neutron counter used to determine the yield ratios has a more uniform efficiency response as a function of source energy than does the 4-detector phoswich array. Consequently, a direct comparison between results obtained using a thermal neutron counter is not possible. An estimate of the neutron capture probability for a 0.3-MeV source (the average neutron energy for AmLi) was made with MCNP and yielded a result of 0.192, compared with 0.0855 for ^{252}Cf. The ratio of these values, 2.25, represents a correction factor for the measured AmLi-to-CR-8 ratio. Applying this correction results in better agreement between the expected and measured yield ratios, but there is still a factor of two difference. There are no statistically significant doubles for MRC100, while the doubles observed for MRC98 is within 3.6 σ. This absence of correlated counts is consistent with the random nature of AmLi neutron emission.

Table 5-4. Results for AmLi Sources

Source ID	Yield relative to CR-8[a]	$S \pm \sigma$	$D \pm \sigma$	Corrected S(AmLi)/ S(CR-8)
MRC98	0.230	1144 ± 4	2.9 ± 0.8	0.50
MRC100	2.04	9376 ± 26	11 ± 14	4.12

[a]Based on measurement in thermal neutron counter.

Before the plutonium sample mass can be estimated, the doubles gate fraction f_d must be determined. This fraction can be calculated from the measured ^{252}Cf data given in Table 5-1 in combination with Eqs. 5-3. Substituting, we arrive at

$$f_d = \frac{2\nu_{s1}}{\varepsilon\nu_{s2}}\left(\frac{D}{S}\right) \tag{5-5}$$

Experimental values can be compared with analytical ones based on a Eq. 5-4. For the data presented in Table 5-1, p = 0 μs and g = 15 μs. Substituting these values and the measured die-away time of 11.4 μs into Eqs. 5-4, we obtain f_d = 0.732. Table 5-5 gives the measured results using the data from Table 5-1 and Eqs. 5-4 and 5-5.

Table 5-5. Doubles Gate Fraction- 4-Detector Array

Source ID	f_d^a
CR-7	0.502
CR-8	0.694
Average	0.598
Eqs. 5-5	0.732

[a]Efficiency used was average value from Table 5-2 (ε = 0.0274).

A small plutonium sample was also measured to demonstrate the potential of the BC454/BGO detector to assay special nuclear material. The mass of the sample was quite small, so that the assumption M = 1 is valid. In this case, the point-model equations

simplify and only the singles and doubles are required to estimate the sample mass. Table 5-6 contains the tag values for the ^{240}Pu-effective mass and α, as well as the measured singles and doubles count rates.

Table 5-6. Sample and Measurement Data- Small Plutonium Sample

Sample ID	α	^{240}Pu-eff	$S \pm \sigma$	$D \pm \sigma$
FZC158 (Oxide)	0.14	0.7054	30.7 ± 0.2	0.40 ± 0.04

Table 5-7 contains the estimates for ^{240}Pu-effective mass and α for the small plutonium sample.

Table 5-7. Plutonium Assay Results- 4-Detector Array

Sample ID	Tag mass (g)	Assay Mass (g)	α
FZC158	0.70	0.98 ± 0.10	0.11

We see from Table 5-7 that the agreement of measured and known sample mass is somewhat high, but within the statistics of the measurement. The value of α agrees fairly well with the known value.

5.3. EVALUATION OF NEUTRON DISCRIMINATION FILTERS

So far, only the use of the BC454/BGO coincidence with the ROI-1 set for neutron discrimination has been examined. In this section, the other filtering methods described in Chapter 4 are evaluated. The other two discrimination methods were 1) use of only the 93-keV$_{ee}$ window (ROI-1) in the BC454, and 2) requiring a BC454/BGO coincidence (93 keV$_{ee}$ and 478 keV respectively) with the ROI-2 set (see Figs. 4-10 and

4-11). Changing the criteria for identification of a neutron event affects the measured detection efficiency and gate fractions. Therefore, evaluation of these other filtering techniques will require recalculation of these parameters. Table 5-8 contains the appropriate detection efficiencies and doubles gate fractions for the other neutron filtering techniques.

Table 5-8. Detection Efficiencies and Gate Fractions- 4-Detector Array

	93-keV$_{ee}$ window[a]		93-keV$_{ee}$ + 478-keV window (wide)[b]	
Source ID	ε	f_d	ε	f_d
CR-7	0.148	0.440	0.063	0.461
CR-8	0.102	0.632	0.065	0.632
Average	0.125	0.536	0.064	0.547

[a]ROI(1) from Fig. 4-10.
[B]ROI(2) from Figs. 4-10 and 4-11.

We see from Table 5-8 that the measured detection efficiency is greater in both instances as compared with the neutron filter method based on the ROI-1 set. In fact, the measured efficiencies are greater than estimated by the MCNP simulation. In the case of the 93-keV$_{ee}$-only ROI, the measured efficiency is greater than the total neutron-capture probability as estimated by MCNP. This increase is because the ROI used for the 93-keV$_{ee}$ events in the BC454 contains additional, non-capture data arising from gamma-ray interactions and proton recoils in which the energy deposited happens to fall within the ROI. For the 93-keV$_{ee}$ plus 478-keV ROI-2 set, the 478-keV detection probability times the branching ratio of 0.94 is estimated by MCNP at 0.42, leading to an efficiency of 0.036. This value is quite a bit lower than the measured on of 0.064, indicating that this

ROI set also contains non-neutron-capture events. One mechanism contributing to excess events could be the 180 degree Compton scatter of the 478-keV gamma-ray occurring near the interface of the BC454 and BGO detector elements. Under this circumstance, it is possible to deposit energy in both detector elements within the expanded ROI set in a manner not considered by the MCNP model.

For the 93-keV$_{ee}$-only ROI data, $p_\gamma = 1$ and the apparent, or effective, increase in the (alpha,n) rate is given by

$$\Delta_\alpha = 1 - \frac{\varepsilon\ (\text{measured})}{\varepsilon\ (\text{MCNP})}. \tag{5-6}$$

Note that this increase will cause a change in the point equations because the $\alpha = 0$ condition for ^{252}Cf no longer holds. This change just affects the equation for singles because the only way α contibutes to doubles and triples is through induced fission, and the non-multiplying condition, $M = 1$, is still valid. The modified point equation for singles then is

$$S = mF\varepsilon\nu_{s1}\left(1 + \Delta_\alpha\right). \tag{5-7}$$

Changing the efficiency also alters the values obtained for the doubles gate fraction. Table 5-9 presents the corrected efficiency and gate fraction results for the 93-keV$_{ee}$ window filter (note that the MCNP efficiency has been modified to reflect the average measured value from the previous section, 0.0274)

Table 5-9. Detection Efficiencies and Gate Fractions- 93-keV$_{ee}$ Window

Source ID	ε	f_d	Δ_α
CR-7	0.090	1.19	0.65
CR-8	0.090	0.814	0.23

The results for the alternative neutron discrimination methods are quite inconsistent and lead to the conclusion that the narrow ROI-1 set is the best at identifying neutron events.

5.4. EXTENSION TO LARGE-VOLUME DETECTOR

An improvement to the existing 4-detector array would be the addition of more detectors to increase the overall efficiency. Because of the good agreement between experimental results for both efficiency and die-away time, at least for the 93-keV$_{ee}$ plus 478-keV ROI-1 set, simulations can be used as an aid in the forecasting of expected performance when adding detectors to the array or in producing a new design. The current data-acquisition system is capable of operating up to 10 detectors simultaneously, and a simulation study was conducted to estimate the neutron-capture efficiency and die-away time for optimum use of the existing detector hardware.

Calculations were made for two types of cylindrical detectors: 1) the 7.2-cm diameter by 10-cm length configuration (ANDAS) and 2) a 7.6-cm diameter by 30-cm length configuration, which has recently been acquired for testing. In each case, the detectors (in a 5-position or 6-position array) surround a 20-cm diameter by 25-cm high sample cavity. Endcaps of graphite are used to help reflect neutrons that might otherwise be lost back toward the detectors. A variety of materials was placed between the detectors to help evaluate the trade-off between efficiency gain and increasing the die-away time. The shorter detectors were stacked two high so that both configurations would have about the same solid angle with respect to the sample cavity. Figure 5-2 shows a schematic of the detector arrangement.

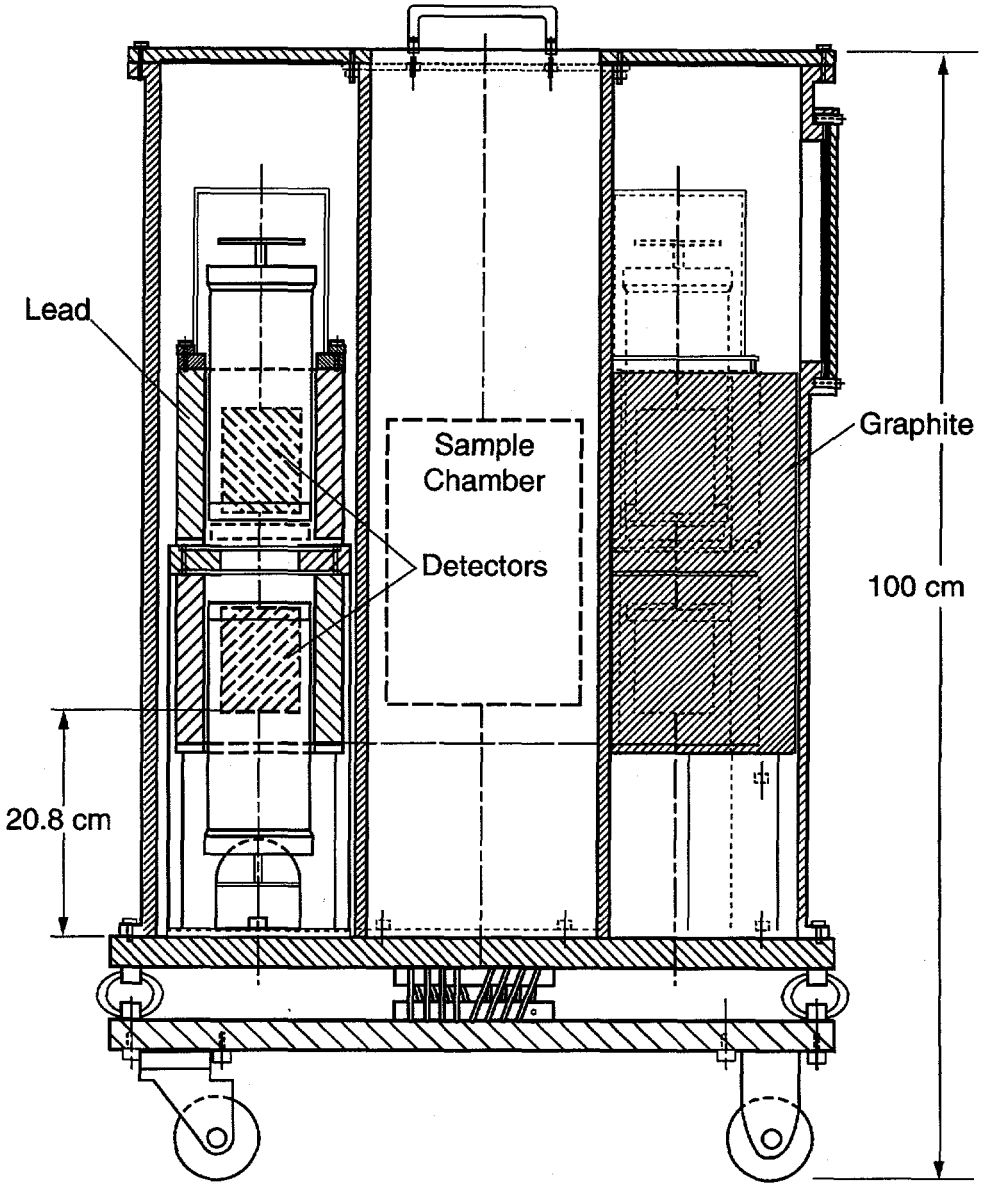

Figure 5-2. Schematic of the 5-Position Array

In addition to the cylindrical detector configuration, an annular one was also simulated. This type of geometry more effectively uses the detector material relative to the cylindrical designs and can achieve a very high neutron-capture probability. Results of the calculational study are presented in Table 5-10, where the detection efficiency is given as the neutron-capture probability times the 478-keV branching ratio of 0.94. Die-away times were calculated by binning the capture tally in time and computing the average capture-weighted time. Efficiencies as high as 20% are possible for the 30-cm length arrangement, with a corresponding die-away time of 7 μs. In the case of the annular configuration, an efficiency of 47% and a die-away time of 4 μs is possible. Both of these cases represent an advancement in assay performance over existing TNCC designs.

Figures 5-3 and 5-4 compare the simulated FNCC designs with the TNCC based on the MCNP results and FOM calculations of the predicted assay variance. In Fig. 5-3, the estimated detection efficiencies are plotted as a function of the corresponding die-away times. The line represents the combination of efficiency and die-away time that equals TNCC assay variance for a 500g plutonium sample, with $M = 1.05$ and $\alpha > 5$. Figure 5-4 translates selected results from Fig. 5-3 into the relative count time decrease as a function of the efficiency increase relative to the line of TNCC-equivalent performance. The potential for improvement over existing TNCC technology is clearly seen.

Table 5-10. Neutron Capture Probabilities and Die-Away Times

Detector configuration[a]	Inter-detector material	Detection efficiency (ε)	Die-away time (μs)
5-Detector	None	0.022	2.7
r = 3.6 cm	Graphite	0.106	7.6
h = 10 cm	Polyethylene	0.179	105.
	Aluminum	0.057	3.6
5-Detector	None	0.046	2.7
r = 3.8 cm	Graphite	0.190	7.2
h = 30 cm	Polyethylene	0.258	83.
	Aluminum	0.109	3.6
6-Detector	None	0.032	3.1
r = 3.6 cm	Graphite	0.119	7.4
h = 10 cm	Aluminum	0.069	3.8
6-Detector	None	0.064	3.2
r = 3.8 cm	Graphite	0.211	7.1
h = 30 cm	Aluminum	0.131	3.9
Annular	Graphite (5.1 cm)[b]	0.189	7.5
r_2 = 21 cm, fixed	Graphite (3.8 cm)	0.276	5.7
	Graphite (2.5 cm)	0.350	4.8
Annular	BC454 (2.5 cm)	0.126	7.2
r_1 = 13 cm, fixed	BC454 (3.8 cm)	0.228	5.6
	BC454 (5.1 cm)	0.323	4.7
	BC454 (7.6 cm)	0.472	3.9

[a]Detector dimensions refer to individual element radii and height. In the case of the annular configuration, r_1 refers to inner radius and r_2 outer radius of detector element.

[b]Graphite thickness relative to r_1. Detector element plus graphite thickness equals 7.6 cm.

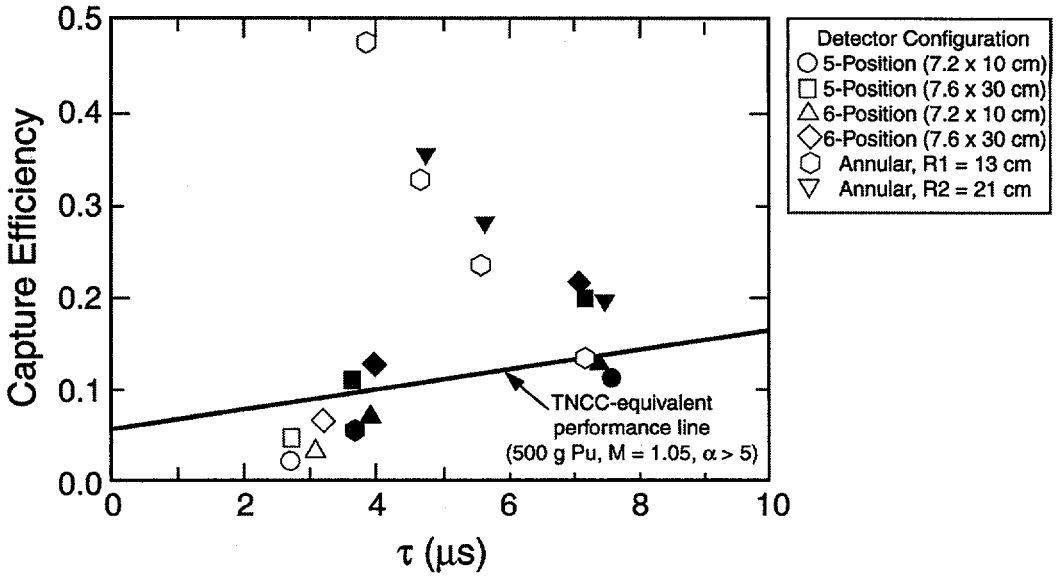

Figure 5-3. Comparison of Various FNCC Designs to TNCC Performance

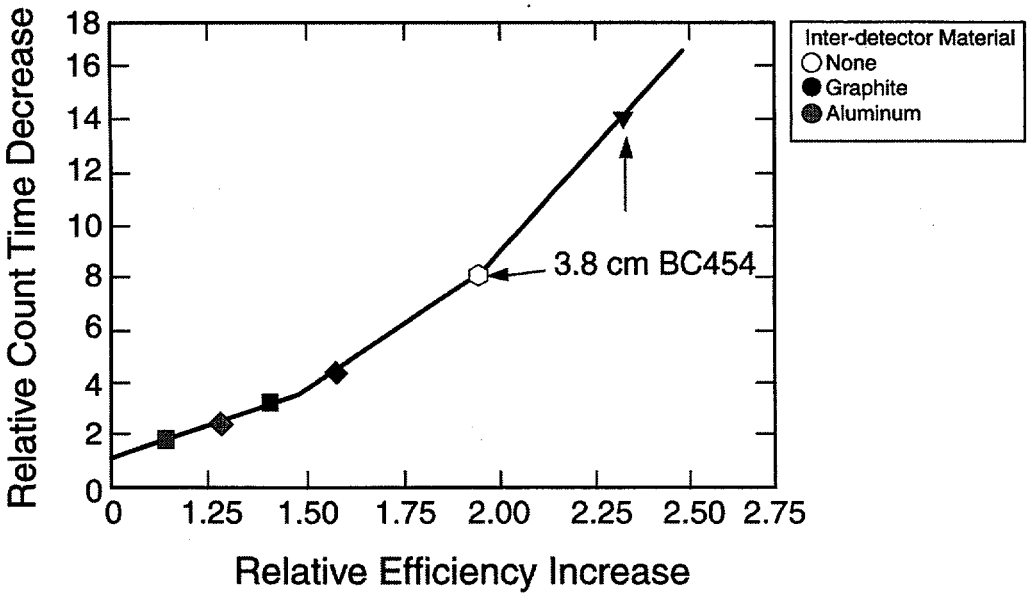

Figure 5-4. Count Time Reduction Relative to TNCC for Selected FNCC Designs

6. CONCLUSIONS

6.1. OVERVIEW

This dissertation suggests that the BC454/BGO phoswich detector is a viable candidate for neutron detection and potential assay applications by 1) separating the individual BC454 and BGO pulses, 2) using spectral discrimination methods to identify neutron events, and 3) applying time-correlation analysis to the filtered data. Experimental demonstration of the detector performance was accomplished and compared with simulation results with good agreement. A data acquisition system has been designed and built that allows the recording of both energy and time for all detected events: BC454 only, BGO only, and BC454+BGO.

Application of neutron time-correlation analysis for the quantitative measurement of special nuclear materials benefits from both high detection efficiency and short die-away time. Existing technology relies on ^{3}He proportional counters embedded in a polyethylene matrix to increase detection efficiency to acceptable levels. The necessarily discrete nature of the detector and moderator results in a fundamental limitation on both achievable efficiencies and die-away times. Current thermal-neutron coincidence counters (TNCC) can attain detection efficiencies on the order of 50%, with a corresponding die-away time of about 50 μs. By combining the moderator (H) with the detector (^{10}B in this case) at the molecular level, this limitation is overcome, resulting in

the physical coupling of high detection efficiency with a short die-away time. The BC454/BGO detector addresses this limitation by combining a boron-loaded plastic scintillator with BGO. Hydrogen is intimately mixed with ^{10}B in BC454, while the addition of BGO enables neutron-capture events to be identified unambiguously through a prompt coincidence between the 93-keV$_{ee}$ peak in the BC454 and the detection of the 478-keV capture gamma ray in the BGO.

Initial calculations have shown that efficiencies of 50% are realistically possible, with a reduction in the die-away time of more than an order of magnitude. Comparison of assay variance estimates for a 50%-efficient TNCC with a 50 μs die-away time versus a corresponding fast neutron coincidence counter having the same efficiency but a 3 μs die-away time was performed, showing that count time reductions of more than 2 orders of magnitude are possible. While this work establishes the possibility of high-efficiency, short die-away time counters, more research required is prior to the practical realization of such a system. An intermediate step would be on the order of 20% detection efficiency and 7 μs.

A data acquisition system has been designed and built that allows collection of up to 10 detector channels and records both the energy and time of each event. The system is designed to accommodate singles count rates of 100,000 counts/sec for a maximum of 1000 seconds. Custom electronics were used to perform a first-order separation of the BC454 and BGO by taking advantage of the differences in the pulse shape of the detector elements. Integration of the detector output is performed in two time domains: 1) an initial short (80 ns) integration that includes most of the BC454 and some BGO and 2) a

subsequent long (400 ns) integration that includes the majority of the BGO and a small fraction of the BC454. The constant fraction discriminator circuit that is on-board with the gated integrator controls the integration timing as well as sending triggers to initiate the conversion of the analog signals by the ADCs and event time-tagging. A 10-channel time-tag module was designed and built that enables the recording of each event time as well as the channel number and diagnostic information such as multiple events occurring during the integration period.

Analyses and simulations were performed for the experimental data obtained. A pulse-separation algorithm and procedure was developed that enables a full separation of the BC454 and BGO responses to be made. Once the detector elements' responses were isolated, an energy calibration was performed for each detector channel and appropriate ROIs determined for neutron-capture event discrimination. Three different methods of neutron discrimination were evaluated: 1) isolation of 93-keV$_{ee}$ events in the BC454 only, 2) requiring a prompt coincidence between the 93-keV$_{ee}$ peak in the BC454 with detection of the 478-keV capture gamma ray in the BGO (narrow ROI set), and 3) requiring a prompt coincidence between the 93-keV$_{ee}$ in the BC454 with the detection of the 478-keV capture gamma ray in full- or partial-energy deposition in the BGO. Results using the three discrimination techniques show that the highest neutron-capture detection is obtained with the 93-keV$_{ee}$-only region of interest (ROI), at the expense of inclusion of non-neutron events into the filtered data. Requiring a prompt coincidence between both detector elements rejects these non-neutron events, at the cost of detection efficiency. In any of the discrimination methods, the point model equations must be modified slightly to account for the specific BC454/BGO response. The efficiency term must also include

the probability of the detection of the 478-keV capture gamma ray, and the α term must be modified to reflect any non-neutron events that are selected.

The demonstration of the quantitative measurement capability of the BC454/BGO detector array was accomplished by performing a series of calculations and comparisons combining the experimental data with the analysis techniques developed and simulations performed. The detection efficiency and die-away time were measured with ^{252}Cf and compared to the values estimated by MCNP simulation. The agreement between the measured and calculated values was good, with ratio of the measured-to-calculated efficiency being 1.07 and the measured-to-calculated die-away time being 0.97. The validity of the point model for analysis of data acquired by the BC454/BGO detectors was tested by taking ratios of the singles and doubles count rates. Agreement between the measured ratios and that expected for ^{252}Cf was reasonably good, with a measured-to-expected doubles ratio of 0.82. Count rates obtained for AmLi were compared to ^{252}Cf. The singles ratio was not the expected value based on measurements with a TNCC because of energy spectrum differences between the two sources. However, the AmLi data did not show any statistically significant doubles counts, a result consistent with the random nature of AmLi neutron emission.

Finally, a small plutonium sample was measured. The agreement between the measured and the known mass was 1.4 and the ratio of measured-to-known α was 0.79. While this result is not of assay caliber, it is encouraging and demonstrates the potential of the BC454/BGO detector array to be used for measurement of special nuclear material.

6.2. SUGGESTIONS FOR FURTHER WORK

A natural extension of the work presented here is the progression to the high-efficiency, short die-away time counter explored by simulation. Achieving the predicted performance will require designing new detectors, new electronics capable of very high throughput to accommodate the high counting rates, and analysis methods where deadtime and associated high-rate problems are significant.

Spectroscopy using the detection system in its current configuration is another area where follow-on work could be done. The exploration of the full use of both the neutron and gamma-ray spectra obtainable by the BC454/BGO detector would have applications to improving assay capability as well extending into new areas of use. For example, nuclear smuggling detection, neutron spectroscopy, determination of the $^{240}Pu_{eff}$ mass fraction concurrently with time-correlation analysis, and the use of time-correlation analysis of fission gamma rays.

Simulation of the full detector response would provide a new analytical tool not available at the present time. This development would require the combination of features that exist in traditional scintillator codes, such as KSUEFF, with those of traditional transport codes, such as MCNP. Response to neutrons and gamma rays would be expanded to light production and transport as a result of neutron capture, proton recoil, and gamma-ray interaction.

APPENDIX A. SOLUTION OF THE POINT EQUATIONS

Solution of the variables m, M, and α is accomplished by first solving for M in the following equation[46]

$$a_1 + b_1 M + c_2 M^2 + M^3 = 0, \tag{A-1}$$

where

$$a_1 = \frac{-3T\nu_{s1}(\nu_{i1} - 1)}{\varepsilon^2 f_t(\nu_{s2}\nu_{i3} - \nu_{s3}\nu_{i2})}, \tag{A-2}$$

$$b_1 = \frac{2D[\nu_{s3}(\nu_{i1} - 1) - 3\nu_{s2}\nu_{i2}]}{\varepsilon f_d S(\nu_{s2}\nu_{i3} - \nu_{s3}\nu_{i2})}, \text{ and} \tag{A-3}$$

$$c_1 = \frac{6D\nu_{s2}\nu_{i2}}{\varepsilon f_d S(\nu_{s2}\nu_{i3} - \nu_{s3}\nu_{i2})}. \tag{A-4}$$

Solve for M by iteration:

(a) Set $M = 1$.

(b) Calculate $z_1 = \dfrac{-a_1 + c_1 M^2 + 2M^3}{b_1 + 2c_1 M + 3M^2}$.

(c) Set $M = z_1$ and repeat (b) until $|M - z_1| < 10^{-9}$

After M is obtained, m and α are given by

$$\alpha = \frac{S}{\varepsilon \nu_{s1} M x_1} - 1, \text{ and} \tag{A-5}$$

$$m = \frac{x_1}{F}, \tag{A-6}$$

where

$$x_1 = \left\lceil \frac{\dfrac{2D}{\varepsilon f_d} - \dfrac{M(M-1)\nu_{i2} S}{\nu_{i1} - 1}}{\varepsilon M^2 \nu_{s2}} \right\rceil \tag{A-7}$$

APPENDIX B. MULTIPLICITY DERIVATION

Derivation of the equations for obtaining the reduced moments of the measured source distributions is accomplished by relating the probability of getting a count of multiplicity n, with the moments of the correlated neutron distribution (reals).

p_n = probability of getting any count of multiplicity n in the pulse-triggered gate,

q_n = probability of getting a count of multiplicity n in the randomly-triggered gate,

r_n = probability of getting any count of multiplicity n in the pulse-triggered gate where all neutrons are from the same fission.

By virtue of being probabilities, p_n, q_n, r_n and have the property

$$\sum_{n=0}^{\infty} p_n = \sum_{n=0}^{\infty} q_n = \sum_{n=0}^{\infty} r_n = 1. \tag{B-1}$$

We define the k^{th} reduced factorial moment of p_n as

$$P_k = \sum_{n=0}^{\infty} \binom{n}{k} p_n, \tag{B-2}$$

Where $\binom{n}{k} = \frac{n!}{(n-k)!\,k!}$. Similar expressions hold for Q_k and R_k. We desire R_0, R_1, and R_2 (moments of the correlated neutron distribution) because they are proportional to S, D, and T (singles, doubles, and triples).

The probability of getting 0, 1, and 2 counts in the pulse-triggered gate can be written as

$$p_0 = r_0 q_0 \qquad \text{(multiplicity 0),} \tag{B-3}$$

$$p_1 = r_1 q_0 + r_0 q_1 \qquad \text{(multiplicity 1), and} \tag{B-4}$$

$$p_2 = r_2 q_0 + r_1 q_1 + r_0 q_2 \qquad \text{(multiplicity 2).} \tag{B-5}$$

In general, we can write the probability of getting n counts in the gate as

$$p_n = \sum_{i=0}^{n} r_{n-i} q_i \cdot \tag{B-6}$$

Singles (S)

We take the 0^{th} reduced factorial moment of p_n

$$\sum_{n=0}^{\infty} p_n = \sum_{n=0}^{\infty} \sum_{i=0}^{n} r_{n-i} q_i \cdot \tag{B-7}$$

We use the Heavyside unit function, $\theta_{n,i}$, to take summation $i \to \infty$.

$$\theta_{n,i} = \begin{cases} 0, & i > n \\ 1, & i \le n \end{cases}, \tag{B-8}$$

to obtain

$$\sum_{n=0}^{\infty} p_n = \sum_{n=0}^{\infty} \sum_{i=0}^{\infty} r_{n-i} q_i \theta_{n,i} \cdot \tag{B-9}$$

We now let $k = n - i$ on RHS to get

$$\sum_{n=0}^{\infty} p_n = \sum_{k=0}^{\infty} \sum_{i=0}^{\infty} r_k q_i \theta_{k,0} \cdot \tag{B-10}$$

The function $\theta_{k,0}$ keeps the summation over k from becoming negative. Because $0 \le k$ at all times, the function can be dropped and we can write

$$\sum_{n=0}^{\infty} p_n = \sum_{k=0}^{\infty}\sum_{i=0}^{\infty} r_k q_i \cdot \tag{B-11}$$

Evaluation of Eq. B-11 yields

$$P_0 = R_0 Q_0 , \tag{B-12}$$

and solving for R_0 we get

$$R_0 = \frac{P_0}{Q_0} = 1 \cdot \tag{B-13}$$

Doubles(D)

We take the 1^{st} reduced factorial moment of p_n and apply a similar procedure to obtain

$$\sum_{n=0}^{\infty} n p_n = \sum_{n=0}^{\infty} n \sum_{i=0}^{n} r_{n-i} q_i , \tag{B-14}$$

$$= \sum_{n=0}^{\infty}\sum_{i=0}^{n} n r_{n-i} q_i \qquad \text{let } k = n - i, \tag{B-15}$$

$$= \sum_{k=o}^{\infty}\sum_{i=0}^{\infty} (k+i) r_k q_i , \tag{B-16}$$

$$= \sum_{k=o}^{\infty}\sum_{i=0}^{\infty} \left(k r_k q_i + i r_k q_i\right) \cdot \tag{B-17}$$

Evaluation gives

$$P_1 = R_1 Q_0 + R_0 Q_1 , \text{ or} \tag{B-18}$$

$$P_1 = R_1 + Q_1, \text{ and so} \tag{B-19}$$

$$R_1 = P_1 - Q_1. \tag{B-20}$$

Triples(T)

We take the 2^{nd} reduced factorial moment of p_n and proceed in a similar manner as above to get

$$\sum_{n=0}^{\infty} \frac{n(n-1)}{2} p_n = \sum_{n=0}^{\infty} \frac{n(n-1)}{2} \sum_{i=0}^{n} r_{n-i} q_i, \tag{B-21}$$

$$= \sum_{n=0}^{\infty} \sum_{i=0}^{n} \frac{n(n-1)}{2} r_{n-i} q_i \qquad \text{let } k = n - i, \tag{B-22}$$

$$= \sum_{k=o}^{\infty} \sum_{i=0}^{\infty} \frac{(k+i)(k+i-1)}{2} r_k q_i, \tag{B-23}$$

$$= \sum_{k=0}^{\infty} \sum_{i=0}^{\infty} \frac{\left(k^2 - k + i^2 - i + 2ki\right)}{2} r_k q_i, \tag{B-24}$$

$$\sum_{k=0}^{\infty} \sum_{i=0}^{\infty} \frac{\left[k(k-1) + i(i-1) + 2ki\right]}{2} r_k q_i, \tag{B-25}$$

$$= \sum_{k=0}^{\infty} \sum_{i=0}^{\infty} \left[\frac{k(k-1)}{2} r_k q_i + \frac{i(i-1)}{2} r_k q_i + kir_k q_i \right], \text{ or} \tag{B-26}$$

$$P_2 = R_2 Q_0 + R_0 Q_2 + R_1 Q_1, \text{ and so} \tag{B-27}$$

$$R_2 = P_2 - Q_2 - R_1 Q_1. \tag{B-28}$$

To obtain count rates we observe that

$$p_i = \frac{(R+A)_i}{\sum_{i=0}^{127}(R+A)_i} \quad \text{and} \quad q_i = \frac{A_i}{\sum_{i=0}^{127} A_i}. \tag{B-29}$$

Finally, we note that

$$S = R_0 \sum_{i=0}^{127} A_i \text{ (total number of triggered events), so} \tag{B-30}$$

$$D = SR_1 = S\sum_{n=1}^{127} i(p_i - q_i), \text{ and} \tag{B-31}$$

$$T = SR_2 = S\left[\sum_{i=2}^{127} \frac{i(i-1)}{2}(p_i - q_i) - \sum_{i=1}^{127} i(p_i - q_i)\sum_{i=1}^{127} iq_i\right]. \tag{B-32}$$

The above equations do not include the effects of deadtime or background.

APPENDIX C. POINT EQUATIONS FOR ACTIVE MULTIPLICITY

The point equations for active multiplicity counting are obtained by setting $\alpha = 0$ and adding terms relevant to the rate of induced fissions by the interrogation source (AmLi). The singles rate is not used in active multiplicity because of the AmLi source and because only two measurements are needed since $\alpha = 0$.

$$D = \frac{sCm\varepsilon^2 f_d \nu_{e2} M^2}{2}\left[1+\left(\frac{M-1}{\nu_{f1}-1}\right)\frac{\nu_{e1}\nu_{f2}}{\nu_{e2}}\right], \text{ and} \tag{C-1}$$

$$T = \frac{sCm\varepsilon^3 f_t \nu_{e3} M^3}{3!}\left[\begin{array}{l} 1+\left(\dfrac{M-1}{\nu_{f1}-1}\right)\dfrac{3\nu_{e2}\nu_{f2}+\nu_{e1}\nu_{f3}}{\nu_{e3}} \\ +3\left(\dfrac{M-1}{\nu_{f1}-1}\right)^2\dfrac{\nu_{e1}\nu_{f2}^2}{\nu_{e3}} \end{array}\right], \tag{C-2}$$

where

D = doubles rate,

T = triples rate,

m = plutonium-240 effective mass,

s = AmLi neutron production rate,

C = Coupling (fissions per source neutron per unit ^{235}U mass),

ε = detection efficiency,

M = neutron multiplication,

f_d = fraction of doubles events in the gate,

f_t = fraction of triples events in the gate,

ν_{e1}, ν_{e2}, ν_{e3} = first, second, and third factorial moments of the epithermal neutron multiplicity distribution, and

ν_{f1}, ν_{f2}, ν_{f3} = first, second, and third factorial moments of the fast-neutron multiplicity distribution.

The moments are different in this case because the spontaneous fission rate is insignificant. Instead, induced fissions caused by the AmLi source are considered the source (epithermal) and subsequent induced fissions are considered multiplication events (fast).

APPENDIX D. ANALYSIS PROGRAMS

1. ANALYZE.C, program reads in event stream, performs pulse separation, and applies filter that user specifies by changing ROIs.

```
/* ANALYZE
  read in the multi-channel data file, perform pulse-separation, filter
  out neutron events- user chooses ROIs
  BINARY DATA input  ASCII DATA output
  output files are
    1) filtered event stream (det_ID, E_pl, E_bgo, f_time, flag, c_time)
    2) histogram (2048 ch) of E_pl and E-bgo*/

#include <stdio.h>
#include <math.h>
#include <stdlib.h>
#include <alloc.h>
#include <process.h>

#define BUF_SIZE        300

static short *event_det_ID, *save_det_ID, *event_E_pl, *event_E_bgo;
static short *save_E_pl, *save_E_bgo;
static short *event_f_time, *save_f_time, *event_flag, *save_flag;
static long *event_c_time, *save_c_time;
static long i, j, k, l, m, p, q;
static short n, o, r, temp_bin1, temp_bin2, bin_pl[2048], bin_bgo[2048];
FILE *fp, *fq, *fr;
char filein[20], fileout[20], histo[20], anal_comment[150],
                comment[250],temp [25],temp2[25];
char cc;

  size_t size;
  struct energy_time
  {
        unsigned char det_ID;
    unsigned long E_pl;
    unsigned long E_bgo;
    unsigned char f_time;
    unsigned char flag;
    unsigned long c_time;
```

```
};
struct energy_time et[BUF_SIZE];


main(void)
{
        printf("ANALYZE\n\n");

/*      Allocate enough memory to process data in BUF_SIZE event-chunks   */
        while (1)
        {


                if ((event_det_ID = (short *) farcalloc(BUF_SIZE,
                sizeof(short)))==NULL)
                {
                        printf("Not enough memory in buffer- event det ID");
                        exit(1);
                }
                if ((event_E_pl = (short *) farcalloc(BUF_SIZE,
                sizeof(short)))==NULL)
                {
                        printf("Not enough memory in buffer- event E pl");
                        exit(1);
    }
                if ((event_E_bgo = (short *) farcalloc(BUF_SIZE,
                sizeof(short)))==NULL)
                {
                        printf("Not enough memory in buffer- event E bgo");
                        exit(1);
    }
                if ((event_f_time = (short *) farcalloc(BUF_SIZE,
                sizeof(short)))==NULL)
                {
                        printf("Not enough memory in buffer- event f time");
                        exit(1);
    }
                if ((event_flag = (short *) farcalloc(BUF_SIZE,
                sizeof(short)))==NULL)
                {
                        printf("Not enough memory in buffer- event flag");
                        exit(1);
    }
                if ((event_c_time = (long *) farcalloc(BUF_SIZE,
                sizeof(long)))==NULL)
                {
                        printf("Not enough memory in buffer- event c time");
                        exit(1);
                }

                if ((save_det_ID = (short *) farcalloc(BUF_SIZE,
                sizeof(short)))==NULL)
                {
                        printf("Not enough memory in buffer- save det ID");
```

```
                exit(1);
    }
        if ((save_E_pl = (short *) farcalloc(BUF_SIZE,
                sizeof(short)))==NULL)
        {
                printf("Not enough memory in buffer- save E pl");
                exit(1);
    }
        if ((save_E_bgo = (short *) farcalloc(BUF_SIZE,
                sizeof(short)))==NULL)
        {
                printf("Not enough memory in buffer- save E bgo");
                exit(1);
    }
        if ((save_f_time = (short *) farcalloc(BUF_SIZE,
        sizeof(short)))==NULL)
        {
                printf("Not enough memory in buffer- save f time");
                exit(1);
    }
        if ((save_flag = (short *) farcalloc(BUF_SIZE,
        sizeof(short)))==NULL)
        {
                printf("Not enough memory in buffer- save flag");
                exit(1);
    }
        if ((save_c_time = (long *) farcalloc(BUF_SIZE,
        sizeof(long)))==NULL)
        {
                printf("Not enough memory in buffer- save c time");
                exit(1);
        }

/*      get filenames- input, output-event stream, output-histogram */
        tryagain:
        printf ("Enter input filename (^C to exit): ");
        scanf ("%s", filein);
        fp = fopen(filein, "rb");

        if (fp == 0)
        {
                printf("Can't find file.\n");
                goto tryagain;
        }

        tryagain1:
        printf ("Enter output filename: ");
        scanf ("%s", fileout);
        fq = fopen(fileout, "w");

        if (fq == 0)
        {
                printf("Can't open file.\n");
                goto tryagain1;
```

```
                }

    tryagain2:
                printf ("Enter histogram output filename: ");
                scanf ("%s", histo);
                fr = fopen(histo, "w");

                if (fr == 0)
                {
                        printf("Can't open file.\n");
                        goto tryagain2;
                }

 /* get analysis comment */
    anal_comment[0]='\0';
    temp[0]='\0';
    temp2[0]='\0';
                printf ("Enter analysis comment: ");

    scanf("%s",temp);
                strcat(anal_comment,temp);
    do
    {
        temp2[0]=cc;
      strcat(anal_comment,temp2);
    }while ((cc=getchar())!='\n');
                fprintf (fq, "%s\n",anal_comment);

 /*         Read in header info                  */

                for (p=0; p<=1; p++)
    {
                        for (o=0; (comment[o]=getc(fp))!='\n'; o++);
                        {
                                comment[o]=0;
                                printf("%s\n", comment);
                                fprintf(fq, "%s\n", comment);
                        }
    }

 /* initialize some values and the histogram array */
        j=0;
                l=0;
                m=0;
                p=0;
        q=0;
    temp_bin1=0;
    temp_bin2=0;


                for (r=0; r<=2047; r++)
        {
      bin_pl[r]=0;
      bin_bgo[r]=0;
```

```
        }

/* loop through data- read/analyze- */
                while (l==0)
    {
                        read_file();
                        analyze_data();
                }

/* write the histogram file */
    fprintf(fr,"%s\t%s\t%s\n","Ch","E_pl","E_bgo");
      for (r=0; r<=2047; r++)
      {
      fprintf(fr,"%d\t%d\t%d\n", r, bin_pl[r],bin_bgo[r]);
      }

                fclose(filein);
                fclose(fileout);
    fclose(histo);

        }
}

read_file()
        {



/*      Read in data (up to BUF_SIZE events)      */


        i=0;
        while (i<=BUF_SIZE)
        {
                        size = fread(&et[i], sizeof(struct energy_time), 1, fp);
      if (size == 1)
      {
         event_det_ID[i]=et[i].det_ID;
        event_E_pl[i]=et[i].E_pl;
        event_E_bgo[i]=et[i].E_bgo;
        event_f_time[i]=et[i].f_time;
        event_flag[i]=et[i].flag;
        event_c_time[i]=et[i].c_time;
      }
                        if (size == 0)  /* if done, return and print event number */
   {
            l=1;
            j=j+i;
                        printf("\nData file is %ld\n", j);
                        return;
                        }
              i++;
              m++;
              if (m==10000)
```

```
                {
                p++;
                q=m*p;

/* print out message every 10,000 events */
                printf ("processing %ld events\n", q);
                m=0;
         }
                }

        j=j+i;


    }

analyze_data()
        {

        for (k=0; k<=i-1; k++)
        {

        save_det_ID[k]=event_det_ID[k];


/* identify detector number and apply pulse-separation algorithm
  leading values are a,b,c,d  offsets are O1/O2/O2/O1 */

        if (event_det_ID[k]==1)
  {
        save_E_pl[k]=1.41366*(event_E_pl[k]-2)-1.58387*(event_E_bgo[k]+162);
        save_E_bgo[k]=3.89985*(event_E_bgo[k]+162)-0.459627*(event_E_pl[k]-2);
  }

        if (event_det_ID[k]==2)
  {
        save_E_pl[k]=1.41366*(event_E_pl[k]-2)-1.4967*(event_E_bgo[k]+38);
        save_E_bgo[k]=3.68522*(event_E_bgo[k]+38)-0.459627*(event_E_pl[k]-2);
  }

        if (event_det_ID[k]==3)
  {
        save_E_pl[k]=1.41366*(event_E_pl[k]-2)-1.37663*(event_E_bgo[k]+172);
        save_E_bgo[k]=3.38959*(event_E_bgo[k]+172)-0.459627*(event_E_pl[k]-2);
        }

        if (event_det_ID[k]==5)
  {
        save_E_pl[k]=1.41366*(event_E_pl[k]-2)-1.51561*(event_E_bgo[k]+38);
        save_E_bgo[k]=3.73179*(event_E_bgo[k]+38)-0.459627*(event_E_pl[k]-2);
  }

        save_f_time[k]=event_f_time[k];
        save_flag[k]=event_flag[k];
        save_c_time[k]=event_c_time[k];
```

```
/* clean up any overflows */
  if (save_E_pl[k]<=0)
        save_E_pl[k]=0;
  if (save_E_bgo[k]<=0)
                save_E_bgo[k]=0;

/* rebin to 2048 (from 16384) channels */
  temp_bin1= (( int )save_E_pl[k])>>3;
        temp_bin2=(( int )save_E_bgo[k])>>3;



/* determine if event is within ROI for each detector, increment histogram
  data, and write to event file  first is ROI-1, second is ROI-2*/
        if (event_det_ID[k]==1)
        {
        if (temp_bin1 >= 0 && temp_bin1 <= 100 && temp_bin2 >= 90 && temp_bin2 <= 159)
  {
                bin_pl[temp_bin1]++;
                bin_bgo[temp_bin2]++;
                fprintf(fq,"%d\t%d\t%d\t%d\t%d\t%ld\n", save_det_ID[k], temp_bin1,
                        temp_bin2, save_f_time[k], save_flag[k], save_c_time[k]);
        }
        }

        if (event_det_ID[k]==2)
        {
        if (temp_bin1 >= 0 && temp_bin1 <= 100 && temp_bin2 >= 110 && temp_bin2 <= 247)
  {
                bin_pl[temp_bin1]++;
                bin_bgo[temp_bin2]++;
    fprintf(fq,"%d\t%d\t%d\t%d\t%d\t%ld\n", save_det_ID[k], temp_bin1,
                temp_bin2, save_f_time[k], save_flag[k], save_c_time[k]);
        }
        }
  if (event_det_ID[k]==3)
        {
        if (temp_bin1 >= 0 && temp_bin1 <= 100 && temp_bin2 >= 60 && temp_bin2 <= 128)
  {
                bin_pl[temp_bin1]++;
                bin_bgo[temp_bin2]++;
    fprintf(fq,"%d\t%d\t%d\t%d\t%d\t%ld\n", save_det_ID[k], temp_bin1,
                temp_bin2, save_f_time[k], save_flag[k], save_c_time[k]);
        }
        }
  if (event_det_ID[k]==5)
        {
        if (temp_bin1 >= 0 && temp_bin1 <= 100 && temp_bin2 >= 110 && temp_bin2 <= 247)
  {
                bin_pl[temp_bin1]++;
                bin_bgo[temp_bin2]++;
    fprintf(fq,"%d\t%d\t%d\t%d\t%d\t%ld\n", save_det_ID[k], temp_bin1,
                temp_bin2, save_f_time[k], save_flag[k], save_c_time[k]);
```

```
        }
        }


  }
        }
```

---

2. TIMEPREP.C, program reads in event stream (original or filtered) and then writes out c_time in binary format (preparation for MULTDIST.C).

```
/* TIMEPREP
        read in the multi-channel data file (original or output from ANALYZE
        Output is time tag only- prep for MULTDIST
        ASCII DATA input  BIBARY DATA output*/

#include <stdio.h>
#include <math.h>
#include <stdlib.h>
#include <alloc.h>
#include <process.h>

#define BUF_SIZE        300

static int *event_det_ID, *save_det_ID, *event_E_pl, *event_E_bgo;
static int *save_E_pl, *save_E_bgo;
static int *event_f_time, *save_f_time, *event_flag, *save_flag;
static long *event_c_time, *save_c_time;
static long i, j, k, l, m, p, q;
static int n, o, r, temp_bin1, temp_bin2, bin_pl[2048], bin_bgo[2048];
FILE *fp, *fq, *fr;
char filein[20], fileout[20], histo[20], anal_comment[150],
                comment[250],temp [25],temp2[25];
char cc;

main(void)
{
        printf("TIMEPREP\n\n");

/*      Allocate enough memory to process data in BUF_SIZE event-chunks   */
        while (1)
        {


                if ((event_det_ID = (int *) farcalloc(BUF_SIZE,
                sizeof(int)))==NULL)
                {
```

```
                printf("Not enough memory in buffer- event det ID");
                exit(1);
        }
        if ((event_E_pl = (int *) farcalloc(BUF_SIZE,
        sizeof(int)))==NULL)
        {
                printf("Not enough memory in buffer- event E pl");
                exit(1);
}
        if ((event_E_bgo = (int *) farcalloc(BUF_SIZE,
        sizeof(int)))==NULL)
        {
                printf("Not enough memory in buffer- event E bgo");
                exit(1);
}
        if ((event_f_time = (int *) farcalloc(BUF_SIZE,
        sizeof(int)))==NULL)
        {
                printf("Not enough memory in buffer- event f time");
                exit(1);
}
        if ((event_flag = (int *) farcalloc(BUF_SIZE,
        sizeof(int)))==NULL)
        {
                printf("Not enough memory in buffer- event flag");
                exit(1);
}
        if ((event_c_time = (long *) farcalloc(BUF_SIZE,
        sizeof(long)))==NULL)
        {
                printf("Not enough memory in buffer- event c time");
                exit(1);
        }

        if ((save_det_ID = (int *) farcalloc(BUF_SIZE,
        sizeof(int)))==NULL)
        {
                printf("Not enough memory in buffer- save det ID");
                exit(1);
}
        if ((save_E_pl = (int *) farcalloc(BUF_SIZE,
                sizeof(int)))==NULL)
        {
                printf("Not enough memory in buffer- save E pl");
                exit(1);
}
        if ((save_E_bgo = (int *) farcalloc(BUF_SIZE,
                sizeof(int)))==NULL)
        {
                printf("Not enough memory in buffer- save E bgo");
                exit(1);
}
        if ((save_f_time = (int *) farcalloc(BUF_SIZE,
        sizeof(int)))==NULL)
```

```
                {
                        printf("Not enough memory in buffer- save f time");
                        exit(1);
    }
                if ((save_flag = (int *) farcalloc(BUF_SIZE,
                sizeof(int)))==NULL)
                {
                        printf("Not enough memory in buffer- save flag");
                        exit(1);
    }
                if ((save_c_time = (long *) farcalloc(BUF_SIZE,
                sizeof(long)))==NULL)
                {
                        printf("Not enough memory in buffer- save c time");
                        exit(1);
                }

/*      get filenames- input, output- c_time */
                tryagain:
                printf ("Enter input filename (^C to exit): ");
                scanf ("%s", filein);
                fp = fopen(filein, "r");

                if (fp == 0)
                {
                        printf("Can't find file.\n");
                        goto tryagain;
                }

                tryagain1:
                printf ("Enter output filename: ");
                scanf ("%s", fileout);
                fq = fopen(fileout, "wb");

                if (fq == 0)
                {
                        printf("Can't open file.\n");
                        goto tryagain1;
                }



/*      Read in header info                     */

                for (p=0; p<=2; p++)
    {
                        for (o=0; (comment[o]=getc(fp))!='\n'; o++);
                        {
                                comment[o]=0;
                                printf("%s\n", comment);
//                              fwrite(&comment,sizeof(comment),1,fq);
                        }
    }
```

```
/* initialize some values */
        j=0;
                l=0;
                m=0;
                p=0;
        q=0;
    temp_bin1=0;
    temp_bin2=0;


/* loop through data- read/write */
                while (l==0)
    {
                        read_file();

                }


                fclose(filein);
                fclose(fileout);

        }
}

read_file()
        {



/*      Read in data (up to BUF_SIZE events)      */


        i=0;
        while (i<=BUF_SIZE)
         {
                n=fscanf(fp,"%d\t%d\t%d\t%d\t%d\t%ld", &event_det_ID[i], &event_E_pl[i],
        &event_E_bgo[i], &event_f_time[i], &event_flag[i], &event_c_time[i]);
                if (n!=6)
                        {       /* if done, return and print event number */
             l=1;
             j=j+i;
                        printf("\nData file is %ld\n", j);
                        break;
                        }
/* write out c_time- binary format */
                fwrite(&event_c_time[i], sizeof(long),1,fq);
                i++;
                m++;
                if (m==10000)
                {
                p++;
                q=m*p;
                printf ("processing %ld events\n", q);
```

```
                m=0;
        }
                }

        j=j+i;


    }
```

---

3. MULTDIST.C, read in the c_time stream (output from TIMEPREP) and generate the R+A and A multiplicity distributions.

```
/* MULTDIST
        read in the c_time data from output of TIMEPREP (BINARY)
        generate R+A and A multiplicity distributions */

#include <stdio.h>
#include <math.h>
#include <stdlib.h>
#include <alloc.h>
#include <process.h>

#define BUF_SIZE  300

static long *event_c_time;
static long i, j, k, l, m, p, q, r, s, t, x, y, z, temp_event, ra[100], a[100];
static long start_time, end_time, interval, temp_time;
static int n, o;
static int toggle;
FILE *fp, *fq;
char filein[20], fileout[20], anal_comment[150],
                comment[250],temp [25],temp2[25];
char cc;

size_t size;

main(void)
{
        printf("MULTDIST\n\n");

/*      Allocate enough memory to process data in BUF_SIZE event-chunks   */
        while (1)
        {


                if ((event_c_time = (long *) farcalloc(BUF_SIZE,
```

```
                sizeof(long)))==NULL)
        {
                printf("Not enough memory in buffer- event c time");
                exit(1);
        }


/*      get filenames- input, output- R+A and A histogram */
        tryagain:
        printf ("Enter input filename (^C to exit): ");
        scanf ("%s", filein);
        fp = fopen(filein, "rb");

        if (fp == 0)
        {
                printf("Can't find file.\n");
                goto tryagain;
        }

        tryagain1:
        printf ("Enter output filename: ");
        scanf ("%s", fileout);
        fq = fopen(fileout, "w");

        if (fq == 0)
        {
                printf("Can't open file.\n");
                goto tryagain1;
        }

/* get analysis comment */
    z=0;
    anal_comment[0]='\0';
    temp[0]='\0';
    temp2[0]='\0';
        printf ("Enter analysis comment: ");

    scanf("%s",temp);
        strcat(anal_comment,temp);
    do
    {
        temp2[0]=cc;
      strcat(anal_comment,temp2);
    }while ((cc=getchar())!='\n');
        fprintf (fq, "%s\n",anal_comment);

/* initialize some values and the histogram array */
        j=0;
                l=0;
                m=0;
                p=0;
                q=0;
                s=0;
                t=0;
```

```
                temp_event=0;
                toggle=0;


                        for (r=0; r<=99; r++)
        {
                        ra[r]=0;
                        a[r]=0;
                        }

/* loop through data- read/analyze R+A- */
                while (l==0)
    {
                        read_file();
                        analyze_rplusa();
                }

/* loop through data again (period is singles rate- read/analyze A- */
    i=0;
                m=0;
                p=0;
                q=0;
    event_c_time[0]=0;
                x=interval;
    printf("x= %ld\n", x);
    y=1;


                for (k=1; k<=j-11; k++)
                {
        x=k*interval;   /* step size through data for A */

  /* set pointer back to either beginning or last spot in file */
                        fseek(fp,z,SEEK_SET);
                        while (event_c_time[0]<x)   /* read until c_time larger than x */
                        {
                                fread(&event_c_time[0],sizeof(long),1,fp);

                        }
                        z=ftell(fp); /* determine pointer location */
                        for (i=1; i<=9; i++)   /* read in next 9 c_times */
                        {
      fread(&event_c_time[i],sizeof(long),1,fp);
                        }
                        analyze_a();  /* get A */
                        m++;
                        if (m==10000)   /* print message every 10,000 events */
                        {
                                p++;
                                q=m*p;
                                printf("Processing %ld events\n", q);
                                m=0;
                        }
```

```
                }
    printf("\nData file is %ld \n",q+m);

   /* write histogram */
                fprintf(fq,"%s\t%s\t%s\n","n","R+A","A");
                for (r=0; r<=99; r++)
                {
                fprintf(fq,"%ld\t%ld\t%ld\n", r, ra[r], a[r]);
                }

                fclose(filein);
                fclose(fileout);

        }
}

read_file()
        {

        i=0;
        while (i<=BUF_SIZE)
        {
                        n = fread(&event_c_time[i], sizeof(long), 1, fp);
                        if (n == 0)
        {        /* if done, return and print event number */
              l=1;
              j=j+i;
                        printf("\nData file is %ld\n", j);

    end_time=event_c_time[i-1];
                interval=(end_time-start_time)/j;
    printf("%ld\t%ld\t%ld\t%ld\n", start_time, end_time, interval, j);

                        return;
                        }
                if (i==2 && j==0) start_time=event_c_time[i];
                i++;
                m++;
                if (m==10000)
                {
                p++;
                q=m*p;

/* print out message every 10,000 events */
                printf ("processing %ld events\n", q);
                m=0;
         }
                }

        j=j+i;
```

```
  }

analyze_rplusa()
        {
/* get R+A */
        for (k=0; k<=i-2; k++)
        {
        if (k==0 && toggle==0)
                {
                k++;
                toggle=1;
                temp_event=event_c_time[k];
                }
                else if (k==0)
                        {
                        if (abs(event_c_time[k]-temp_event >=0) && abs(event_c_time[k]-temp_event
<= 60)) toggle=2;
                                else ra[0]++;
                        }
        temp_event=event_c_time[k];
        if (abs(event_c_time[k+1]-event_c_time[k] >=0) && abs(event_c_time[k+1]-event_c_time[k] <=
60)) toggle=2;
                else
                        {
                        ra[0]++;
//                      printf("0\n");
                        }

        while (toggle==2)
        {
        while (event_c_time[k+t+1]-event_c_time[k] <= 60)
        {

                if (abs(event_c_time[k+t+1]-event_c_time[k]-0 >= 0) && abs(event_c_time[k+t+1]-
event_c_time[k] <= 60)) s++;
                t++;
        }
        ra[s]++;
//      printf("%ld\n", s);
        s=0;
        t=0;
        toggle=1;
        }



        }


        }


analyze_a()
        {
```

```
        if (abs(event_c_time[0]-x >=0) && abs(event_c_time[0]-x <= 60)) toggle=2;
                        else
                        {
                        a[0]++;
//                      printf("0\n");
                        }

        while (toggle==2)
        {
        while (event_c_time[t]-x <= 60)
        {

                if (abs(event_c_time[t]-x-0 >= 0) && abs(event_c_time[t]-x <= 60)) s++;
                t++;
        }
        a[s]++;
//      printf("%ld\n", s);
        s=0;
        t=0;
        toggle=1;
        }


        }
```

---

4. ROSALPHA.C,

```
/* ROSALPHA
  read in the modified c_time only file (ASCII) and generate
  Rossi-Alpha distribution with 4096 ticks (1 ms)  */

#include <stdio.h>
#include <math.h>
#include <stdlib.h>
#include <alloc.h>
#include <process.h>

#define BUF_SIZE  300

static long *event_c_time;
static long i, j, k, l, m, p, q, temp_event, start, end, r, temp_bin1, time[4096];
static int n, o;
static int toggle;
FILE *fp, *fq;
char filein[20], fileout[20], anal_comment[150],
```

```
                comment[250],temp [25],temp2[25];
char cc;

main(void)
{
        printf("ROSALPHA\n\n");

/*      Allocate enough memory to process data in BUF_SIZE event-chunks   */
        while (1)
        {


                if ((event_c_time = (long *) farcalloc(BUF_SIZE,
                        sizeof(long)))==NULL)
                {
                        printf("Not enough memory in buffer- event c time");
                        exit(1);
                }



/*      get filenames- input, output- Rossi-Alpha histogram */
                tryagain:
                printf ("Enter input filename (^C to exit): ");
                scanf ("%s", filein);
                fp = fopen(filein, "r");

                if (fp == 0)
                {
                        printf("Can't find file.\n");
                        goto tryagain;
                }

                tryagain1:
                printf ("Enter output filename: ");
                scanf ("%s", fileout);
                fq = fopen(fileout, "w");

                if (fq == 0)
                {
                        printf("Can't open file.\n");
                        goto tryagain1;
                }



/* get analysis comment */
    anal_comment[0]='\0';
    temp[0]='\0';
    temp2[0]='\0';
                printf ("Enter analysis comment: ");

    scanf("%s",temp);
                strcat(anal_comment,temp);
```

```
    do
    {
        temp2[0]=cc;
      strcat(anal_comment,temp2);
    }while ((cc=getchar())!='\n');
                fprintf (fq, "%s\n",anal_comment);

/*      Read in header info                     */

                for (p=0; p<=2; p++)
    {
                        for (o=0; (comment[o]=getc(fp))!='\n'; o++);
                        {
                                comment[o]=0;
                                printf("%s\n", comment);
                                fprintf(fq, "%s\n", comment);
                        }
    }


/* initialize some values and the histogram array */
        j=0;
                l=0;
                m=0;
                p=0;
        q=0;
    temp_bin1=0;
                temp_event=0;
                toggle=0;
                start=0;
                end=0;


                        for (r=0; r<=4095; r++)
        {
                        time[r]=0;
                        }

 /* loop through data- read/analyze- */
                while (l==0)
    {
                        read_file();
                        analyze_data();
                }

/* write the histogram file */
                fprintf(fq,"%s\t%s\t%s\n","time","number");
                        for (r=0; r<=4095; r++)
                        {
                        fprintf(fq,"%ld\t%ld\n", r, time[r]);
                        }

                fclose(filein);
                fclose(fileout);
```

```
        }
}

read_file()
        {


/*      Read in data (up to BUF_SIZE events)        */


        i=0;
        while (i<=BUF_SIZE)
         {
                n=fscanf(fp,"%ld", &event_c_time[i]);
                if (n!=1)
                        {       /* if done, return and print event number */
              l=1;
              j=j+i;
                        printf("\nData file is %ld\n", j);
                        break;
                        }
                i++;
                m++;
                if (m==10000)
                {
                p++;
                q=m*p;

/* print out message every 10,000 events */
                printf ("processing %ld events\n", q);
                m=0;
         }
                }

        j=j+i;


    }

analyze_data()
        {

/* bin arrival times up to 4096 ticks ( 1ms) then reset clock */
        for (k=0; k<=i-1; k++)
        {

        if (k==0 && toggle==0)
                {
                k++;
                k++;
                toggle=1;
                start=event_c_time[k-1];
```

```
                end=start+4095;
                }
                else if (k==0)
                        {
                        if ((event_c_time[k] <= end))
                                {
                                temp_bin1=event_c_time[k]-start;
                                toggle=1;
                                }
                                else
                                {
                                start=temp_event;
                                end=start+4095;
                                toggle=2;
                                }
                        }

        if (k==i-1) temp_event=event_c_time[k];

        if ((event_c_time[k] <= end))
                {
                temp_bin1=event_c_time[k]-start;
                toggle=1;
                }
                else
                {
                start=event_c_time[k];
                end=start+4095;
    toggle=2;
                }

/* allow for possibility of negative time difference due to
  order in which TTM is read out 1.5 microseconds max */
        if (temp_bin1 < -6)
                {
                k++;
                toggle=2;
                }
                else temp_bin1=abs(temp_bin1);


        if (toggle==1)
                {
                time[temp_bin1]++;
                }


        }


        }
```

APPENDIX E. LIST OF TERMS AND ACRONYMS

A	accidentals gate
ADC	analog-to-digital converter
ANDAS	Advanced Neutron Detection and Analysis System
BC454	boron-loaded plastic scintillator (Bicron Corp.)
BGO	bismuth germanate
CFD	constant-fraction discriminator
DOE	Department of Energy
FA	detector flight assembly
FNCC	Fast-Neutron Coincidence Counter
FOM	figure-of-merit
FWHM	full width at half maximum
G_1,G_2	first (short) and second (long) integration gates
GI	gated integrator
GRS	Gamma-Ray Spectrometer experiment on NASA's Lunar Prospector Mission
HV	high voltage
IAEA	International Atomic Energy Agency
LV	low voltage

MC&A	materials control and accountancy
MCA	multichannel analyzer
NCC	Neutron Coincidence Counter (software)
NDA	non-destructive assay
NIM	Nuclear Instrument Module
NPT	Nonproliferation Treaty
NRC	Nuclear Regulatory Commission
PMT	photomultiplier tube
R+A	reals plus accidentals gate
ROI	region of interest
SNM	special nuclear material
TNCC	Thermal-Neutron Coincidence Counter
TTM	time-tag module
VME	Versa Module Eurocard
VSB	VME Subsystem Bus

APPENDIX F. LIST OF VARIABLES

α	(alpha,n)-to-spontaneous fission neutron ratio
A	accidentals multiplicity count distribution
a, b, c, d	pulse-separation algorithm constants
a_1, b_1, c_1, x_1, z_1	point-equation solution variables
B	digitized BGO pulse integration value (completely integrated)
C	coupling constant for active multiplicity (fissions per unit source per gram)
ch	channel number
D	doubles count rate
E	energy (keV)
ε	neutron detection efficiency
F	spontaneous fission rate per gram
$f(t)$	analytical model for BC454 pulse shape
f_d	fraction of doubles in the gate
f_{B1}, f_{B2}	fraction of BGO pulse area residing within the G_1 and G_2 integrator channels
f_{P1}, f_{P2}	fraction of BC454 pulse area residing within the G_1 and G_2 integrator channels

f_t	fraction of triples in the gate
$g(t)$	analytical model for BGO pulse shape
h	height
I_1, I_2	digitized pulse integration values for the G_1 and G_2 integrator channels
k	relative gain for the G_1 and G_2 integrator channels
m	Pu-240 effective mass
M	neutron net leakage multiplication
N	number of closely-spaced counts in shift register
n_{10}	^{10}B atom density (atoms/cm^3)
ν	number of neutrons emitted
$\bar{\nu}$	first moment of $P(\nu)$
$\overline{\nu(\nu-1)}$	second factorial moment of $P(\nu)$
$\overline{\nu(\nu-1)(\nu-2)}$	third factorial moment of $P(\nu)$
$\nu_{e1}, \nu_{e2}, \nu_{e3}$	first, second, and third factorial moments of the epithermal neutron multiplicity distribution
$\nu_{f1}, \nu_{f2}, \nu_{f3}$	first, second, and third factorial moments of the fast neutron multiplicity distribution
$\nu_{i1}, \nu_{i2}, \nu_{i3}$	first, second, and third factorial moments of the induced fission neutron distribution
$\nu_{s1}, \nu_{s2}, \nu_{s3}$	first, second, and third factorial moments of the spontaneous fission neutron multiplicity distribution

O_1, O_2	digitized integration value of baseline for the G_1 and G_2 integrator channels
p	reals plus accidentals multiplicity probability distribution
$P(\nu)$	density function for neutron emission
P	digitized BC454 pulse integration value (completely integrated)
P_k, Q_k, R_k	k^{th} reduced factorial moment of the reals plus accidentals, accidentals, and reals multiplicity distributions
$^{240}Pu_{eff}$	Pu-240 effective mass
q	accidentals multiplicity probability distribution
r	radius
r	reals multiplicity probability distribution
R	reals multiplicity count distribution
$R+A$	real plus accidentals multiplicity count distribution
R^2	fit-correlation coefficient
s	AmLi neutron production rate
S	singles count rate
σ	^{10}B(n,alpha) cross section
T	triples count rate
τ	average neutron lifetime (die-away time)
τ_P	shaping parameter for $f(t)$
τ_{B1}, τ_{B2}	shaping parameters for $g(t)$

$\theta_{n,j}$	Heavyside unit function
υ	neutron velocity
x	energy calibration intercept (keV)
X	fraction of BGO pulse area residing within the sum of the G_1 and G_2 integrator channels
y	energy calibration slope (keV/ch)

REFERENCES

[1] D. Reilly, N. Ensslin, and H. Smith, Jr., Eds., Passive Nondestructive Assay of Nuclear Materials, Nuclear Regulatory Commission report NUREG/CR-5550 (March 1991), Chapter 16.

[2] K. Böhnel, "Determination of Plutonium in Nuclear Fuels Using the Neutron Coincidence Method," KFK2203, Karlsruhe (1975), also AWRE Translation 70 (54/4252), Aldermaston (1978).

[3] M. S. Krick and J. E. Swansen, "Neutron Multiplicity and Multiplication Measurements," *Nucl. Inst. Meth.* **219**, 384-393 (1984).

[4] D. M. Cifarelli and W. Hage, "Models for a Three Parameter Analysis of Neutron Signal Correlation Measurements for Fissile Material Assay," *Nucl. Inst. Meth.* **A251**, 550-563 (1986).

[5] See Ref. 1, Chapters 6 - 10.

[6] Adapted from Ref. 1, p. 342.

[7] See Ref.2.

[8] M. Stevens, J. Swansen, and L. East, "Shift Register Neutron Coincidence Module," Los Alamos Scientific Laboratory report LA-6121-MS (1975).

[9] J. Swansen, P. Collinsworth, and M. Krick, "Shift Register Coincidence Electronics System for Thermal Neutron Counters," *Nucl. Inst. Meth.* **176**, 555-565 (1980).

[10] N. Picilio, "Reactor Noise Analysis in the Time Domain," AEC Critical Review Series TID 24512 (1969).

[11] W. Hage and D. M. Cifarelli, "Correlation Analysis with Neutron Count Distributions in Randomly or Signal Triggered Time Intervals for Assay of Special Fissile Materials," *Nucl. Sci. Eng.* **89**, 159-176 (1985).

[12] K. Böhnel, "The Effect of Multiplication on the Quantitative Determination of Spontaneously Fissioning Isotopes by Neutron Correlation Analysis," *Nucl. Sci. Eng.* **90**, 75-82 (1985).

[13] N. Ensslin, "A Simple Self-Multiplication Correction for In-Plant Use," in *Proceedings of the 7th Annual Symposium on Safeguards and Nucl. Mater. Manage.* (ESARDA, Liege, Belgium ,1985) Vol. 19, pp. 233-238.

[14] H. O. Menlove, R. Abedin-Zadeh, and R. Zhu, "The Analyses of Neutron Coincidence Data to Verify Both Spontaneous-Fission and Fissionable Isotopes," Los Alamos National Laboratory report LA-11639-MS (August 1989).

[15] D. G. Langner, et al., "Neutron Multiplicity Counter Development," in *Proceedings of the 13th Annual Symposium on Safeguards and Nucl. Mater. Manage.* (ESARDA, Avignon, France, 1991) Vol. 24, pp. 285-290.

[16] N. Ensslin, M. S. Krick, D. G. Langner, and M. C. Miller, "Active Neutron Multiplicity Counting of Bulk Uranium," *Nucl. Mater. Manage.* **XX**, 433-437 (1991).

[17] D. M. Drake, W. C. Feldman, and C. Hurlbut, "New Electronically Black Neutron Detectors," *Nucl. Inst. Meth.* **A247**, 576-582 (1986).

[18] ibid.

[19] W. C. Feldman, G. F. Auchampaugh, and R. C. Byrd, "A Novel Fast-Neutron Detector for Space Applications," *Nucl. Inst. Meth.* **A306**, 350-365 (1991).

[20] R. C. Byrd, B. L. Barraclough, W. C. Feldman, and S. J. Bame, "Measurements and Calculations for a Space-Based Neutron Sensor," Los Alamos National Laboratory report LA-12340-MS (October 1992).

[21] Courtesy of R. C. Byrd.

[22] Courtesy of R. C. Byrd.

[23] R. C. Byrd, G. F. Auchampaugh, and W. C. Feldman, "Measurement and Analysis of Neutron Energy Spectra from Fission Sources," Los Alamos National Laboratory report LA-12627-MS (November 1993).

[24] R. C. Byrd, "Directional Fast-Neutron Detectors," Los Alamos National Laboratory report LA-12379-MS (October 1992).

[25] R. C. Byrd, G. F. Auchampaugh, and W. C. Feldman, "Directional Measurements for Sources of Fission Neutrons," Los Alamos National Laboratory report LA-12633-MS (November 1993).

[26] Courtesy of R. C. Byrd.

[27] J. B. Birks, The Theory and Practice of Scintillation Counting, (Pergamon, London, 1964) p. 384.

[28] J. F. Briesmeister, Ed., "MCNP- A General Monte Carlo N-Particle Transport Code, Version 4A," Los Alamos National Laboratory report LA-12625-M (November 1993).

[29] N. Ensslin, N. Dytlewski, and M. S. Krick, "Assay Variance as a Figure of Merit for Neutron Multiplicity Counters," *Nucl. Inst. Meth.* **A290**, 197-207 (1990).

[30] See Ref. 19.

[31] E. A. Kamykowski, "Analysis of Mean Lifetime for Capture of Neutrons in Boron-Loaded Plastic Scintillators," *Nucl. Inst. Meth.* **A299**, 105-110 (1990).

[32] R. C. Byrd and W. T. Urban, "Calculations of the Neutron Response of Boron-Loaded Scintillators," Los Alamos National Laboratory report LA-12833-MS (December 1994).

[33] See Ref. 29.

[34] M. C. Miller, R. C. Byrd, N. Ensslin, W. C. Feldman, M. S. Krick, T. H. Prettyman, and P. R. Russo, "Conceptual Design of a Fast Neutron Coincidence Counter for Verification of Special Nuclear Materials," *Appl. Radiat. Isot.* (to be published).

[35] W. C. Feldman (private communication).

[36] R. C. Byrd and P. A. Russo, "Experimental Tests of a Radiation Direction Finder," Los Alamos National Laboratory report LA-13212-MS (November 1996).

[37] Courtesy of W. C. Feldman.

[38] Courtesy of W. C. Feldman.

[39] Bicron Corp. data sheet.

[40] Courtesy of W. C. Feldman.

[41] W. C. Feldman, A. B. Binder, G. S. Hubbard, R. E. McMurray, Jr., M. C. Miller, and T. H. Prettyman, "The Lunar Prospector Gamma-Ray Spectrometer," *Proc. Lunar Planet. Sci. Conf.* XXVII, Houston TX, 1996.

[42] G. F. Knoll, Radiation Detection and Measurement, (Wiley, New York, 1989), p. 570-572.

[43] See Ref. 1, p. 348.

[44] R. A. Cecil, B. D. Anderson, and R. Madey, "Improvded Predictions of Neutron Detection Efficiency for Hydrocarbon Scintillators form 1 MeV to about 300 MeV," *Nucl. Inst. Meth.* **161**, 439-447 (1979).

[45] R. C. Byrd, private communication

[46] B. Harker and M. Krick, Software Users Manual- Windows NCC, Los Alamos National Laboratory document, 1996 (unpublished).

*U.S. GOVERNMENT PRINTING OFFICE 1998-0-673-028/27051